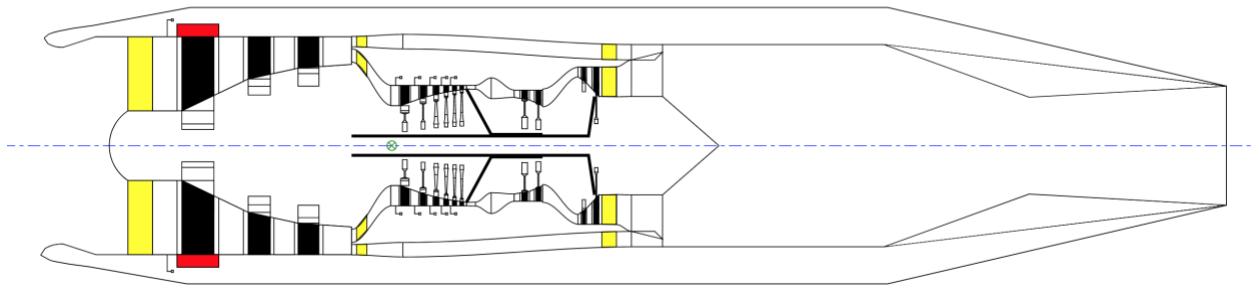


YJ-2030: Candidate Engine for a Supersonic Business Jet

AIAA Foundation 2019 – 2020 Undergraduate
Engine Design Competition



Team Leader:
Ted Vlady

Team Members:
Soon Keat Ong
Oscar Klempay
Steve Zakharov

Advisor:
Dr. Jerry Seitzman
Mr. Russell Denney



SIGNATURE PAGE:

Design Team:

Oscar Klempay
#738508



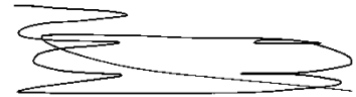
Soon Keat Ong
#738218



Ted Vlady
#921865



Steve Zakharov
#921876



Faculty Advisors:

Mr. Russell Denney
#414062

Dr. Jerry Seitzman
#070425

Executive Summary:

The YJ-2030 is a candidate engine to be installed on the next supersonic business jet. It offers high performance across the flight envelope with a similar nacelle envelope to the baseline engine. The features on the YJ-2030 allow it to supercruise at Mach 2.1 over the water with the potential to reach Mach 3.0 flight. The engine implements new material and manufacturing technologies that decrease its weight while increasing component performance. The engine meets Stage 5 noise constraints and supercruise emissions goals. The LTO emissions performance must be revisited during component testing. A summary of the YJ-2030 components and performance is shown below.

Component	Description
Engine Architecture	Afterburning Mixed Flow Turbofan
Inlet	4 shock, 2-D Mixed Compression Supersonic inlet
Fan	3-Stage High Efficiency Fan with Polyimide Fan Blades
HPC	6 Stage All Blisk HPC
Burner	Next generation annular, lean-premixed combustor
HPT	2 Stage cooled HPT manufactured from CMC
HPC	2 Stage uncooled LPT manufactured from CMC
Mixer	Full composite deeply scalloped, highly lobed mixer design
Afterburner	Shares duct with mixer-ejector and core-bypass mixer to reduce length
Nozzle	Fully Variable Axisymmetric Converging Diverging Nozzle
Performance Metric	Value
Fan Diameter (in)	49.2
Weight (lbm)	4338
Engine + Inlet Length (feet)	34.66 feet
NYC to London Fuel burn (lbm)	92769
Time for NYC to London	4:57
Range at Mach 0.98, 40000 feet (nm)	5300
Takeoff Exit Jet Velocity	1100 ft/s with Mixer-Ejector Active
Supercruise NOx emissions (g/kg)	4.83
LTO cycle NOx	Does Not Meet Requirement*

*NOx relationships must be revisited after combustor testing

Table of Contents

1.	<i>Introduction</i>	1
2.	<i>Requirements Definition</i>	2
2.1	Mission Definition	2
2.2	Baseline Engine	2
2.3	Thrust requirements	3
2.4	Additional Requirements	5
3.	<i>Cycle Analysis</i>	5
3.1	Cycle Architecture	5
3.2	Addition of Augmentor	7
3.3	Cycle Optimization	8
3.3.1	Approach.....	8
3.3.2	Assumptions.....	9
3.3.3	Cycle Optimization Results.....	11
3.4	Final Cycle Summary	13
4.	<i>Inlet</i>	15
4.1	Inlet Architecture	15
4.2	Inlet Design	16
4.3	Inlet Off Design Performance	19
4.4	Materials and Manufacturing	21
5.	<i>Compressors</i>	21
5.1	Design Approach	21
5.2	Fan	23
5.2.1	Fan Design Results.....	24
5.2.2	Fan Blade Design.....	27
5.2.3	Fan Off Design Performance	28
5.3	High Pressure Compressor	29
5.3.1	HPC Design Results.....	29
5.3.2	HPC Blade Design	32
5.3.3	High Pressure Compressor Off Design Performance.....	32
5.4	Materials and Manufacturing	33
6.	<i>Combustor</i>	35
6.1	Combustor Architecture	36
6.2	Combustor Design	36
6.2.1	Diffuser Design	36
6.2.2	Main Combustor Design	37
6.2.3	Combustor Liner Design.....	40
6.3	Combustor Off Design Performance	42
6.4	Combustor Emissions	42

6.5	Materials And Manufacturing	44
7.	<i>Turbines</i>	45
7.1	Design Approach	45
7.2	High Pressure Turbine	46
7.2.1	HPT Design Results	47
7.2.2	HPT Blade design	50
7.2.3	HPT Off Design Performance.....	51
7.3	Low Pressure Turbine	52
7.3.1	LPT Design Results.....	52
7.3.2	LPT Blade Design.....	55
7.3.3	LPT Off Design Performance	56
7.4	Materials and Manufacturing	57
8.	<i>Mixer, Afterburner and Mixer Ejector</i>	58
8.1	Core-Bypass Mixer	58
8.1.1	Core-Bypass Mixer Design	59
8.2	Afterburner	61
8.2.1	Afterburner Design.....	61
8.3	Mixer Ejector	62
8.3.1	Mixer Ejector Design	63
8.4	Materials and Manufacturing	64
9.	<i>Nozzle</i>	64
9.1	Nozzle Architecture	64
9.2	Nozzle Design	65
9.3	Nozzle Off Design Performance	67
9.4	Materials and Manufacturing	69
10.	<i>Engine Control System</i>	69
11.	<i>Final Engine Flow path and Engine Weight Analysis</i>	70
12.	<i>Conclusion</i>	72
	<i>References</i>	73
	<i>Appendix A- Baseline Engine NPSS Output</i>	A-1
	<i>Appendix B- YJ-2030 NPSS Outputs</i>	B-1
	<i>Appendix C- YJ-2030 Inlet Maps</i>	C-1
	<i>Appendix D: Material Properties</i>	D-1
	<i>Appendix E: Fan Velocity Triangles</i>	E-1
	<i>Appendix F: HPC Velocity Triangles</i>	F-1
	<i>Appendix G: HPT Velocity Triangles</i>	G-1
	<i>Appendix H: LPT Velocity Triangles</i>	H-1

List of Tables

Table I. Supersonic Business Jet Aircraft Specifications [1].....	1
Table II. New York to London SSBJ Mission Summary.....	2
Table III. Comparison of baseline NPSS model and RFP baseline model.	3
Table IV. Subsonic Thrust Estimation requirements	3
Table V. Thrust Requirements at multiple flight conditions.....	4
Table VI. Weighted Pugh Matrix comparing engine architectures.....	7
Table VII. Augmentor vs. No Augmentor Trade Study on a MFTF with $T_{4\max} = 3360\text{ }^{\circ}\text{R}$	8
Table VIII. Final On-Design Cycle Summary Data.....	13
Table IX. Mission Fuel Burn Analysis	14
Table X. Weighted Pugh Matrix comparing Inlet Architectures.	15
Table XI. Inlet Entrance Conditions and Design Choices.	17
Table XII. YJ-2030 Inlet Dimensions, Ramp Angles and station Mach Numbers at design point	18
Table XIII. Inlet Performance at different Mission Stages.	19
Table XIV. Fan Inlet Conditions and Requirements.....	24
Table XV. Fan Design Results Summary	24
Table XVI. Fan Compressor Design Parameter Results.....	25
Table XVII. Fan Compressor Design Blade Angles and Mach Numbers	25
Table XVIII. HPC Design Conditions and Requirements	29
Table XIX. HPC Design Results Summary	29
Table XX. HPC Design Parameter Results.....	31
Table XXI. HPC Design Blade Angles and Mach Numbers	31
Table XXII. Compressor Stress Analysis.	33
Table XXIII. Compressor Material and Manufacturing summary.....	35
Table XXIV. Combustor Architecture Pugh Matrix.....	36
Table XXV. Combustor Inlet Conditions and Requirements	36
Table XXVI. Diffuser Design Results.	37
Table XXVII. Airflow Distribution in the YJ-2030 Combustor.....	37
Table XXVIII. YJ-2030 Main Combustor Design Information.....	38
Table XXIX. YJ-2030 Combustor Swirler Design	40
Table XXX. Final Combustor Performance Parameters.....	40
Table XXXI. Cruise Emissions Performance for the YJ-2030.....	43
Table XXXII. YJ-2030 LTO Emissions Performance.	44
Table XXXIII. General Turbine Parameter Guidelines	46
Table XXXIV. HPT Inlet Conditions and Design Requirements.	47
Table XXXV. HPT Design Results Summary.....	47
Table XXXVI. HPT Design Parameter Results.....	47
Table XXXVII. HPT Design Blade Angles and Mach Numbers	48
Table XXXVIII. LPT Inlet Conditions and Design Requirements.	52
Table XXXIX. LPT Design Results Summary	53
Table XL. LPT Design Parameter Results.....	53
Table XLI. LPT Design Blade Angles and Mach Numbers	53
Table XLII. Turbine Stress Analysis.	57
Table XLIII. Turbine Material and Manufacturing summary.....	58
Table XLIV. Mixer Inlet and Outlet Conditions.....	59
Table XLV. Mixer Design Results.....	60
Table XLVI. Afterburner Inlet Conditions	61
Table XLVII. Afterburner Design Conditions	62
Table XLVIII. Nozzle Design Results.....	65
Table XLIX. WATE++ Results for the YJ-2030.....	71
Table L. YJ-2030 Component and Performance Summary	72
Table LI. AVIMID® N Material Properties [47].....	D-1
Table LII. TI-834 Material Properties [48].	D-1
Table LIII. Ti48Al2Cr2Nb Material Properties [49].	D-1
Table LIV. CMC Material Properties [50].....	D-1

List of Figures

Figure 1. Diagram of Proposed Supersonic Business Jet [1].....	1
Figure 2. Thrust verses Mach Number verses Altitude Diagram.....	4
Figure 3. Mixed Flow Turbofan with Mixer Ejector Nozzle [7].....	6
Figure 4. Variable Cycle Engine with Mixer Ejector Nozzle [7].....	6
Figure 5. FLADE engine [7].....	6
Figure 6. Block Diagram of YJ-2030 Flow path Components.....	8
Figure 7. Fan and HPC polytropic efficiencies verses entry into service year. [16].....	10
Figure 8. HPT and LPT polytropic efficiencies verses entry into service year. [16].....	10
Figure 9. BPR vs. T4 vs. Mission fuel + Engine Weight Trade Study holding HPC PR constant.....	11
Figure 10. HPC vs. T4 vs. Mission fuel + Engine Weight Trade Study holding BPR constant.....	12
Figure 11. HPC vs. BPR vs. Mission fuel + Engine Weight Trade Study holding T4 constant.....	12
Figure 12. YJ-2030 Power Management Schedule.....	14
Figure 13. Inlet recovery verses Mach Number for different inlet compression types. [20].....	16
Figure 14. Two dimensional 3+1 shock Mixed Compression inlet [21].....	16
Figure 15. YJ-2030 2D Drawing of Inlet at Mach 2.1.....	18
Figure 16. Inlet ramp angle schedule and pressure recovery verses Mach Number.....	18
Figure 17. Conditions leading to Buzz [22].....	20
Figure 18. Inlet Distortion [15].....	20
Figure 19. Inlet Buzz-Distortion Performance.....	21
Figure 20. Compressor Coordinate System [15].....	22
Figure 21. Guidelines on the Range of Compressor Parameters [15].....	23
Figure 22. Aerodynamic parameters as a function of blade radius for the 1 st (left) and last fan stage (right).....	26
Figure 23. Fan Flow path drawing.....	26
Figure 24. Twist of the 1 st and last stage fan rotor blades as a function of blade radius.....	27
Figure 25. Scaled Fan Compressor Map for the YJ-2030 with the Mission Operating line overlaid.....	28
Figure 26. Aerodynamic parameters as a function of blade radius for the 1 st (left) and last HPC stage (right).....	30
Figure 27. HPC Flow Path Drawing.....	30
Figure 28. Twist of the 1 st and last stage HPC rotor blades as a function of blade radius.....	32
Figure 29. Scaled HPC Compressor Map for the YJ-2030 with the Mission Operating line overlaid.....	33
Figure 30. Stator Sectors for a J-85 engine.....	35
Figure 31. Comparison of traditional blade locking mechanism verses a Blisk [29] [28].....	35
Figure 32. Diagram of a annular gap igniter plug.....	38
Figure 33. YJ-2030 Combustor Flow path.....	39
Figure 34. TAPS II Dome Configuration.....	39
Figure 35. Cooling Air verses Cooling Effectiveness relationship [15].....	41
Figure 36. Film Cooling Method [15].....	41
Figure 37. Combustor Liner with effusion hole surrounding the primary dilution holes [36].....	41
Figure 38. Typical Relight Envelope with YJ-2030 mission conditions overlaid.....	42
Figure 39. Turbine Labeling Convention [15].....	46
Figure 40. Aerodynamic parameters as a function of blade radius for the 1 st (left) and 2 nd HPT stage (right).....	48
Figure 41. HPT Smith Chart [22].....	49
Figure 42. HPT Flow Path Drawing.....	49
Figure 43. Twist of the 1 st and last stage HPT nozzle and rotor blades as a function of blade radius.....	50
Figure 44. Cooling Scheme for a HPT Stage [40].....	51
Figure 45. Five Pass Inner Blade Cooling.....	51
Figure 46. Scaled HPT Map for the YJ-2030 with the Mission Operating line overlaid.....	52
Figure 47. Aerodynamic parameters as a function of blade radius for the 1 st (left) and 2 nd LPT stage (right).....	54
Figure 48. LPT Smith Chart [22].....	54
Figure 49. LPT Flow path Drawing.....	55
Figure 50. Twist of the 1 st and last stage LPT nozzle and rotor blades as a function of blade radius.....	55
Figure 51. Scaled HPT Map for the YJ-2030 with the Mission Operating line overlaid.....	56
Figure 52. GE Passport Mixer and Center cone [41].....	58
Figure 53. Typical Mixer labeling scheme [42].....	60

Figure 54. GE Affinity Mixer [23].....	60
Figure 55. EJ200 Afterburner architecture [15].....	61
Figure 56. JT8D ejector nozzle showing cruise (left) and takeoff (right) operation. [43].....	62
Figure 57. NASA Mixer Ejector Model [7]......	63
Figure 58. Modified Mixer Ejector Model.....	63
Figure 59. Typical Nozzle Dimensions and Parameters [22].	65
Figure 60. Drawing of the nozzle flow path at different operating conditions	66
Figure 61. CD Nozzle Actuation Schematic [22].	66
Figure 62. Chevron Nozzle Pattern [15].	67
Figure 63. YJ-2030 Afterbody Drag Relationship [20].	68
Figure 64. YJ-2030 Nozzle Performance at different flight conditions.....	68
Figure 65. Effect of variable A8 on fan operating line [22].....	68
Figure 66. YJ-2030 Nozzle Area Schedule.....	69
Figure 67. CMC Divergent Nozzle Flaps on a F-16 Nozzle [44].....	69
Figure 68. YJ-2030 FADEC Block Diagram.....	70
Figure 69. YJ-2030 WATE++ Flow path.	71
Figure 70. Baseline Engine NPSS Model Output	A-1
Figure 71. YJ-2030 NPSS Output at Design point	B-1
Figure 76. YJ-2030 NPSS Output at Takeoff	B-2
Figure 77. YJ-2030 Inlet Maps.	C-1
Figure 78. Fan Hub Velocity Triangles.....	E-1
Figure 79. Fan Mean-line Velocity Triangles.....	E-2
Figure 80. Fan Tip Velocity Triangles.....	E-3
Figure 81. HPC Hub Velocity Triangles.....	F-1
Figure 82. HPC Mean line Velocity Triangles.....	F-2
Figure 83. HPC Tip Velocity Triangles	F-3
Figure 84. HPT Hub Velocity Triangles.....	G-1
Figure 85. HPT Mean line Velocity Triangles.....	G-2
Figure 86. HPT Tip Velocity Triangles	G-3
Figure 87. LPT Hub Velocity Triangles	H-1
Figure 88. LPT Mean Line Velocity Triangles.....	H-2
Figure 89. LPT Tip Velocity Triangles.....	H-3

Acknowledgements

The team would like to thank Dr. Seitzman and Mr. Denney for advising the team. Taking time out of your busy day to give the team suggestions and advice proved invaluable.

1. Introduction

The YJ-2030 is a candidate engine for a new supersonic business jet. The business jet shall travel from Europe to North America and back, in one day, carrying a maximum of twelve passengers. The design cruise point of the engine is Mach 2.1 at 40,000 feet altitude, as stated by the AIAA Request for Proposal (RFP) [1]. The aircraft has a maximum fuel capacity of 97,400 pounds. A diagram of the proposed supersonic business jet and more through aircraft specifications are shown in Table I and Figure 1.

Table I. Supersonic Business Jet Aircraft Specifications [1]

General characteristics	
Crew	2
Capacity	8 – 12 passengers
Length	135.6 ft (41.33 m)
Wing span	64.2 ft (19.57 m)
Height	21.2 ft (6.46 m)
Wing area	1,200 ft ² (111.5 m ²)
Max. take-off weight	146,000 lbm (40,823 kg)
Power plant	2 × low bypass ratio turbofans; 21,700 lbf (96.53 kN) each
Performance	
Maximum speed	1,720 knots (Mach 3; 1980 mph; 3186 km/h)
Cruise speed	1204 knots (Mach 2.1; 1386 mph; 2230 km/h) @ 40kft
Range	At Mach 0.95: 4,600 nm (5,300 mi; 8,500 km)
Service ceiling	51,000 ft (16,000 m)

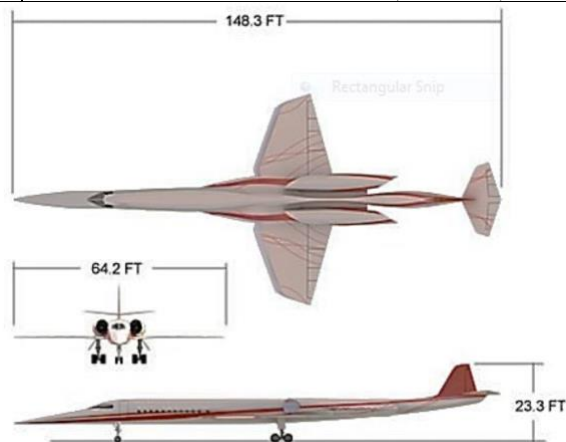


Figure 1. Diagram of Proposed Supersonic Business Jet [1]

The subsequent sections detail the specific requirements the YJ-2030 must meet, the YJ-2030 cycle, specific component design for the proposed engine, a flow path and weight analysis and finally, a performance check against the engine requirements.

2. Requirements Definition

To begin YJ-2030 design, the team broke down the requirements from the performance and airframer developers. A baseline mission, as well as a baseline engine model, are created as a way to quantitatively measure the proposed engine. In this design, the requirements are derived from the AIAA RFP document, International Civil Aviation Organization (ICAO) documentation and Federal Aviation Administration (FAA) documentation. Engine size, engine thrust, engine emissions and engine noise are all derived as requirements in the sections below.

2.1 Mission Definition

In order to better measure the YJ-2030 performance, a sample New York to London mission was created based on general business jet parameters. Noise restrictions also influenced the mission. As shown below in Table II, the aircraft will takeoff from New York and climb to 40,000 feet. Then, the aircraft will begin a Boomless cruise at Mach 1.15, while it travels over the northeastern United States and Canada. Once the aircraft is clear of land, it will begin a cruise-climb at Mach 2.1 beginning at 40,000 feet and ending at 50,000 feet. Once the aircraft reaches the British Isles, it will decelerate and begin an economy cruise at Mach 0.98 before descending, approaching and landing in London. This mission is similar to a typical high speed civil transport (HSCT) economic mission [2].

Table II. New York to London SSBJ Mission Summary

Mission stage	Altitude begin (ft)	Altitude end (ft)	Mach Number	Time (min)	Distance (miles)	Total distance (miles)
Taxi	0	0	0	10	0.0	0.0
Takeoff	0	1500	0	2	3.0	3.0
Climb & Accelerate to 40k	1500	40,000	N/A	20	115.6	118.6
Overland Boomless Cruise	40,000	40,000	1.15	90	1138.5	1257.1
Oversea Cruise	40,000	50,000	2.1	70	1617.0	2874.1
Overland Economy Cruise	50,000	50,000	0.98	35	377.3	3251.3
Descend	50,000	1500	N/A	30	184.3	3435.7
Approach and Land	1500	0	N/A	5	10.0	3445.7
Taxi In	0	0	0	5	0.0	3445.7

2.2 Baseline Engine

Numerical Propulsion System Simulation (NPSS) was used to model the baseline engine given in the RFP [3]. NPSS was chosen as the modeling environment over similar programs like GasTurb because NPSS allows the user to modify elements and write custom programs that interact with the cycle. This allows for more flexibility to perform overall mission trade studies and gives the option to include estimations for installed performance and additional losses from maps. Some functionality is lost when using NPSS over GasTurb, such as built in weight estimation and initial turbomachinery design, however, these functions can be made up through the use of Weight

Analysis of Turbine Engine (WATE++) for engine weight estimation and team generated design codes for turbomachinery design.

The baseline engine was modeled using the cycle parameters given in the RFP. The major difference between the RFP baseline model and NPSS baseline model is the use of a non-stratified fan in the NPSS model for better off-design model convergence; The fan pressure ratio was set to 1.9 to account for the non-stratified fan. The differences between the NPSS model and the RFP baseline model are outlined below in Table III. Less than a 1% error was calculated in the engine mass flow and in the thrust specific fuel consumption (TSFC) between the two models, thus validating the baseline NPSS model. The sea level static output of the NPSS model is shown in Appendix A.

Table III. Comparison of baseline NPSS model and RFP baseline model.

	Engine Mass Flow (lbm/s)	SLS Thrust (lbf)	TSFC (lbm/(hr*lbf))
NPSS	477.2	21698.9	0.4719
RFP baseline	479	21698.9	0.4745
% Error	0.376	0.00	0.548

2.3 Thrust requirements

Following the creation of the baseline model, thrust requirements may be derived for the YJ-2030. First, the required takeoff performance is given by the RFP, 21,700 lbf [1]. The thrust required for subsonic points, such as climb, decent and approach, are calculated using the NPSS baseline engine. In these cases, the baseline engine is run at the mission point at a specific throttle position to estimate the thrust required. For example, at the climb point, the baseline engine is run at 20,000 feet, Mach 0.70 at 99% fan speed to estimate the climb thrust. This process was repeated for the descent point and approach point. For taxi thrust, the ICAO landing take-off (LTO) cycle definition of taxi thrust is used: 5.8% of takeoff thrust. A summary of the thrust requirements and method of derivation is shown below in Table IV.

Table IV. Subsonic Thrust Estimation requirements

Condition	Altitude (ft)	MN	Baseline engine N %	Thrust (lbf)	Method of Derivation
Takeoff	0	0	N/A	21700	RFP
Climb	20,000	0.7	99	9570	Baseline Model
Descent	10,000	0.7	60	2400	Baseline Model
Approach	2000	0.25	60	6000	Baseline Model
Taxi in/out	0	0	N/A	1258	LTO definition

The transonic and supersonic thrusts may be derived by recreating and extrapolating the thrust verses altitude verses Mach number figure provided in the RFP [1]. In steady level flight, thrust will be equal to drag. Therefore, the

figure is recreated by calculating the drag at the different points using the dynamic pressure, wing area and guessing a coefficient of drag value. Coefficient of drag was iterated until the curves matched those of the RFP. Then, the coefficient of drag was extrapolated to Mach 2.1 and Mach 3.0 to find thrust relationship at those points. A reproduced plot with Mach 2.1 and Mach 3.0 curves is shown below in Figure 2. The black points in the figure represent comparison points to ensure that the recreated figure and RFP figure match.

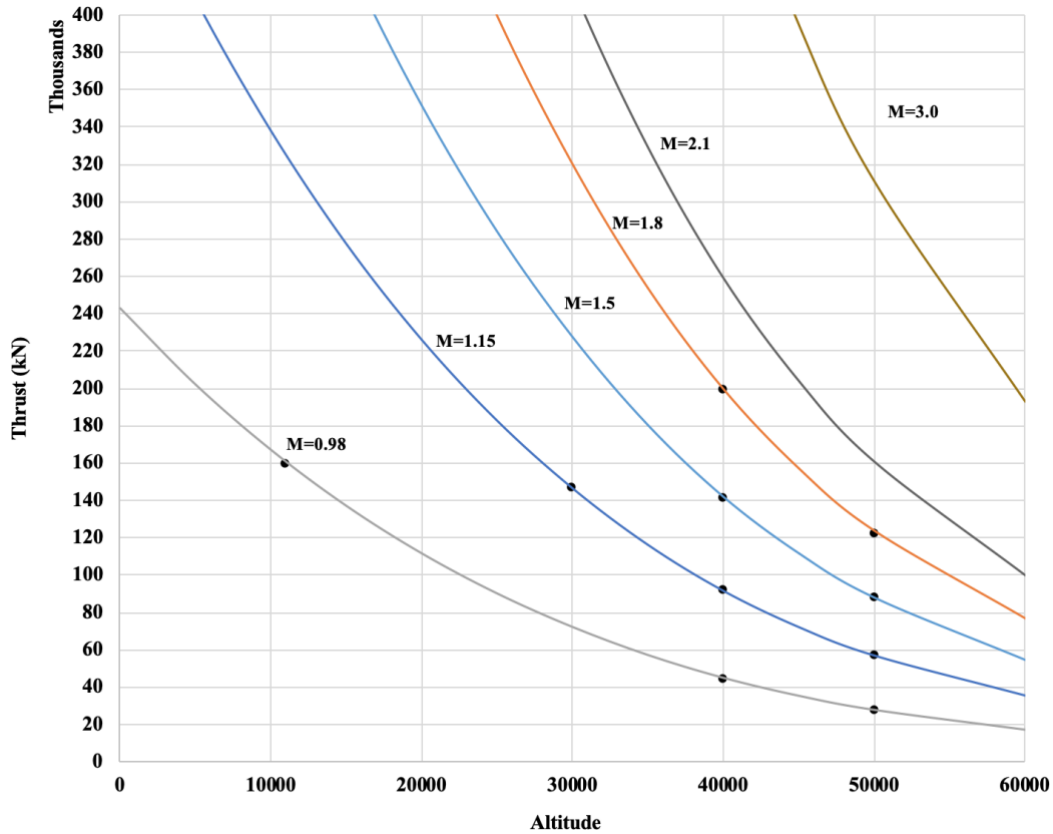


Figure 2. Thrust versus Mach Number versus Altitude Diagram

A table summarizing the thrust requirements is shown below in Table V. The YJ-2030 shall produce excess thrust at all of these flight conditions.

Table V. Thrust Requirements at multiple flight conditions.

MN	Altitude (ft)	Total Thrust Required (N)	Thrust Required for 1 Engine (lbf)
0.98	40,000	45083	5068
0.98	50,000	27956	3142
1.15	40,000	91182	10249
1.15	50,000	56542	6356
1.5	40,000	141927	15953
1.8	40,000	199622	22438
2.1	40,000	258769	29000
2.1	45,000	203665	22900
3	50,000	311102	35000

2.4 Additional Requirements

Noise around airports has been of particular concern over the past decade. The RFP states the aircraft and its engines shall meet the most stringent noise constraints. The newest legislation from the FAA sets out Stage 5 noise constraints [4]. Stage 5 noise constraints require a reduction of 17 EPNdB relative to Stage 3 [5]. Aircraft noise is difficult to determine without conducting flight tests. Instead, the noise constraint may be represented by a nozzle exit velocity constraint. Boeing has predicted that a reduction of 10 to 20 EPNdB from Stage 3 could be achieved if the exit nozzle velocity is 1100 ft/s or lower [6].

Next, all engines, including supersonic engines, must meet the emissions requirements laid out by ICAO. These requirements dictate the amount of emissions in mass per unit thrust for a typical landing take off cycle. However, emissions are not only limited to the LTO cycle; High altitude supersonic emissions have been a concern due to the climate change effects from a high altitude release of NO_x. In the High Speed Research (HSR) program, a value of 5 lb of NO_x per klb of fuel has been set as a goal for future supersonic cruise emissions [7]. The YJ-2030 shall meet this cruise emissions requirement as well as the LTO NO_x emissions requirement.

Finally in the RFP, it was stated that the engine is preferred to stay within the existing nacelle envelope and be lighter than the current baseline engine. This is defined as a 49.2'' fan diameter, a total nacelle length of 34 feet and a baseline engine weight of 4500 lbm [1].

3. Cycle Analysis

During cycle analysis, the YJ-2030 architecture is chosen based on the mission, regulatory and aircraft requirements. Then, the architecture is optimized for maximum aircraft range while meeting the requirements. This optimization includes choosing the fan pressure ratio (FPR), bypass ratio (BPR), overall pressure ratio (OPR) and turbine inlet temperature (T₄) for the YJ-2030.

3.1 Cycle Architecture

The first step in cycle analysis is selecting an engine architecture. Three engine architectures, that are marked as needing further exploration for use in commercial supersonic transports, are investigated [7].

The first architecture explored was the mixed flow turbofan (MFTF) with a mixer ejector nozzle for noise suppression, shown in Figure 3. This architecture is the simplest of the four cycles while providing middle of the road fuel efficiency across the flight regime. The MFTF is used as an architecture in the RFP baseline engine and the GE

Affinity Engine, which will power Aerion’s new supersonic business jet [8]. There are noise concerns with this architecture, but if the mixer ejector nozzle is sized properly, Stage 5 noise limits can be met.

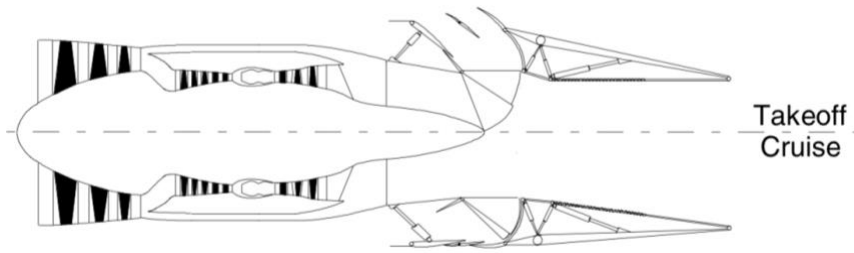


Figure 3. Mixed Flow Turbofan with Mixer Ejector Nozzle [7]

The next architecture explored was the Variable Cycle Engine (VCE) with a mixer ejector nozzle for noise suppression, shown in Figure 4. A VCE architecture allows for the engine to change the amount of air mass going through its core. This architecture is quite complex and heavy, but offers a lower mission fuel burn and allows for a lighter mixer ejector nozzle. This engine architecture has not been used on any aircraft, however, GE Aviation has produced two VCE testbeds, one in the 1980’s called the YF-120 and one recently, called the ADVENT (ADaptive Versatile ENgine Technology) Engine [9].

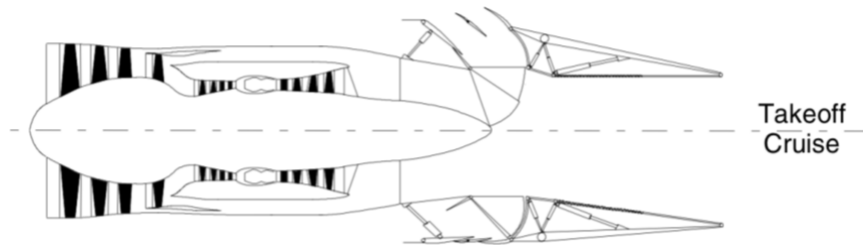


Figure 4. Variable Cycle Engine with Mixer Ejector Nozzle [7]

The third architecture investigated is the FLADE engine, shown in Figure 5. This architecture features an outer bypass duct with a fan tip extended into it. This duct offers acoustic shielding from the core exhaust and offers an alternative to using a mixer ejector nozzle. From NASA studies, this architecture comes out to be the heaviest and largest of the engines due to the large outer bypass duct needed for noise attenuation [7]. No physical FLADE engines have been produced to date.

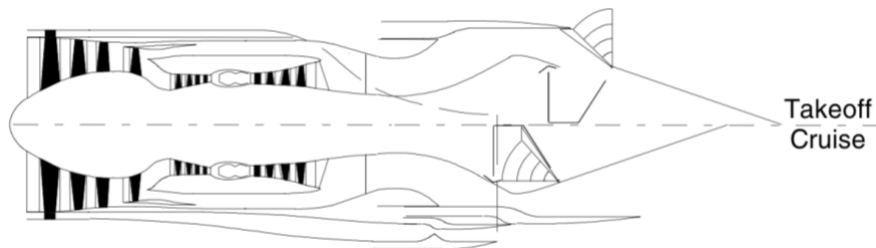


Figure 5. FLADE engine [7]

The architectures discussed above are compared in a weighted Pugh Matrix, shown in Table VI.

Table VI. Weighted Pugh Matrix comparing engine architectures

	Size & Weight (2)	Fuel Burn (3)	Complexity (1)	TRL (2)	Total
VCE	2	3	1	2	18
FLADE engine	1	1	2	1	9
MFTF	3	2	3	3	21

The results show that the MFTF is the best engine architecture suited for the mission. The technology readiness level (TRL) of this architecture is estimated to be level 9.

3.2 Addition of Augmentor

The use of an augmentor in a commercial aircraft is generally not preferred due to weight, length and cost concerns; Nonetheless, an augmentor is investigated for use on the YJ-2030 to achieve the thrust needed to reach the max speed of the aircraft, Mach 3.0. In this configuration, an augmentor provides two main benefits: minimizing the fan diameter and preventing the high pressure (HP) spool from overspeeding. The addition of an augmentor will require a variable area nozzle, with a variable throat area. The variable throat area allows for control of the fan stall margin, something required during augmentor use. Without it, the fan would stall due to the increased backpressure.

From analyzing the Brayton cycle T-s diagram, it can be seen that increasing T_4 , keeping everything else constant, will increase specific thrust. Therefore, at the design point, if T_4 is increased, the engine mass flow and thus fan diameter will decrease for a constant thrust required. Without an augmentor, the design point T_4 will be set below the maximum T_4 limit, so that at Mach 3, the T_4 limit is hit and the thrust required at this speed is produced. This oversizes the engine and overspeeds the HP spool at Mach 3.0 compared to the Mach 2.1 design point. This in turn requires the compressor design speed to be at Mach 3.0, a flight condition not often reached in typical missions.

With an augmentor present, the T_4 limit may be set at design point and a HP spool rpm limit can be implemented. Then the augmentor can be used to produce the necessary extra thrust to fly at speeds greater than Mach 2.1.

Additional disadvantages of using an augmentor include: high fuel flows during use and a pressure loss across the afterburner, which increases mission fuel burn. A small trade study, shown in Table VII, is conducted on an unoptimized MFTF to see the effect of an augmentor on the cycle.

Table VII. Augmentor vs. No Augmentor Trade Study on a MFTF with $T_{4\max} = 3360\text{ }^{\circ}\text{R}$

	No Augmentor Configuration	Augmentor Configuration
Fan Diameter (in)	56	49
Length Addition (in)	-	50
Bare Engine Weight (lbm)	5200	5300
T_4 ($^{\circ}\text{R}$) @ Mach 2.1	2883	3360
T_4 ($^{\circ}\text{R}$) @ Mach 3.0	3360	2907
HPC Rpm % @ Mach 2.1	100	100
HPC Rpm % @ Mach 3.0	113	101
Fuel Flow (lbm/hr) @ Mach 2.1	30386	30785

Table VII confirms that the addition of an afterburner reduces fan diameter and, with the proper controls implemented, prevents a HP spool overspeed. The bare engine weight gain with an augmentor is only 100 lbm due to the engine smaller diameter and the use of Ceramic Matrix Composites (CMC) in the afterburner section; But the length addition is quite significant, 50 inches. Furthermore, the Mach 2.1 fuel burn increases by 1.3% with an augmentor present. The fuel burn increase can be counteracted by using the variable nozzle throat area to control the fan operating line and improve TSFC. In the end, the engine length and mission fuel burn disadvantages are overlooked so that the 49” fan diameter requirement can be met easier.

3.3 Cycle Optimization

3.3.1 Approach

Following the selection of the engine architecture, cycle optimization may begin. A diagram of the cycle component blocks is shown below in Figure 6.

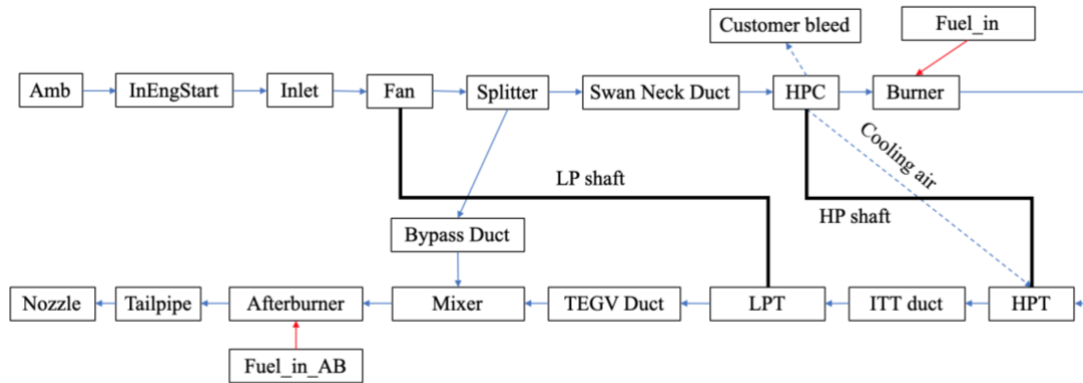


Figure 6. Block Diagram of YJ-2030 Flow path Components

FPR, BPR, HPC PR and T_4 are varied to optimize the cycle. It was decided that the most optimum cycle is one that has the lowest mission fuel burn plus aircraft engine weight, while fulfilling all of the customer requirements. Mission fuel burn plus aircraft engine weight was used instead of just mission fuel burn because a certain combination

of the design parameters may have an improved mission fuel burn, but the increase in engine weight will offset the fuel burn weight savings. This method ensures that the chosen cycle maximizes aircraft range.

Using cycle parameters from each trade study combination, an estimated bare engine weight could be calculated using an formula derived by Torenbeck [10]. Applying Equation 1 to the baseline engine yields an engine weight of 4790 lbm, an overestimation of 6%. This is deemed acceptable for preliminary design.

$$W_{\text{engine}} = \left[\frac{10 \text{ OPR}^{0.25} \dot{m}_{\text{T.O.}}}{1 + \text{BPR}} + 0.12 \frac{F_{\text{T.O.}}}{g} \left(1 - \frac{1}{\sqrt{1 + 0.75\text{BPR}}} \right) \right] \quad (1)$$

Using a simplified equation, rather than using the more accurate WATE++ program was done due to runtime concerns and convergence errors with WATE++, especially within the turbomachinery. After the final cycle was selected, a WATE++ model was generated for an accurate, final weight representation.

3.3.2 Assumptions

In order to set the T₃ limit, a quick literature review of compressor materials was conducted. Nickel superalloys can operate in temperatures upwards of 2100 °R [11]. However, to improve the HPC lifetime, a T₃ limit lower than this should be implemented. Thus, a T₃ limit of 2000 °R is reasonable.

Cooling flow for the HPT was varied in NPSS, using a process outlined by Gauntner, for each cycle based on a blade temperature selection [12]. Operating blade temperature was decided by analyzing the trends in Ceramic Matrix Composites (CMC) and thermal barrier coatings (TBC). In 2016, GE Aviation stated that CMC parts can “operate at 2,400 degrees Fahrenheit” or about 2850 °R [13]. Additionally, turbine inlet temperatures have steadily rose approximately 100 °R per decade over the past 20 years [14]. Finally, advanced TBCs have been predicted to increase blade operating temperature by approximately 180 °R [15]. Using these technologies and trends, the team predicts that the maximum blade temperature in the HPT will be 3100 °R, by 2030. If T₄ is higher, cooling flow will be needed to cool the blade to 3100 °R. The LPT will require no cooling due to a lower operating temperature and the use of advanced alloys.

Fan diameter was calculated in the NPSS model by assuming an inlet fan MN of 0.6 at design point and a hub to tip ratio of 0.3. These design choices are taken into account when designing the fan.

Figure 7 and Figure 8 show the polytropic efficiency of turbomachinery over time. The fan, HPT and LPT polytropic efficiencies are set below the estimated trendlines because their designs prioritize a low stage count over

high efficiency to save weight. Additionally, it is the teams belief that the polytropic turbine efficiencies are overestimated in these figures. The HPC efficiency is chosen based on the trend line.

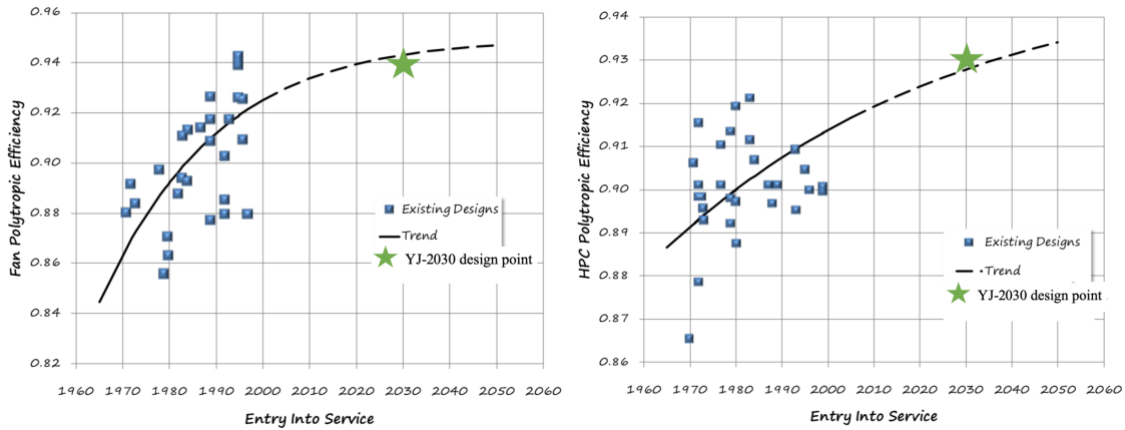


Figure 7. Fan and HPC polytropic efficiencies verses entry into service year. [16]

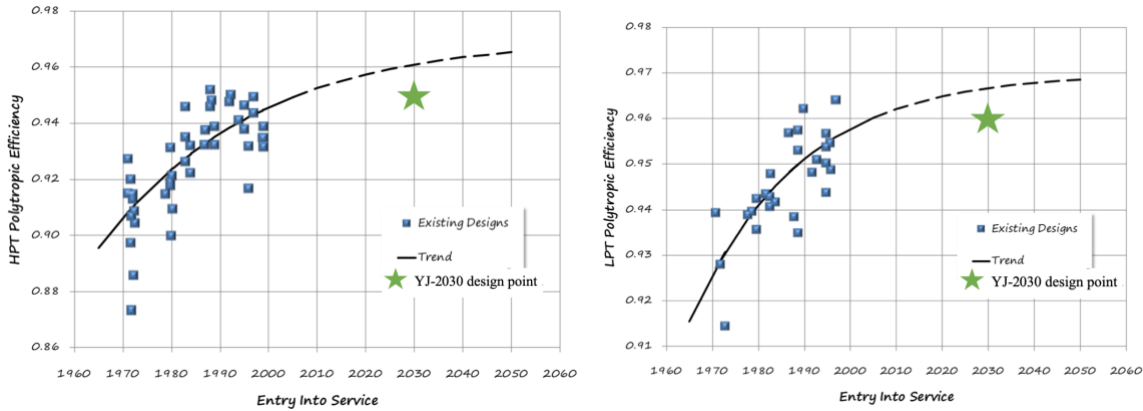


Figure 8. HPT and LPT polytropic efficiencies verses entry into service year. [16]

Overboard bleed, used for cabin pressurization, is calculated by assuming a maximum of 15 passengers and crew onboard at any single time. Per Timbly, a 1 lbm/min/passenger fresh airflow rate will ensure that the cabin will not be stuffy [17].

The shaft offtake for the YJ-2030 is assumed to be 110 horsepower from the HP spool throughout the entire mission. This horsepower offtake is slightly more than the HP spool offtake for the V2500 engine, a commercial transport engine [18]. The offtake was higher in the YJ-2030 engine to account for the power required to control the inlet ramps and the variable nozzle. Additionally, the shaft mechanical efficiencies were improved from the baseline engine to 99.5%, a reasonable value for 2030 entry to service.

Finally, since the engine is a MFTF, the mixer extraction ratio, the ratio of the total pressures of the two mixing streams, is set to 1.0. This choice keeps mixing losses to a minimum [19]. The selection of a single mixer

extraction ratio for all cycles, constrains the FPR to a single value based on a BPR, T4 and HPC PR choice. This reduces the number of free variables to 3.

3.3.3 Cycle Optimization Results

The BPR vs T4 vs mission fuel + engine weight plot is shown in Figure 9. In this study, the cooling air flow was varied so that the first stage HPT would have a blade temperature of 3100 °R. Increasing the BPR of the engine, decreased mission fuel burn due to the increased propulsive efficiency of the engine, however, increasing the BPR, also increased the T₃, fan diameter and weight of the engine. Increasing the T₄ of the engine, increases mission fuel burn due to the higher amount of cooling flow required, but decreased the fan size due to the higher specific thrust of the cycle. Increasing T₄ also significantly increased cruise emissions. Emissions, T₃ and fan diameter limits are drawn on the plot and the minimum point of mission fuel burn + engine weight is chosen. This point is a BPR of 0.85 and T₄ of 3366 °R.

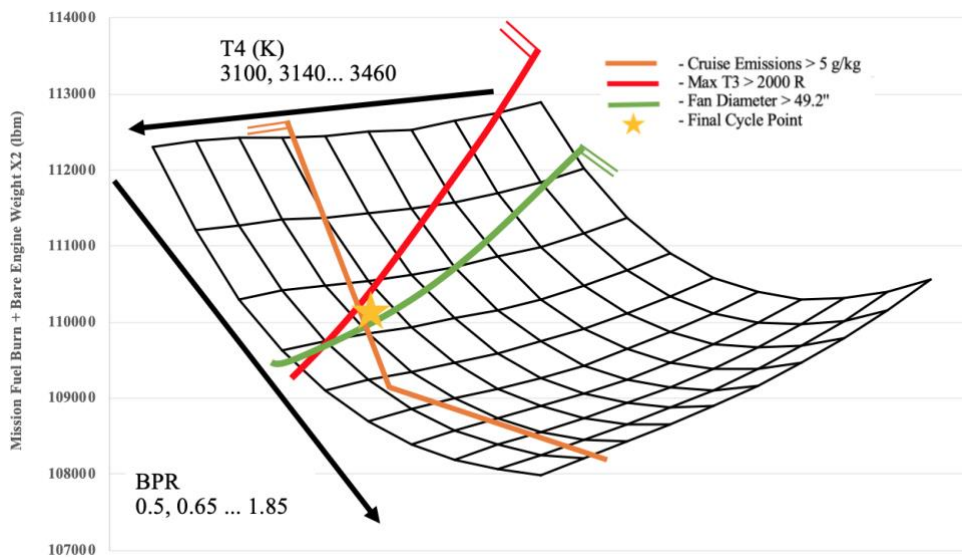


Figure 9. BPR vs. T4 vs. Mission fuel + Engine Weight Trade Study holding HPC PR constant.

The HPC vs T4 vs mission fuel + engine weight plot is shown in Figure 10. Just as the study above, cooling flow is varied for each cycle, while holding a constant blade temperature of 3100 °R. When HPC PR is increased, it increases the thermal efficiency of the engine, therefore decreasing mission fuel burn. However, increasing HPC PR also adds more stages to the HP spool, increasing engine weight. This tradeoff is why the constant T₄ lines curve. Just as above, increasing T₄ increases mission fuel burn due to more cooling flow required, but decreases the fan diameter due to a higher specific thrust. In this study it can be seen that T₃ is highly dependent on the HPC PR choice. Again, cruise emissions and fan diameter are mostly driven by the T₄ selection, but choosing a higher HPC PR will also lead

to increased emissions and an increased fan diameter. Emissions, T_3 and fan diameter limits are drawn on the plot and the minimum point of mission fuel burn + engine weight is chosen. This point is a T_4 of 3366 °R and HPC PR of 8.5.

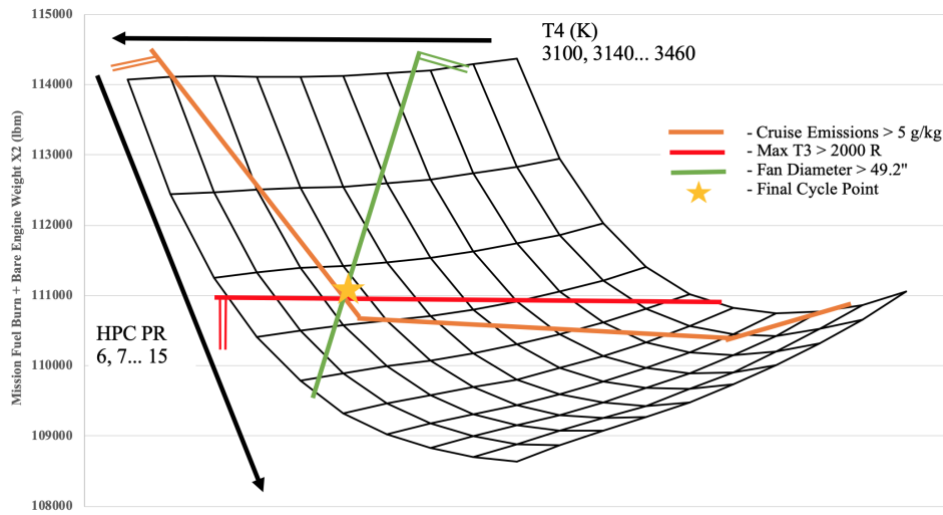


Figure 10. HPC vs. T_4 vs. Mission fuel + Engine Weight Trade Study holding BPR constant.

Finally, the HPC vs BPR vs mission fuel + engine weight plot is shown in Figure 11. In this study T_4 is held constant but cooling flow is still varied to keep a constant HPT blade temperature. For a constant BPR or HPC PR, the figure shows that there is an optimum point for range. Essentially, continuing to increase these parameters may increase engine efficiency, but at the expense of increasing the weight of the engine to the point where range actually decreases. Emissions, T_3 and fan diameter limits are drawn on the plot and the minimum point of mission fuel burn + engine weight is chosen. This point is a BPR of 0.85 and HPC PR of 8.5.

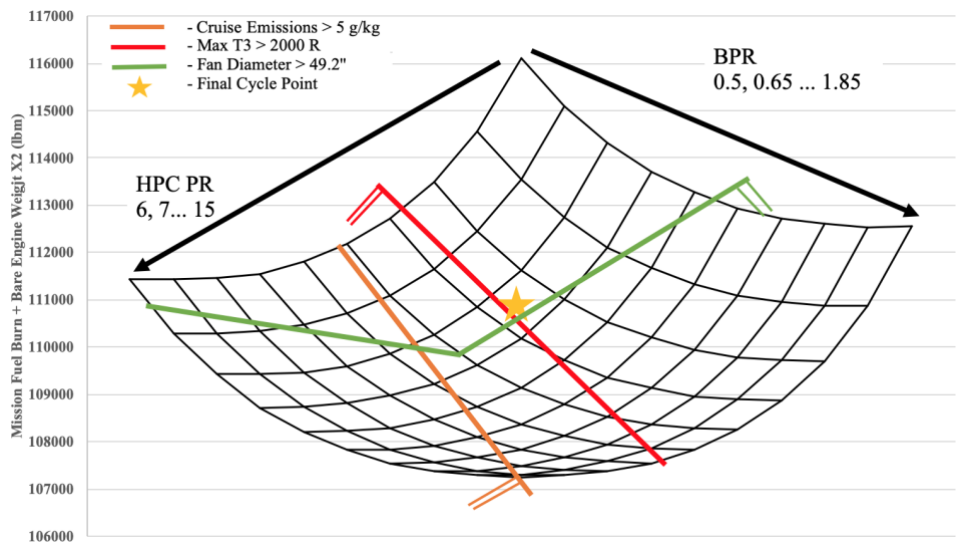


Figure 11. HPC vs. BPR vs. Mission fuel + Engine Weight Trade Study holding T_4 constant.

For all trade studies, the Emissions, T_3 and fan diameter are drawn as linear relationships to estimate the limits. If more computing power was available, thousands of cases would be run in the design space so that these limits could be more accurately drawn.

3.4 Final Cycle Summary

From the trade study results above, a final thermodynamic cycle is selected and its parameters are summarized below. Note that the installed thrust and installed TSFC include losses from inlet and nozzle drags as well as customer bleed and HP spool offtake. The cooling flow percentages were determined using CoolIt to match to a HPT blade temperature of 3100 °R.

Table VIII. Final On-Design Cycle Summary Data

Cycle Summary Data	
Design MN	2.1
Design Altitude (ft)	40,000
Design Fan Mass Flow (lbm/s)	658.414
Design Gross Thrust (lbf)	72000.3
Design Bypass Ratio	0.85
Design Installed Net Thrust	29001.6
Design Installed TSFC (lbm/hr/lbf)	1.0984
Design Overall Pressure Ratio	27.89
Design T4 (°R)	3366.0
Design Core Pressure Ratio	8.5
Design Fan / LPC Pressure Ratio	3.33
Design Chargeable Cooling Flow (%@25)	0.73%
Design Non-Chargeable Cooling Flow (%@25)	2.06%
Design Polytropic Efficiency for Each Compressor	Fan: 0.94, HPC: 0.93
Design Adiabatic Efficiency for Each Turbine	HPT: 0.9564, LPT: 0.9639
Design HP & LP Shaft RPM	LP shaft: 6913 HP shaft: 14485
Design HP/LP Shaft Off-take Power Design Customer Bleed Flow	1% customer bleed 110 HP Off-Take from HP shaft

After the optimal cycle is solidified, the YJ-2030 mission performance is determined. The cycle model is run in off design mode using mission profile outlined in the section above. The mission fuel burn for each mission stage is computed and summarized in Table IX.

Table IX. Mission Fuel Burn Analysis

Mission stage	Altitude (ft)	Mach Number	Engine Thrust (lbf)	Fuel Flow (lbm/hr)	Time	Fuel Burned in Segment (lbm)
Taxi	0	0	1258	948.4	00:15	474
Takeoff	0	0	21700	10927.2	00:02	728
Climb & Accelerate to 40k	20,000	0.7	9570	6928.9	00:20	4619
Overland “Boomless” Cruise	40,000	1.15	10250	9222.3	01:30	27667
Oversea Cruise	45,000	2.1	22900	25062.7	00:60	50125
Overland Economy Cruise	51,000	0.98	3142	2654.4	00:55	4866
Descend	10,000	0.7	2400	3423.9	00:30	3424
Approach and Land	2000	0.25	6000	3290.7	00:05	548
Taxi In	0	0	1258	948.4	00:10	316
Total:					4:57	92769

From the table, it can be seen that the aircraft can complete the New York City to London mission in around 5 hours with 5% fuel reserves. The mission time is about 2 hours quicker than if it was flown commercially, in a no wind situation. Range can be extended to over 5000 nautical miles if the aircraft is flown at Mach 0.98 at 40,000 feet. Copies of the on design and off design cycles are included in Appendix B. The NPSS model can be shared upon request of the authors.

Following the mission analysis, the maximum thrust of the engine was measured across the flight envelope. This was done by imposing cycle limits such as: a T4 limit of 3410 °R, a N1 limit of 103%, a N2 limit of 101% and a N1c limit of 100%. The results of the maximum thrust study may be seen below. Below Mach 1.15, the corrected fan speed limits engine thrust. During supersonic acceleration, the uncorrected fan spool speed limits thrust. At design point, T4 limits the thrust. Finally, at Mach 3.0, T3 or HP spool speed limits the engine performance and the afterburner must be used. The “theta break” of the engine occurs around Mach 1.15, 40,000 feet or a T2 of 494 °R.

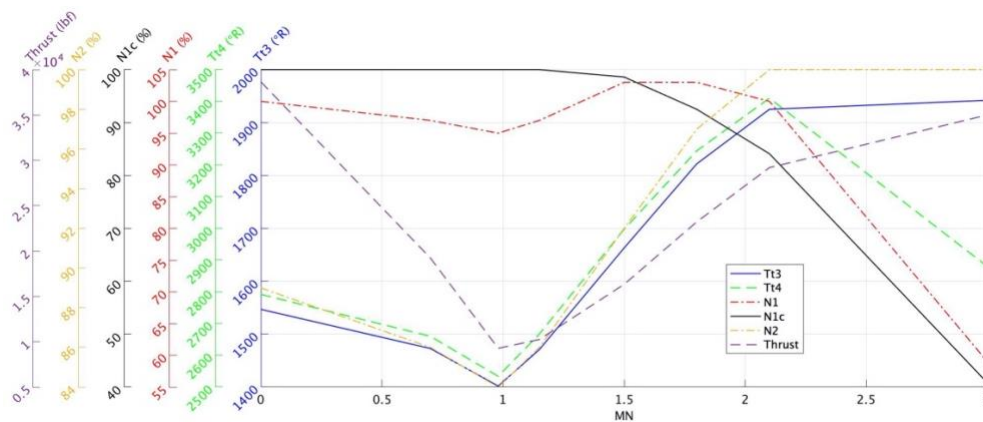


Figure 12. YJ-2030 Power Management Schedule

4. Inlet

The YJ-2030 features a 4 shock, 2-D mixed compression supersonic inlet. The inlet supplies the fan of the engine with the required amount of air mass, at an appropriate Mach Number, with little distortion for each throttle setting within a flight envelope. In supersonic systems, the performance of the inlet is of utmost importance due to the large effects inlet pressure recovery and installation effects play on the TSFC. Low weight, a small envelope, high reliability and easy maintainability are preferred characteristics for a jet engine inlet. Thus, commercial supersonic inlet design is a multi-faceted compromise between many requirements rather than a single optimal design.

4.1 Inlet Architecture

To begin preliminary inlet design, basic inlet architectures are investigated and a trade study is performed. A variable two dimensional ramp inlet, used in the Concorde, a variable axisymmetric spike inlet, used in the SR-71, and a fixed geometry inlet, used in the F-35, are all evaluated in a weighted Pugh matrix.

Table X. Weighted Pugh Matrix comparing Inlet Architectures.

	Performance Across Flight Envelope (3)	Weight & Length (1)	Reliability (2)	Total
Variable Spike Inlet	3	3	2	16
Variable 2D	5	2	4	25
Fixed Geometry Inlet	1	5	5	18

From Table X, it is evident that the variable 2D inlet is suited best for the application. External, internal and mixed compression inlets are all investigated. Figure 13 shows the pressure recovery of the inlet as a function of Mach Number, number of shocks and inlet type. With the engine operating at a maximum speed of Mach 3.0, a mixed compression engine is needed to ensure a high enough pressure recovery so that the engine does not to be oversized to meet thrust requirements at max speed. A 3 oblique shock, 1 normal shock inlet is chosen for its 95% pressure recovery performance at MN=2.1. An additional shock would increase the weight of the inlet significantly while only offering a 1% increase in pressure recovery.

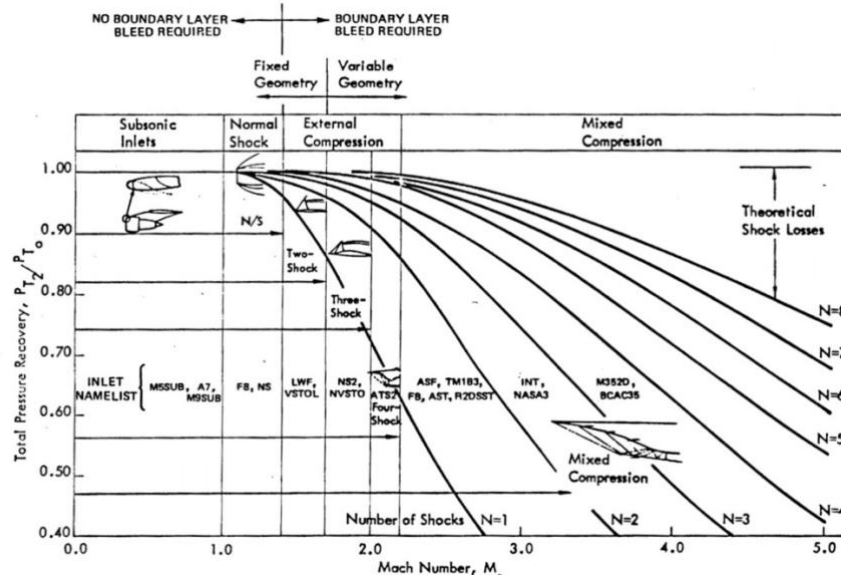


Figure 13. Inlet recovery verses Mach Number for different inlet compression types. [20]

4.2 Inlet Design

A basic 3 oblique shock, 1 normal shock, mixed compression inlet with appropriate notation is shown in Figure 14.

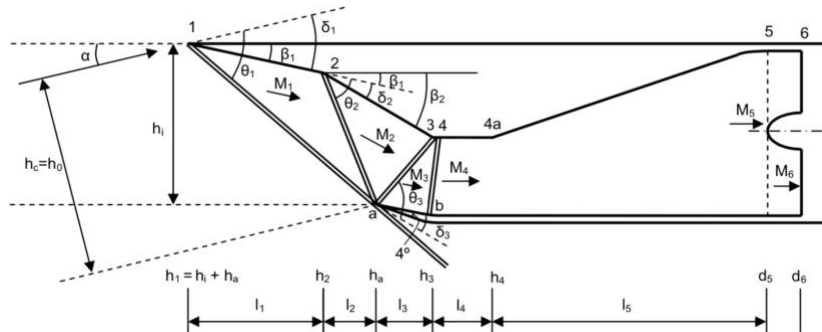


Figure 14. Two dimensional 3+1 shock Mixed Compression inlet [21]

Using a process laid out by Ran, the design point angles may be found using oblique shock properties, shown in Equation 2 and Equation 3. [21] In multi shock systems, the highest pressure ratio is achieved when the normal component of the oblique shocks are all equal as shown in Equation 4. A MATLAB program is written to calculate shock angles and deflection angles based on these equations for a 3 oblique shock + 1 normal shock system. The pressure ratio across each shock can then be calculated using Equation 5.

$$M_n^2 = \frac{(\gamma + 1)^2 M_{n-1}^4 \sin^2 \theta_n - 4(M_{n-1}^2 \sin^2 \theta_n - 1)(\gamma M_{n-1}^2 \sin^2 \theta_n + 1)}{[2M_{n-1}^2 \sin^2 \theta_n - (\gamma - 1)][(\gamma - 1)M_{n-1}^2 \sin^2 \theta_n + 2]} \quad (2)$$

$$\tan \delta_n = \frac{2 \cot \theta_1 (M_{n-1}^2 \sin^2 \theta_n - 1)}{2 + M_{n-1}^2 (\gamma + 1 - 2 \sin^2 \theta_n)} \quad (3)$$

$$M_1 \sin^2 \theta_1 = M_2 \sin^2 \theta_2 = \dots = M_n \sin^2 \theta_n \quad (4)$$

$$PR_n = \left[\frac{(\gamma + 1) M_{n-1}^2 \sin^2 \theta_n}{(\gamma - 1) M_{n-1}^2 \sin^2 \theta_n + 2} \right]^{\frac{\gamma}{\gamma - 1}} \left[\frac{(\gamma + 1)}{2 \gamma M_{n-1}^2 \sin^2 \theta_n - (\gamma - 1)} \right]^{\frac{1}{\gamma - 1}} \quad (5)$$

If the inlet mass flow is known at the design point, these angles and deflection angles may be used to calculate the supersonic inlet dimensions. The 3 oblique shocks are set to intersect at the cowl lip while the normal shock is set to intersect at the other end of the 3rd oblique shock.

To design the subsonic diffuser, fan mass flow and fan inlet Mach number are needed. Fourteen degrees is chosen as the subsonic diffuser angle to reduce diffuser length while ensuring the boundary layer stays attached. Using Equation 6 and the data from a Mach 2.1, 2D NASA PIPSI inlet, the subsonic diffuser pressure ratio may be calculated [20]. The variable ϵ represents the pressure loss coefficient and is taken as 0.12 from the PIPSI data.

$$PR_{\text{diffuser}} = 1.0 - \epsilon \left[1 - \frac{1}{(1 + 0.2M^2)^{3.5}} \right] \quad (6)$$

The inlet design point is set at the cycle design point of Mach 2.1, 40,000 feet and optimized for maximum pressure recovery by varying the final throat Mach number using the MATLAB program. Table XI shows the design choices made for the inlet.

Table XI. Inlet Entrance Conditions and Design Choices.

Parameter	Value
MN_0	2.1
T_s (R)	389.97
P_s (psi)	2.72
γ	1.395
Inlet \dot{W} (lbm/s)	704.29
Fan Inlet Diameter (in)	49.2
MN_{4_up}	1.25
Diffuser angle	10°
Pressure loss coefficient, ϵ	0.12

Figure 15 shows a 2D drawing of the inlet and Table XII shows a table of the dimensions, design point Mach numbers and design point overall inlet pressure recovery with station numbers marked as they were in Figure 14.

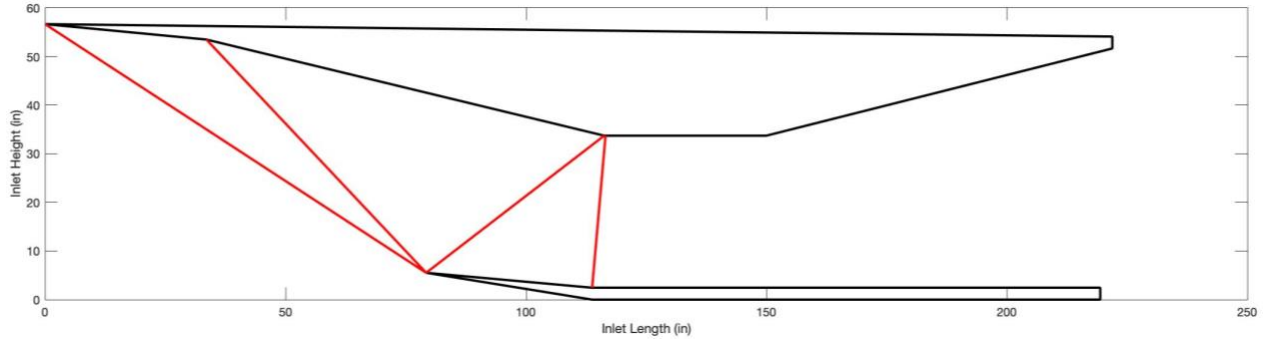


Figure 15. YJ-2030 2D Drawing of Inlet at Mach 2.1

Table XII. YJ-2030 Inlet Dimensions, Ramp Angles and station Mach Numbers at design point

l1 (in)	l2 (in)	l3 (in)	l4 (in)	l5 (in)
33.8	45.9	37.2	33.8	71.5
h1 (in)	h2 (in)	h3 (in)	ha (in)	h4 (in)
57.0	53.8	33.8	5.6	33.8
B1 (degrees)	B2 (degrees)	B3 (degrees)	Inlet Width (in)	Inlet Height (in)
5.4	13.5	5.1	49.2	57.0
MN @ 1	MN @ 2	MN @ 3	MN @ 4	Overall PR
1.92	1.57	1.25	0.81	0.9365

Figure 16 shows an inlet ramp angle schedule for supersonic flight. This schedule was calculated by optimizing for the highest pressure recovery. This ramp schedule is not perfect and should be corroborated by a CFD model or wind tunnel testing.

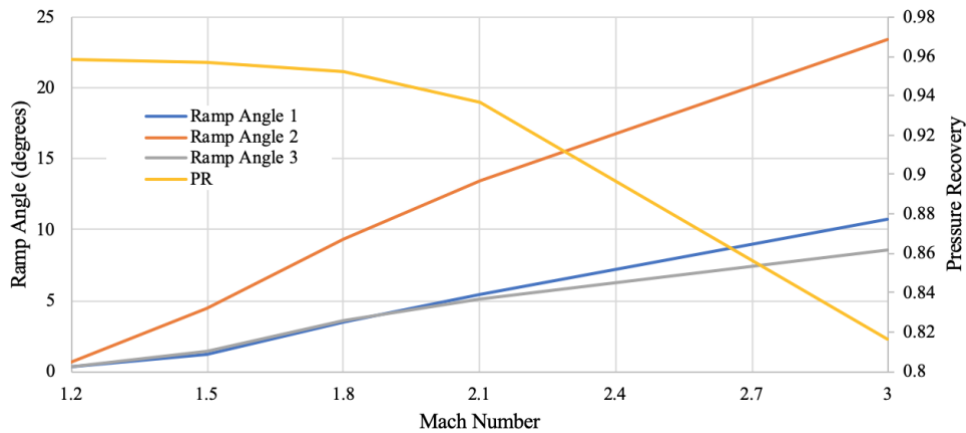


Figure 16. Inlet ramp angle schedule and pressure recovery verses Mach Number

Finally, to complete the supersonic inlet design, bypass, bleed and takeoff doors should be considered. Since this inlet operates at a wide range of MNs, bleed and bypass doors will be needed to extract the boundary layer and better match the inlet to the fan air demand, respectively. When the airflow is slowed down through a series of shocks a thick boundary layer will build, which can disrupt the fan and cause stall. Therefore, it will be bleed off using a

porous ramp. A bypass door downstream of the terminal shock will be used to better match the inlet mass flow rate to the fan air mass demand [15]. Finally, at takeoff speeds, the engine demands a large amount of mass flow. Typically the inlet is unable to fully provide this mass flow, therefore, takeoff doors will be added to the inlet to provide the extra mass flow [22]. These doors will be opened and closed based on a pressure differences and will close when the aircraft is at sufficient speed.

4.3 Inlet Off Design Performance

Mixed compression supersonic inlets require bypass and bleed offtakes during operation depending on the throttle setting and flight speed. Also, during low throttle settings a significant amount of air will be spilled around the inlet. These offtakes and aerodynamic effects will cause installed drags on the engine. These drags are not typically bookkept by the airframer and must be instead accounted for in the installed performance of the engine. These drags are difficult to calculate for newly designed inlets without the use of complex CFD and wind tunnel testing, therefore, NASA Inlet performance PIPSI maps will be used to measure the performance of the engine across the mission envelope.

The “R2DSST” inlet performance maps are chosen because the R2DSST inlet most closely matches the designed inlet parameters; Both inlets are 2D mixed compression inlets and designed for Mach 2.0+. A process laid out by Kowalski is used in conjunction with the NPSS solver in order to converge the inlet flow parameters [20]. The process had to be modified when calculating the off design pressure recovery due to convergence errors in the NPSS model; A simple Mach number versus pressure recovery relationship was used instead of the more complex A_o/A_c versus $eRam$ relationship. The inlet maps used in this model are shown in Appendix C.

Inlet drags are summarized for the 3 different cruise portions of the mission in Table XIII, The effect from the drags is quite significant; at some conditions the inlet drag was well over 5% of the overall net thrust supplied by the engine. No bypass extraction occurs at Mach 2.1 since this is the design point. Additionally, no bypass extraction occurs at the Mach 1.15 and Mach 0.98 mission points by virtue of the inlet maps. Any conditions faster than Mach 1.3 would have bypass extracted from the inlet.

Table XIII. Inlet Performance at different Mission Stages.

Mission stage	A_o/A_c	Drag due to inlet (lbf)	eRam	Bypass (lb_m/s)	Bleed (lb_m/s)
Overland Cruise (40k, 1.15 MN)	0.5241	620.39	0.9802	0	9.3
Oversea Cruise (40k, 2.1 MN)	0.8575	887.82	0.9313	0	46.05
Overland Cruise (50k, .98 MN)	0.4987	463.67	0.9839	0	5.07

Another important piece of the inlet off design performance is the buzz and distortion of the inlet. During off design, the throat terminal shock may not lie inside the throat of the inlet. This can cause interactions between the subcritical shock and the boundary layer and can block the inlet causing a large drop in the pressure recovery. This will cause the shock to travel towards the cowl lip and the process repeats at a rapid rate. An example of Buzz is shown in Figure 17.

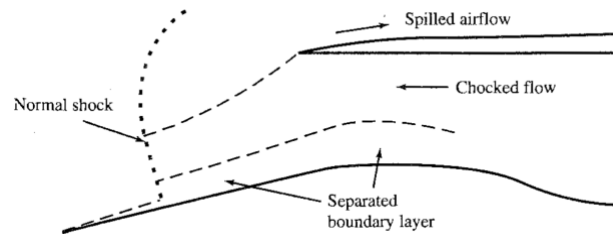


Figure 17. Conditions leading to Buzz [22]

Distortion is a phenomenon where the fan face receives a nonuniform pressure and flow distribution at the fan face. Distortion as well as buzz may severely lower thrust and cause the compressor to stall; Therefore, buzz and distortion must be prevented.

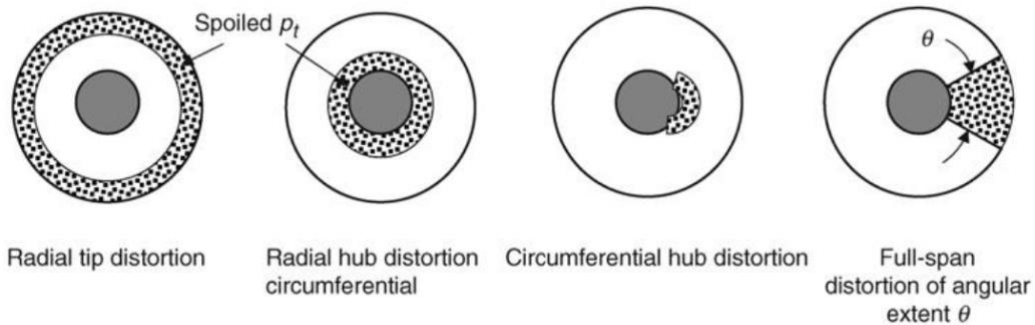


Figure 18. Inlet Distortion [15]

Figure 19 shows the engine demand area over inlet capture area ratio versus MN. This is plotted against the distortion and buzz limits of the R2DSST inlet. Shown by the red ellipse, the inlet transients into the buzz limit around Mach 1.8. Mach 1.8 also is the R2DSST inlet starting Mach number. This condition must be revisited during inlet CFD analysis to ensure the inlet will not unstart and enter buzz.

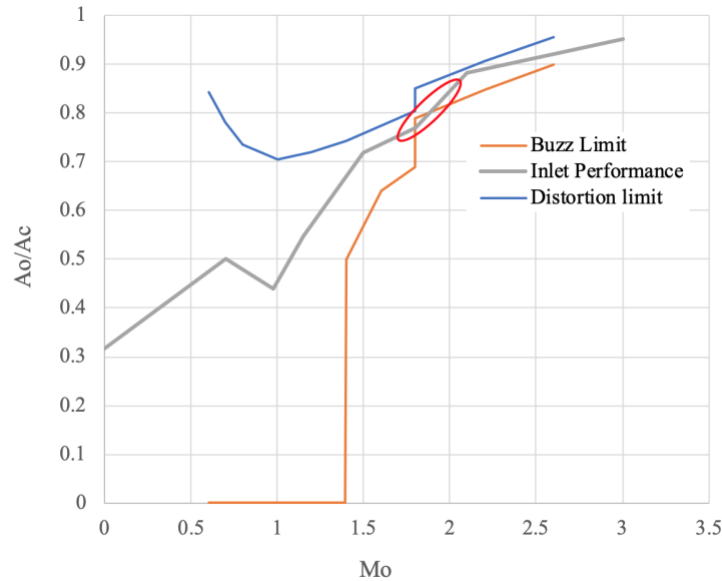


Figure 19. Inlet Buzz-Distortion Performance

4.4 Materials and Manufacturing

The inlet experiences temperatures up to 1100 °R during Mach 3.0 operation at 50,000 feet. Traditional composite materials that could be used to manufacture the inlet would degrade at these temperatures. High temperature polyimide composites have been used in jet engines as nozzle flaps. Current state of the art polyimide composites such as AVIMID® N, have a service temperature of around 1200 °R. Its material properties are shown in Appendix D. The team recommends that the YJ-2030 inlet be build using the AVIMID® N composite material. Rather than manufacturing the inlet as a single part or multiple large parts, the composite material could be manufactured as thick composite sheets and then screwed together into the desired shape. This would allow for quicker and easier maintenance of the inlet.

5. Compressors

The YJ-2030 includes a 3 stage fan and 6 stage high pressure compressor. The purpose of a jet engine compressor is to mechanically compress the air to the specified design requirements using a system that is safe, efficient and lightweight. This section will outline the general compressor design approach, followed by a discussion of the design results. Finally, compressor materials and manufacturing methods will be discussed.

5.1 Design Approach

The general approach for compressor design begins by determining the efficiency, pressure ratio and corrected mass flow requirements from the cycle design and compressor map. On a compressor map, component

design point is typically at a corrected speed of 100% and an R-line of 2 on the map. Therefore, to find the component design requirements, the compressor map is scaled using the map scalars from the cycle model and the pressure ratio, corrected mass flow and efficiency are read off the map at the component design point. Next, a design point condition is chosen so that the inlet conditions to the compressor may be found.

Once conditions and requirements are set, design may begin. The team utilized Turbomachinery prEliminary Design (TED), a team generated MATLAB script, to carry out the compressor design. TED performs a mean-line compressor design by assuming a constant axial velocity across the machine. Besides the inlet conditions, additional inputs include: first stage rotor relative MN, hub to tip ratio, inlet guide vane exit angle and loss coefficients. Traditionally, loss coefficients would be a fall out from the other design choices, but since the efficiency was already selected based on technology trends, the loss coefficients will be varied to match the compressor efficiency from the map. Stage inputs include: exit stator flow angle, deHaller number, diffusion factor on the rotor and stator, taper ratio, and chordwise Reynolds number on the rotor and stator. Special attention was paid to ensure that the selected first stage rotor relative MN would not yield a shaft speed that would violate the AN₂ rule for the turbines.

General turbomachinery equations outlined by Fähradi and Mattingly were used to create TED [15] [22]. The following labeling and sign convection was used for the compressor design:

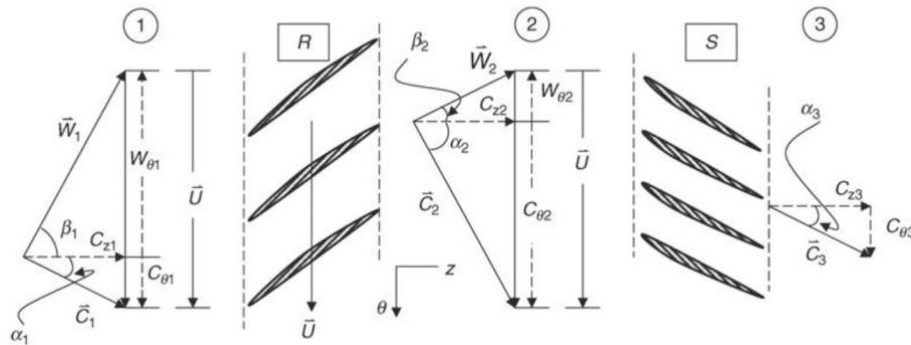


Figure 20. Compressor Coordinate System [15].

As Figure 20 shows, the exit stator or inlet guide vane flow angle is used as the incoming absolute flow angle to the following rotor. This allows all flow angles in the compressor to be generated from just DeHaller number choices and exit stator/IGV angle choices. Flow angles across the blade height, including at the hub and tip, may be found by assuming free vortex flow.

Inputs are varied and stages are added one by one until a design that meets both the compressor requirements and the general compressor parameter guidelines is found. A figure showing general guidelines on compressor parameters is shown in Figure 21. TED was also coded to output the compressor parameters, generate velocity triangles at the mean-line, hub and tip and create a component flow path outline.

Parameter	Range of values	Typical value
Flow coefficient ϕ	$0.3 \leq \phi \leq 0.9$	0.6
D-Factor	$D \leq 0.6$	0.45
Axial Mach number M_z	$0.3 \leq M_z \leq 0.6$	0.55
Tip Tangential Mach Number, M_T	1.0–1.5	1.3
Degree of reaction	$0.1 \leq R \leq 0.90$	0.5 (for $M < 1$)
Reynolds number based on chord	$300,000 \leq Re_c$	>500,000
Tip relative Mach number (1st Rotor)	$(M_{1r})_{tip} \leq 1.7$	1.3–1.5
Stage average solidity	$1.0 \leq \sigma \leq 2.0$	1.4
Stage average aspect ratio	$1.0 \leq AR \leq 4.0$	<2.0
Polytropic efficiency	$0.85 \leq e_c \leq 0.92$	0.90
Hub rotational speed	$\omega r_h \leq 380$ m/s	300 m/s
Tip rotational speed	$\omega r_t \sim 450$ – 550 m/s	500 m/s
Loading coefficient	$0.2 \leq \psi \leq 0.5$	0.35
DCA blade (range)	$0.8 \leq M \leq 1.2$	Same
NACA-65 series (range)	$M \leq 0.8$	Same
De Haller criterion	$W_2/W_1 \geq 0.72$	0.75
Blade leading-edge radius	$r_{L.E.} \sim 5$ – 10% of t_{max}	5% t_{max}
Compressor pressure ratio per spool	$\pi_c < 20$	up to 20
Axial gap between blade rows	$0.23 c_z$ to $0.25 c_z$	$0.25 c_z$
Aspect ratio, fan	~ 2 – 5	<1.5
Aspect ratio, compressor	~ 1 – 4	~ 2
Taper ratio	~ 0.8 – 1.0	0.8

Figure 21. Guidelines on the Range of Compressor Parameters [15].

5.2 Fan

The YJ-2030 features a transonic 3 stage fan that produces a pressure ratio of 4.44 at design point. To start fan design, the requirements of the fan are set. For the YJ-2030, at the top of climb cycle design point, the starting point on the unscaled map is a corrected fan speed of 91% and R-line of 2. The fan map is scaled and at the component design point, the PR requirement is 4.44, the adiabatic efficiency requirement is 0.914 and corrected mass flow requirement is 531 lbm/s. This PR requirement is much different than the PR requirement of 3.33 at design point, highlighting the fact that sometimes the compressor does not share its design point with the cycle design point.

Because the fan diameter was considered a constraint during cycle design, a fan hub-tip ratio and a fan entrance MN was chosen at design point. This allowed the team to determine the fan diameter during cycle design. However, these choices must be respected during component design. The team must use the hub-tip ratio and the fan entrance area determined by the cycle.

Sea level static is chosen as the fan design condition which sets the uncorrected mass flow. Since the fan entrance area and hub to tip ratio were already chosen during cycle design, inlet MN is determined using the ideal

compressible gas flow continuity equation and inlet conditions. Table XIV summarizes the design conditions and requirements for the fan.

Table XIV. Fan Inlet Conditions and Requirements.

Parameter	Value
Total Temperature (°R)	518.67
Total Pressure (psi)	14.696
Average Heat Capacity Ratio	1.4
Mach Number	0.67
Mass Flow Requirement (lbm/s)	531.83
Pressure ratio Requirement	4.44
Efficiency Requirement (%)	91.4
Fan Area (in ²)	1729.3
Hub/tip ratio	0.3

The design Mach Number for the fan is quite high, however due to the fan diameter requirement, this must be accommodated. A variable inlet guide vane was included on the multistage fan as part of the front frame to deal with the high fan inlet Mach number and to help match the fan better during off design performance. Many supersonic MFTFs, such as the GE Affinity and the GE F110, also include VIGV [23].

5.2.1 Fan Design Results

A 3 stage fan is designed with a 1st stage rotor tip Mach number of 1.416. This yields a low spool design rpm of 6913. The 1st stage rotor tip Mach number is within the suggested values from Farokhi but is quite high. It could be lowered if the stage count was increased but this is deemed undesirable since an additional fan stage can easily add 500 to 1000 pounds of engine weight. A table summarizing overall Fan compressor results is shown in Table XV.

Table XV. Fan Design Results Summary.

Parameter	Value
Number of Stages	3
1 st Stage Rotor Tip MN	1.416
Shaft Speed (rpm)	6913
Pressure Ratio	4.44
Adiabatic Efficiency	91.4%

The detailed stage parameters can be seen in Table XVI on the following page. These values are well within the recommended ranges. Velocity triangles at the hub, mean-line and tip of each stage can be seen in Appendix E.

Blade angles and MNs are shown in Table XVII. Blade angles are calculated from the flow angles by assuming a 2° incidence and using Carters rule for deviation. For initial design, the stagger of the blades are estimated using the cascade profiles for the stators and the double circular arc estimation for the rotors.

Table XVI. Fan Compressor Design Parameter Results.

	IGV	Stage 1		Stage 2		Stage 3	
		Rotor	Stator	Rotor	Stator	Rotor	Stator
Diffusion Factor	N/A	0.43	0.42	0.43	0.42	0.43	0.42
De Haller #	N/A	0.72		0.72		0.72	
Stage PR	0.988	1.671		1.664		1.616	
Loading Coefficient	N/A	0.439		0.402		0.385	
Flow Coefficient	N/A	0.653		0.581		0.544	
Hub to Tip ratio	0.3	0.300		0.613		0.757	
Mean Radius (in)	18.157	18.157	20.032	20.398	21.651	21.816	22.604
Number of blades	26	20	23	30	47	42	47
Solidity	1.04	1.29	1.19	1.21	1.20	1.18	1.28
AR	3.65	2.29	1.63	1.80	1.29	1.53	1.10
Taper Ratio	1	0.8	1	0.8	1	0.8	1
Tip Speed (ft/s)	N/A	1483.8		1483.8		1483.8	
Stagger Angle (°)	2	-67.7	16	-69.5	16	-70.5	16
Blade Chord (in)	4.721	7.515	6.558	5.295	5.026	3.888	3.889
Degree of Reaction	N/A	0.758		0.789		0.798	

Table XVII. Fan Compressor Design Blade Angles and Mach Numbers.

	IGV	Stage 1		Stage 2		Stage 3	
		Rotor	Stator	Rotor	Stator	Rotor	Stator
Blade angle in (deg)	0.00	-54.24	33.27	-57.58	33.36	-59.25	33.99
Blade angle out (deg)	2.24	-35.32	-8.59	-41.69	-8.58	-44.73	-9.63
MN abs in	0.670		0.769		0.706		0.658
MN abs out	0.671		0.616		0.567		0.524
MN relative in		1.206		1.216		1.178	
MN relative out		0.813		0.819		0.797	

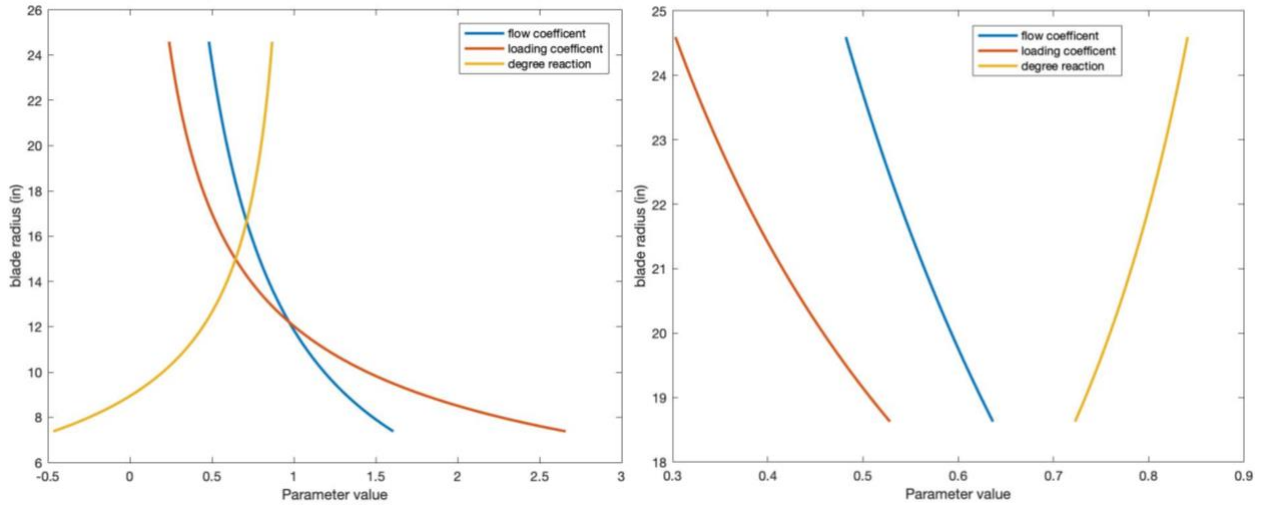


Figure 22. Aerodynamic parameters as a function of blade radius for the 1st (left) and last fan stage (right).

From Figure 22, it can be seen that the free vortex flow design assumption does not work well for the first stage. At the hub of the tall first stage blade, the reaction is negative and the flow coefficient and loading coefficient flow fall out of their actable ranges. This phenomenon, along with lower blade speeds at the hub is why large single stage fans are stratified, with the hub producing a lower pressure rise. During detailed fan design later on, this lower pressure rise must be accounted for in the following stages.

On the other hand, free vortex flow design assumption works very well for the last stage of the fan. The reaction stays above 0.5 near the hub and the flow and loading coefficients stay within their recommended ranges.

The final flow path of the Fan compressor is shown below in Figure 23. It should be noted that the YJ-2030 fan diameter meets the strict 49.2'' fan diameter constraint outlined by the RFP.

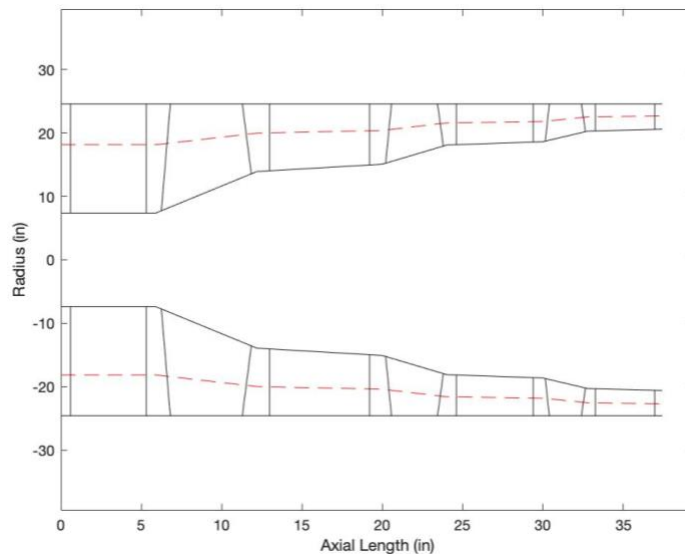


Figure 23. Fan Flow path drawing.

5.2.2 Fan Blade Design

Blade design for the fan must be considered. As can be seen from Table XVII above, the relative MN that the rotors see is supersonic while the absolute MN that the stators see is subsonic. Thus a different blade shape will be required for the stators and the rotors. Furthermore, as we travel across the blade height, the magnitude of the MN increases. This means that the hub may require an airfoil that is subsonic while the blade tip may require a supersonic airfoil.

The rotors on all 3 stages of the fan will require controlled diffusion airfoils or custom airfoils to prevent large shock losses and efficiency drops. Near the tip of the rotors, the blades may become quite thin, which may cause issues during manufacturing.

The stators may be designed with NACA 65-series airfoils at the hub and mean-line since the absolute MN is below 0.78. The tip of the stators may require double circular arc airfoils (DCA). For simplicity, the YJ-2030 shall manufacture its stators with a constant DCA shape across the blade height.

Finally, the twist of the first and last stage fan rotor blades is analyzed. As can be seen from Figure 24, the first stage flow turning is very high at the hub and the turning varies significantly from the hub to the tip. This further confirms that a free vortex flow assumption is not possible for the first stage of the fan. On the other hand, the last stage rotor sees a fairly constant flow turning between 10-20 degrees across the blade height. This should not present any issues during manufacturing.

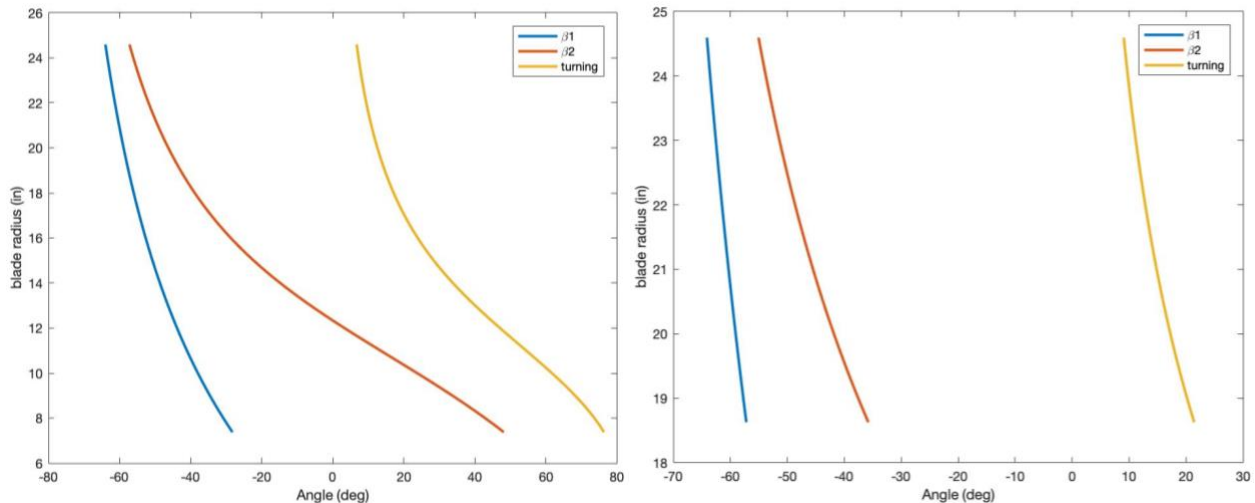


Figure 24. Twist of the 1st and last stage fan rotor blades as a function of blade radius.

5.2.3 Fan Off Design Performance

Just as important as the design of the compressor is its performance over the flight envelope. The YJ-2030 cycle design uses Energy Efficient Engine (EEE) turbomachinery maps. The uncorrected map starting point is a corrected fan speed of 91% and R-line of 2. This point was chosen for power management purposes. As MN increases, T_2 will increase as well. Since the flight envelope is so large, this has a dramatic effect on the corrected fan speed, N_{1c} , and thus N_1 . So that the engine can meet performance requirements at supersonic climb conditions such as Mach 1.5 and Mach 1.8, the design point corrected fan speed and must be lowered. This is why the fan was designed to have a much higher FPR, 4.4, than was needed at design point, 3.35. This concept is outlined by Kurzke and Halliwell [24].

During design point calculations, NPSS scales the performance maps based on the cycle parameters chosen. Then, in off design mode, the turbomachinery is matched based on power requirements and flow continuity. A scaled fan compressor map is shown below in Figure 25. The corrected fan speed values needed to be scaled as well, which is why these values seem irregular at first glance. The mission operating line is overlaid on the map to show that a positive stall margin is maintained throughout the flight envelope. Because the taxi and Mach 3 operating points travel outside of the fan limits, the performance is extrapolated. These points should be rigorously tested to confirm the performance at these points.

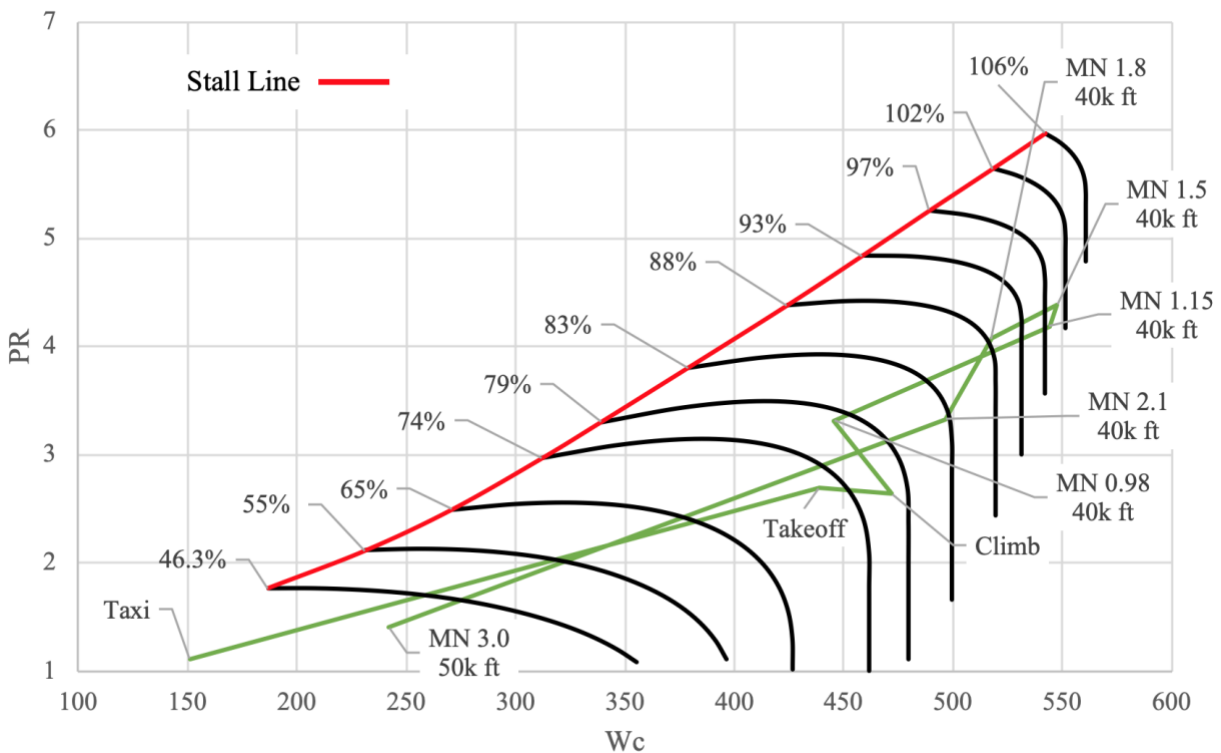


Figure 25. Scaled Fan Compressor Map for the YJ-2030 with the Mission Operating line overlaid.

5.3 High Pressure Compressor

The YJ-2030 features a highly efficient, 6 stage HPC with a pressure ratio of 8.5. Just like the fan, HPC design conditions and requirements must be found. For the YJ-2030, at top of climb design point, the HPC corrected speed is set to 100% while the R-line is set to 2. Therefore, the component design point and the cycle design point are the same. Thus, the pressure ratio requirement is 8.5, the corrected mass flow requirement is 98.30 lbm/s and the adiabatic efficiency requirement is approximately 90.9%. For simplicity, the design conditions for the HPC will be those at cycle design point. These conditions set the uncorrected mass flow requirement for the compressor. Unlike the fan, entrance area, entrance MN, and hub-tip ratio are now design choices since no core size requirement is present. Table XVIII summarizes the design conditions and requirements.

Table XVIII. HPC Design Conditions and Requirements.

Parameter	Value
Static Temperature (°R)	1020.29
Static Pressure (psi)	68.75
Average Heat Capacity Ratio	1.35
Mass Flow Requirement (lbm/s)	76.025
Pressure ratio Requirement	8.5
Efficiency Requirement (%)	90.9

Additionally, a variable inlet guide vane, is included on the HPC to allow for better off design matching and easier start up. The first 3 rows of stators are also designed to be variable stators to help with these issues. By changing their angle during operation, they may change the incidence angle of the oncoming flow, increasing efficiency.

5.3.1 HPC Design Results

A 6 stage HPC is designed with a 1st stage rotor tip Mach number of 1.14. This yields a high pressure spool design rpm of 14485. The 1st stage rotor tip Mach number is on the lower end of the recommended values to limit the HPT AN₂. Additionally, by choosing a lower 1st stage rotor tip Mach number, the HPC efficiency could be higher and the engine program risk lower. A table summarizing overall Fan compressor results is shown in Table XIX.

Table XIX. HPC Design Results Summary.

Parameter	Value
Number of Stages	6
First stage Rotor Tip MN	1.14
RPM	14485
PR	8.50
Adiabatic Efficiency	90.89%

The stage parameters can be seen in Table XX on Page 31. These values are within the recommended ranges from Farokhi. Velocity triangles at the hub, mean line and tip of each HPC stage can be seen in Appendix F. Blade angles and MNs are shown in Table XXI.

From Figure 26, it can be seen that the free vortex flow assumption works well for the first stage HPC. The ranges of the flow and loading coefficients are acceptable across the blade height. Furthermore, near the hub, the reaction is satisfactory, greater than 0.5. At the last stage, the aerodynamic coefficients barely change across the blade height because the blade height is relatively small.

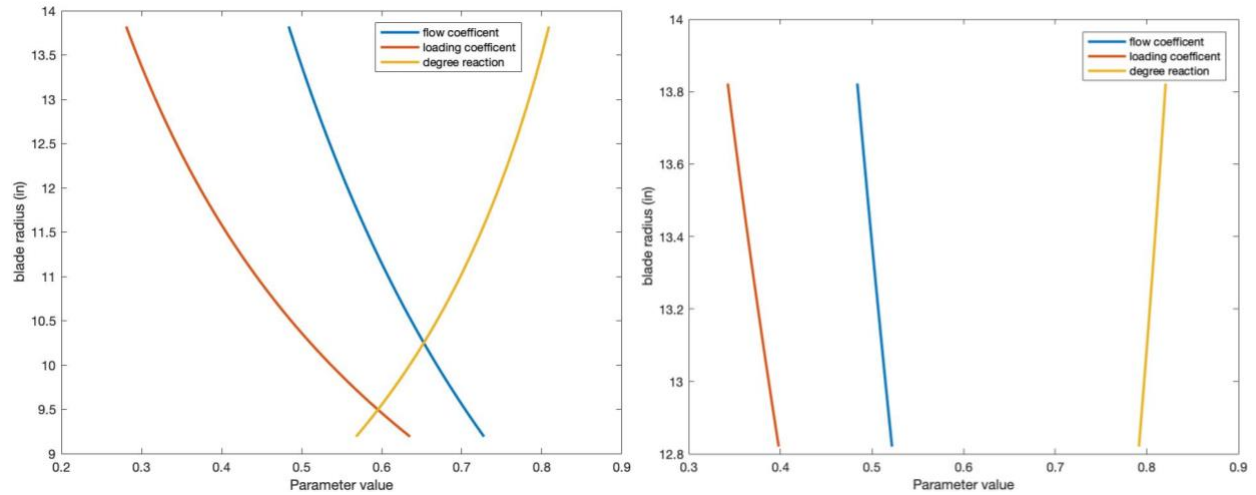


Figure 26. Aerodynamic parameters as a function of blade radius for the 1st (left) and last HPC stage (right).

The final flow path of the HPC compressor is shown below in Figure 27. The max tip radius of the HPC, 14 inches, gives more than enough room for the bypass duct to surround the core.

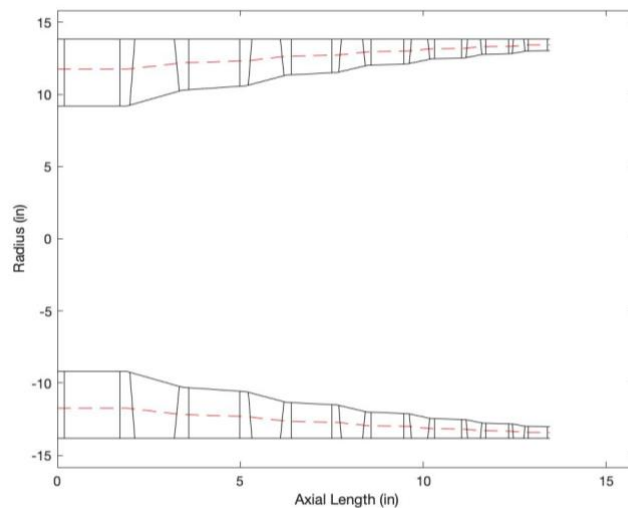


Figure 27. HPC Flow Path Drawing.

Table XX. HPC Design Parameter Results,

	IGV	Stage 1		Stage 2		Stage 3		Stage 4		Stage 5		Stage 6	
		Rotor	Stator	Rotor	Stator	Rotor	Stator	Rotor	Stator	Rotor	Stator	Rotor	Stator
Diffusion Factor	N/A	0.425	0.430	0.425	0.430	0.425	0.430	0.425	0.430	0.425	0.430	0.425	0.430
De Haller #	N/A	0.720		0.720		0.720		0.720		0.720		0.720	
Stage PR	0.990	1.508		1.481		1.449		1.415		1.384		1.355	
Loading Coeff	N/A	0.390		0.378		0.372		0.369		0.369		0.368	
Flow Coeff	N/A	0.570		0.543		0.526		0.515		0.507		0.502	
h/t	0.665	0.665		0.766		0.833		0.877		0.906		0.928	
Mean Radius (in)	11.738	11.738	12.185	12.315	12.639	12.720	12.945	12.998	13.156	13.192	13.307	13.331	13.415
# blades	55	48	66	64	112	84	112	107	143	135	167	166	199
Solidity	1.13	1.23	1.28	1.20	1.31	1.18	1.32	1.16	1.36	1.15	1.31	1.14	1.31
AR	3.03	2.40	2.34	2.21	2.08	2.05	1.88	1.92	1.73	1.82	1.59	1.73	1.49
Taper Ratio	1	0.8	1	0.8	1	0.8	1	0.8	1	0.8	1	0.8	1
Tip Speed	N/A	1747.2		1747.2		1747.2		1747.2		1747.2		1747.2	
Stagger Angle	7	-68.8	12	-69.8	13	-70.4	14	-70.9	15	-71.4	16	-71.67	16
Blade Chord	1.528	1.932	1.506	1.459	1.198	1.127	0.966	0.888	0.791	0.709	0.660	0.579	0.555
Reaction	N/A	0.735		0.754		0.768		0.780		0.798		0.807	

Table XXI. HPC Design Blade Angles and Mach Numbers.

	IGV	Stage 1		Stage 2		Stage 3		Stage 4		Stage 5		Stage 6	
		Rotor	Stator	Rotor	Stator	Rotor	Stator	Rotor	Stator	Rotor	Stator	Rotor	Stator
Blade angle in	0.00	-56.50	36.89	-58.05	36.71	-59.13	36.48	-59.90	36.19	-60.69	35.31	-61.15	34.92
Blade angle out	7.78	-39.68	-2.75	-42.56	-3.88	-44.52	-5.03	-45.90	-7.31	-47.30	-8.57	-48.09	-9.76
MN abs in	0.550		0.676		0.636		0.600		0.568		0.535		0.509
MN abs out	0.554		0.521		0.491		0.465		0.442		0.421		0.403
MN relative in		1.053		1.038		1.014		0.985		0.962		0.933	
MN relative out		0.725		0.716		0.700		0.682		0.667		0.648	

5.3.2 HPC Blade Design

Blade design for the HPC must be considered. As can be seen from Table XXI, the relative MN that the rotors see is transonic while the absolute MN that the stators see is subsonic. Similar to the fan, a different blade shape will be required across the blade height.

The rotors on all 6 stages of the HPC will require DCA airfoils to prevent large shock losses and efficiency drops. The stators may be designed with NACA 65-series airfoils across the entire blade height since the absolute MN is below 0.78 at the tip.

Finally, we can study the blade twist. As can be seen from Figure 28, the first stage flow turning is limited to about 30 degrees at the hub and 15 degrees at the tip. The last stage rotors have almost no twist in them and are about 1 inch in height. This shouldn't result in any boundary layer or tip clearance issues on the last stage.

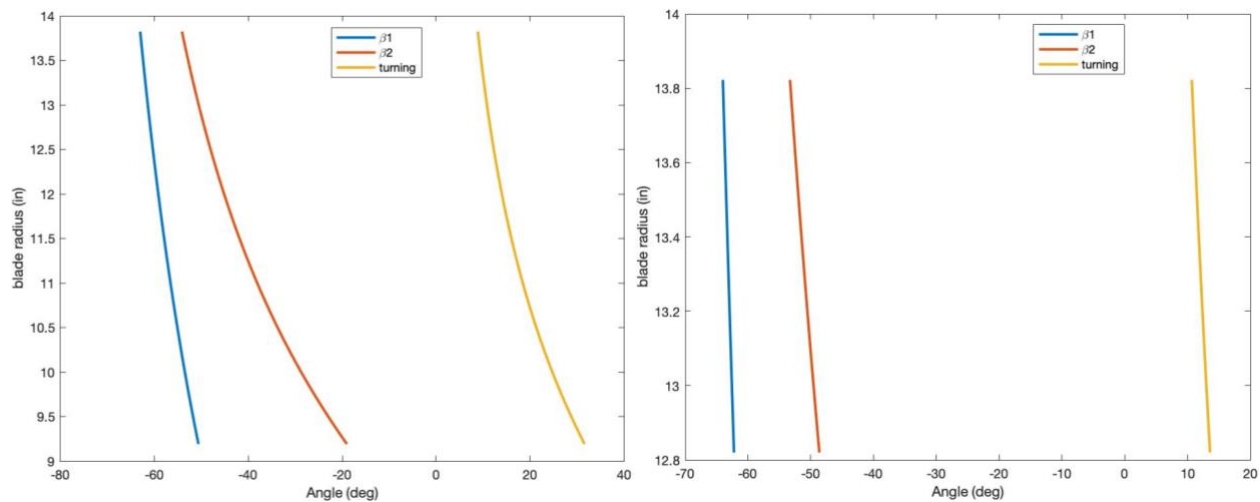


Figure 28. Twist of the 1st and last stage HPC rotor blades as a function of blade radius.

5.3.3 High Pressure Compressor Off Design Performance

At cycle design point, the HPC operates at uncorrected map starting point of 100% corrected speed and an R-line of 2. Unlike the fan, the HPC actually shares a cycle design point with the component design point. For the HPC, the EEE HPC compressor map is used in the cycle design. This map is scaled according to map scalars listed at the cycle design point and is shown in Figure 29, with the mission operating line overlaid. All mission points have the stall margin of at least 10%.

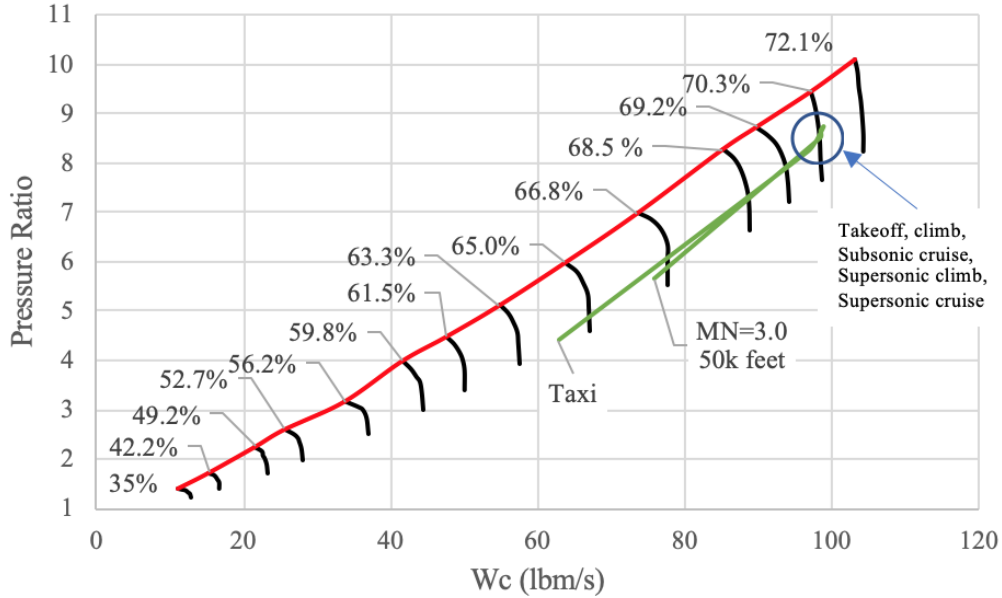


Figure 29. Scaled HPC Map for the YJ-2030 with the Mission Operating line overlaid.

5.4 Materials and Manufacturing

The dominant stresses that occur in the compressors are the centrifugal stresses in the rotors and their disks. Secondary stresses in the compressors include bending, vibrational and thermal stresses. Equation 7, was used to determine the required specific strength for the blades based the centrifugal stresses in the blades.

$$\frac{\sigma_c}{\rho_{blade}} = \frac{\omega^2 A}{4\pi} (1 + TR) \quad (7)$$

Results of the compressor stress analysis, as well as the estimated maximum operating temperature for each rotor blade is shown in Table XXII.

Table XXII. Compressor Stress Analysis.

	Fan			HPC					
	Stage 1	Stage 2	Stage 3	Stage 1	Stage 2	Stage 3	Stage 4	Stage 5	Stage 6
Required material strength/density ratio (ksi/(slug/ft³))	7.11	4.42	2.96	5.50	4.00	2.94	2.21	1.70	1.33
AN2 rule (in²*rpm x10¹⁰)	8.26	5.67	3.87	7.11	5.23	3.87	2.91	2.24	1.75
T_{max} (°R)	1139	1167	1195	1320	1444	1569	1693	1818	1942

In conjunction with calculating the stresses in the blades, a literature review on fan and compressor materials and manufacturing techniques was done. Many modern high bypass SFTFs utilize carbon-fiber fan blades [25]. However, if implemented on the YJ-2030, the epoxy used to manufacture the carbon-fiber fan blades would degrade

at the Mach 3.0 temperatures. Therefore, an alternative high temperature composite was researched. PMR Polyimide/Graphite fiber composites have been investigated for use on fan blades by NASA in the 1970's with varying degrees of success [26]. Modern polyimide composites, such AVIMID® N, have a service temperature of around 1200 °R and material properties that more than suffice for use as a fan blade. The material properties are shown in Appendix D. If this technology is deemed not mature by 2030, the alternative would be manufacturing the 3 stage fan as titanium blisks. Newest derivatives of the F110, a similarly sized engine to the YJ-2030, feature a 3 stage blisk (bladed disk) design [27]. This manufacturing path will reduce the number of components in the fan, simplifying manufacturing, but would probably increase the engine weight.

State of the art HPCs typically feature designs with the first 4-5 stages manufactured as titanium blisks. Later stages are manufactured with a separate disk and nickel blades inserts. Because of the high temperatures at Mach 3.0 in the YJ-2030, only the first 3 stages may be manufactured from Ti-834, a high temperature titanium alloy. The material properties for Ti-834 alloy are shown in Appendix D.

The latter 3 stages in the HPC of the YJ-2030 feature compressor blisks that are manufactured from Ti48Al2Cr2Nb, a Titanium-Aluminum alloy. Titanium-aluminum alloys are considered to be replacements to nickel super alloys; They offer similar strength properties to nickel alloys but are significantly less dense. Material properties are shown in Appendix D. The latter 3 stage blisks will be unable to be manufactured using traditional methods like multi axis CNC machining due to the small blade height. Instead, they will be 3-D printed out of Ti48Al2Cr2Nb powder in circular sectors and electron beam welded (EBW). The blisk must be printed in separate parts because current metal 3D printing machines are unable to print such a large part. Research has shown that this method is feasible, potentially more economical than traditional machining, and produces a part with comparable strength and fatigue life to the status quo [28].

The stators of each stage will be made out of the material used in the rotor and will be manufactured using traditional methods where the stators are manufactured as “sectors” and slid into the casing. An example of stator sectors are shown in Figure 30.

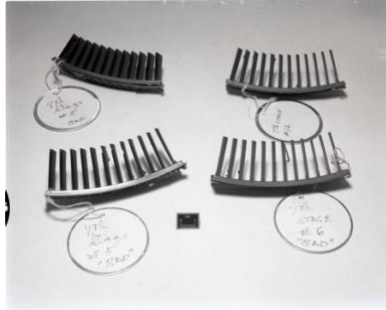


Figure 30. Stator Sectors for a J-85 engine [29].

Manufacturing the HPC rotors as blisks reduces weight by as much as 20-30%, improves efficiency and reduces the number of parts in the HPC system, simplifying final assembly and maintenance. A comparison of a traditional blade locking pin design and a compressor blisk is shown in Figure 31.

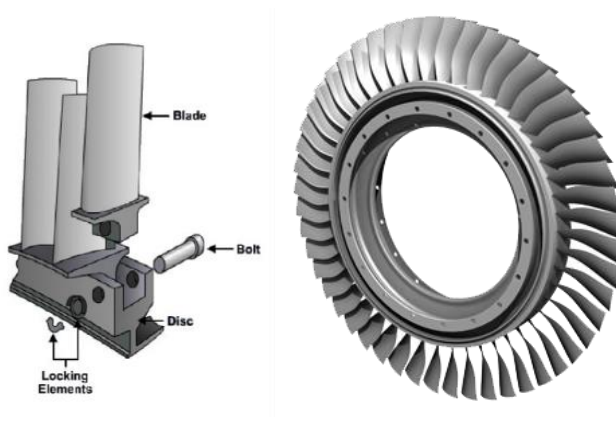


Figure 31. Comparison of traditional blade locking mechanism versus a Blisk [28] [30]

Finally, a table summarizing the rotor material and manufacturing technique for the compressors is shown in Table XXIII.

Table XXIII. Compressor Material and Manufacturing summary.

	Fan			HPC					
	Stage 1	Stage 2	Stage 3	Stage 1	Stage 2	Stage 3	Stage 4	Stage 5	Stage 6
Material	AVIMID® N			Ti-834			Ti48Al2Cr2Nb		
Manufacturing technique	Composite layup & Autoclave			CNC Blisks			3D Printed Blisks		
Alternative Manufacturing technique	CNC Titanium Blisks			N/A-Technology is already mature			Traditional lock and pin blades		

6. Combustor

The YJ-2030 features a next generation annular, lean-premixed combustor. The combustor is modeled after the GE TAPS II combustor. The purpose of a jet engine combustor is to mix the fuel and air and then ignite the mixture.

6.1 Combustor Architecture

To determine the combustor architecture for the YJ-2030, a literature review on combustor design goals and combustor architectures was conducted. Then, a Pugh Matrix is created to determine the architecture.

For civil jet engine combustors, high combustion stability, high combustion efficiency, low total pressure loss, low NOx emissions and high lifetime are design goals. Modern, technologically mature combustor architectures are: the rich-quench-lean (RQL) combustor, dual annular combustor (DAC) and the Twin Annular Premixing Swirler (TAPS) combustor. The RQL combustor functions by burning fuel rich in the primary zone to improve flame stability and lower NOx before quickly quenching with the dilution air. The DAC functions by combusting the fuel in two staged combustion zones using twin nozzle fuel injectors. Finally, the TAPS combustor architecture functions by premixing the fuel-air mixture and then staging the combustion similar to the DAC [31]. The Pugh matrix evaluating the combustor architectures using the design goals listed above is shown in Table XXIV.

Table XXIV. Combustor Architecture Pugh Matrix

Combustor Architecture	Stability	Combustion Efficiency	NOx Emissions	Pressure Loss	Linear Life	Total
RQL	3	3	1	2	2	11
DAC	2	3	2	2	2	11
TAPS	2	3	3	2	3	13

From the results, it is evident that the TAPS configuration is best suited for the YJ-2030.

6.2 Combustor Design

6.2.1 Diffuser Design

The entrance flow conditions at the cycle design point and combustor requirements are shown in Table XXV.

Table XXV. Combustor Inlet Conditions and Requirements.

Parameter	Value
\dot{W} (lbm/s)	345.61
P_{t3} (psi)	646.366
T_{t3} (°R)	1915.37
T_{t4} (°R)	3366
MN_3	0.403
Inlet Radius (in)	13.43
Combustor Cycle Design PR	0.96
Exit Radius (in)	12

The exit MN coming from the compressor is 0.403; this must be slowed down using a diffuser, otherwise the combustor will be long and experience a high hot pressure loss. The YJ-2030 combustor uses a dump diffuser design with a pre-diffuser to lower the pressure loss across the diffuser. The flow slows by 40% in the pre diffuser, prior to entering the dump diffuser. This significantly lowers the pressure loss that occurs across the dump diffuser. The pressure loss across the pre-diffuser is small and is assumed to be 0. The PR across the dump diffuser is calculated using relationships outlined by Barclay [15]. Diffuser design results are included in Table XXVI.

Table XXVI. Diffuser Design Results.

	Pre diffuser	Dump Diffuser
Entrance Area (in²)	66.81	121.46
Entrance MN	0.41	0.23
Tip (in)	13.82	13.91
Hub (in)	13.03	12.44
Mean (in)	13.43	13.17
Exit Area	121.46	226.97
Exit MN	0.23	0.12
Length (in)	1.84	1.89
Pre diffuser angle (°)	10.00	
Total Length (in)	3.73	
PR across Diffuser	0.97	

6.2.2 Main Combustor Design

Traditional combustors divert most of the air around the snout to be injected through primary, secondary or cooling holes. The differentiating factor in a TAPS combustor design is that 70% of the inlet air goes through the snout of the combustor while the remaining 30% is used for cooling the liner [32]. Twenty percent of the snout flow is reserved for dome cooling. Additionally, the air-liquid ratio (ARL) in the fuel injector is assumed to be 3.14. This allows for a high penetration and spray area [33]. The air distribution in the YJ-2030 combustor is shown in Table XXVII.

Table XXVII. Airflow Distribution in the YJ-2030 Combustor.

\dot{W}_3 (lbm/s)	\dot{W}_{fuel} (lbm/s)	Total		Snout		
		\dot{W}_{snout} (lbm/s)	$\dot{W}_{liner\ cooling}$ (lbm/s)	$\dot{W}_{swirler}$ (lbm/s)	$\dot{W}_{dome\ cooling}$ (lbm/s)	$\dot{W}_{fuel\ injector}$ (lbm/s)
345.61	8.85	241.93	103.68	171.31	42.83	27.79

The design procedure for sizing the YJ-2030 combustor begins by determining the combustor snout and dome heights based of a reference MN choice, the mass flow distribution and the exit conditions from the diffuser. Because the snout requires higher mass flow, this results in a snout and dome height that is much larger than traditional

combustors. The reference MN choice is iterated to produce a low pressure loss and ensure the reference velocity is between 50-100 ft/s.

In traditional combustors, the liner length may be estimated as three times the dome height [22]. Because the TAPS combustor configuration requires no dilution air, the length of the liner and thus the overall combustor may be reduced [31]. Two times dome length is a reasonable choice that still yields a residence time of at least 2ms.

The YJ-2030 will feature 2 fuel ignitors, installed on opposite ends of the combustor. The ignitor plugs shall be annular gap igniter plugs. These plugs protrude into the liner in order to create a better spark. A diagram of a annular gap igniter plug is shown in Figure 32.

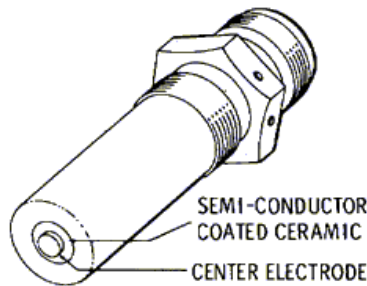


Figure 32. Diagram of a annular gap igniter plug [34].

Combustor geometry and the YJ-2030 combustor flowpath sketch are shown in Table XXVIII and Figure 33 respectively.

Table XXVIII. YJ-2030 Main Combustor Design Information.

Parameter	Value	Parameter	Value
Entrance Casing Tip (in)	14.65	Casing Exit Tip (in)	12.65
Entrance Casing Hub (in)	11.30	Casing Exit Hub (in)	11.35
Entrance Casing Area (in ²)	272.69	Casing Exit Area (in ²)	98.55
Snout Area (in ²)	190.88	Dome Height (in)	2.34
Snout Tip (in)	14.15	Dome Length (in)	1.13
Snout Hub (in)	11.81	Liner Length (in)	4.92
Number of Domes	26	Pressure Loss Across Liner	0.993
Number of Ignitors	2	Total Combustor Length (in)	8.83

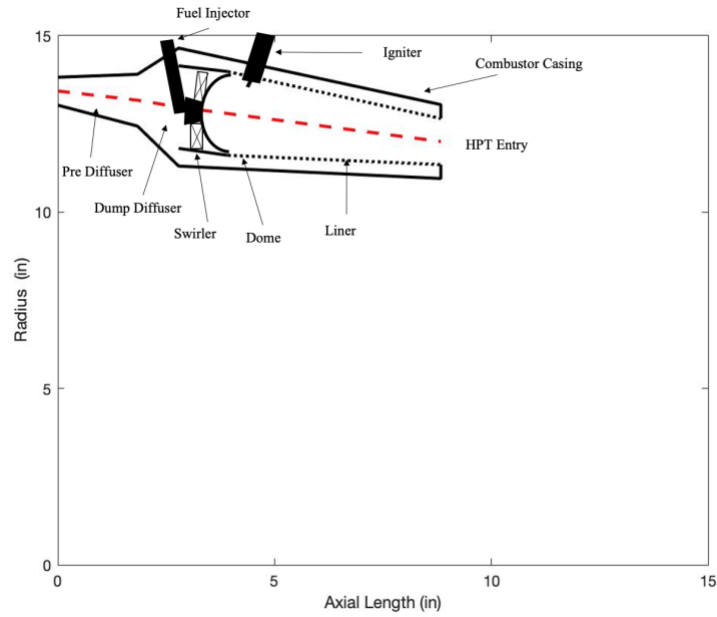


Figure 33. YJ-2030 Combustor Flow path.

Once combustor geometry is set, the combustor swirlers may be designed. The swirlers in a TAPS combustor can be broken into two categories: cyclonic swirlers and pilot swirlers. As seen in Figure 34, there are two cyclonic swirlers in each dome which swirl approximately 80% of the flow. The remaining 20% of air is swirled by pilot swirlers. In the diagram below, two swirlers surround the pilot fuel injector. For YJ-2030 design, it is assumed the inner swirler is part of the fuel injector system.

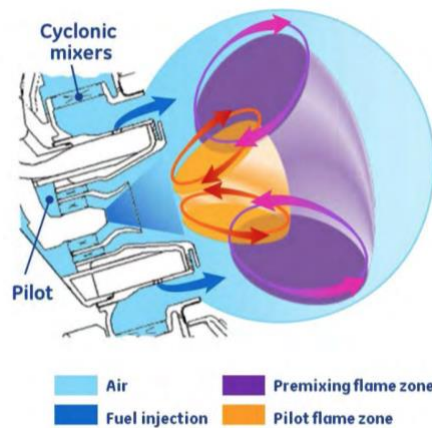


Figure 34. TAPS II Dome Configuration [32].

A process outlined by Li is adapted for the TAPS swirlers [35]. An axial flat-vaned swirler is chosen for use in both the cyclonic and pilot swirlers because of its simplicity and low cost. During swirler design, a high swirl

number, $0.8 < S_n < 1.0$, is preferred to ensure that healthy recirculation zone is produced. Results for the swirler design are shown in Table XXIX.

Table XXIX. YJ-2030 Combustor Swirler Design

	Cyclonic Swirler	Pilot Swirler
Number of swirlers per Dome	2	1
$\dot{W}_{swirler}$ (lbm/s)	1.20	0.60
Vane Angle (°)	50	60
Number Vanes	8	8
Thickness of vanes (in)	0.04	0.04
Swirler Coefficient	1.3	1.3
Diameter Fuel Injector (in)	0.00	0.47
Diameter Swirler (in)	2.03	1.64
Swirl number	0.79	1.03

Finally, the fuel injectors for the combustor are chosen. A TAPS combustor contains a pitot injector and two main injectors. The pitot injector shall be a simplex fuel injector and the main injectors shall be air-blast atomizers. Simplex Injectors rely on a large pressure different between the fuel and air to atomize the droplets while the air-blast injectors rely on the shear from the air flow [36].

The combustor performance parameters are shown in Table XXX. The primary zone equivalence ratio for a TAPS combustor was estimated from the TAPS II Combustor final report [37].

Table XXX. Final Combustor Performance Parameters.

Combustor Pressure ratio	Residence time (s)	Patter Factor	T_{t, max} (°R)	Primary Zone Equivalence ratio (ϕ)	Reaction Rate parameter (b)	Combustor Loading Parameter (θ)
0.96	0.002	0.15	3584	0.623	350.535332	73 E+5

The combustor efficiency may be estimated as ~100% from a relationship derived by Henderson and Blazowski [15]. This matches the cycle combustion efficiency of 99.99%.

6.2.3 Combustor Liner Design

The combustor liner design is relatively simple for a TAPS combustor compared to other designs; No dilution holes are required. The main design focus of the liner is to ensure that the liner has a long lifetime and the combustor casing is protected from the heat. Per the TAPS design specifications, 20% cooling air is reserved for cooling the liner. Using Equation 8, the liner cooling method may be determined.

$$\Phi = \frac{T_{gas} - T_{metal}}{T_{gas} - T_{cooling}} \quad (8)$$

Estimating the target liner metal temperature as 2700 °R and overestimating the gas temperature as the maximum gas temperature derived from the Pattern Factor, 3584 °R, the cooling effectiveness parameter is 0.53. This represents a worst case scenario.

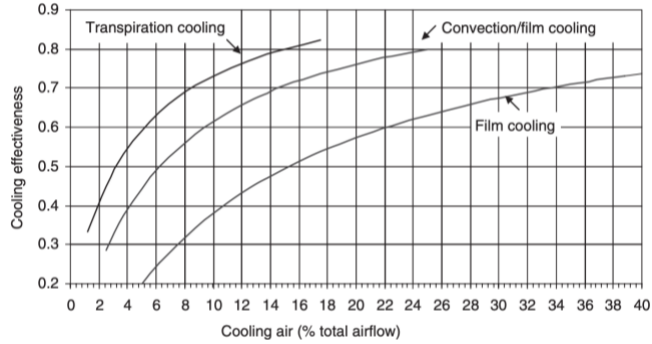


Figure 35. Cooling Air verses Cooling Effectiveness relationship [15]

At 20% cooling airflow, reading off Figure 35, worst case only film cooling is required for the YJ-2030 combustor liner. A potential film cooling method for the liner is shown in Figure 36.

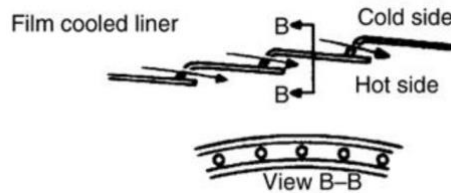


Figure 36. Film Cooling Method [15]

Another popular cooling method is called “effusion cooling” and differs from traditional film cooling in hole size and hole density. Traditional film cooling holes are larger and more spaced out compared to effusion holes. With complex manufacturing processes becoming more mainstream, complex effusion cooling hole patterns may be designed and easily manufactured. Effusion hole patterns are shown in Figure 37.



Figure 37. Combustor Liner with effusion hole surrounding the primary dilution holes [38]

This method is more effective at cooling the liner for the same amount of cooling flow than tradition film cooling. Therefore, the YJ-2030 will feature a combustor liner that utilizes effusion cooling.

6.3 Combustor Off Design Performance

Similar to the turbomachinery components, the combustor changes its performance as the engine operating conditions change. In the cycle model, combustor efficiency and combustor pressure loss remain the same throughout the flight envelope. In reality, this is not the case; After flight testing, the cycle model should be updated to include performance maps for combustor efficiency and combustor pressure ratio as a function of corrected flow.

Another important off design performance metric is the relight envelope of the combustor. If a blowout occurs in a combustor, for any reason, it is imperative for the relight to be quick and easy, otherwise safety may be at risk.

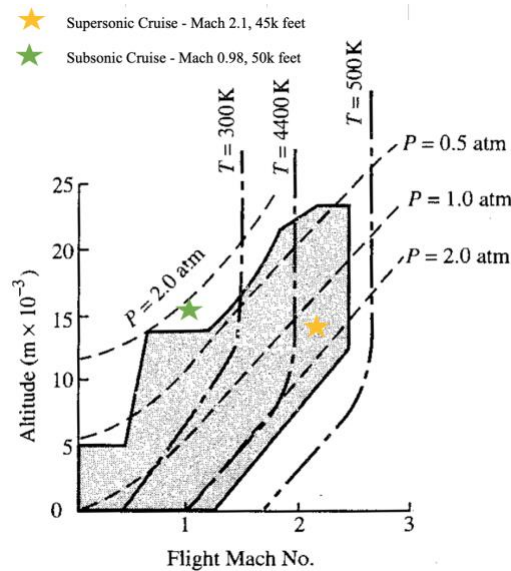


Figure 38. Typical Relight Envelope with YJ-2030 mission conditions overlaid [15].

As Figure 38 shows, at the supersonic cruise-climb point, the aircraft is safely within the relight envelope. At other flight conditions, such as high altitude subsonic cruise, the pilot may have to descent to a lower altitude in order to relight the combustor.

6.4 Combustor Emissions

As mentioned earlier in the requirements section, emissions are of great importance for civil certified jet engines. The YJ-2030 is evaluated on its NO_x emissions production using two metrics. Its supersonic cruise NO_x emissions index and the landing takeoff cycle NO_x emissions. It was difficult to find a NO_x Emission Index (EI) estimation for a TAPS configuration combustor. Instead, a NASA HSR NO_x EI relationship was modified. The equations used in the study were developed in 1995; Since then, there has been significant improvement in combustor

technology. Per Foust, the TAPS combustor reduced NOx emissions by almost 40% relative to a RQL combustor [32]. To obtain a conservative estimate for the YJ-2030 emissions, the NOx EI calculated from the HSR study was reduced only by 25%. During flight testing, a true NOx EI relationship may be developed. The equations used to calculate the NOx EI are shown below:

If $T_3 > 1100$ °R

$$EI = (0.01555T_3 - 8.3) * 0.75 \quad (9)$$

Else if $T_3 > 1100$ °R

$$EI = 0.75 * 2.899 \left(\frac{T_{3,max}}{1000} - .046 \right) \left(\frac{P_4}{P_{4,TOC}} \frac{T_{4,TOC}}{T_4} \frac{W_{31,TOC}}{W_{31}} \right) \exp(-72.28 + 2.087\sqrt{T_f} - 0.014611T_f) \quad (10)$$

Where

$$T_f = \max(3600, T_3 + 1.1765(T_4 - T_3)) \quad (11)$$

These equations are evaluated at the supersonic cruise point, the boomless cruise point and the high-subsonic cruise point to understand the cruise emissions performance.

Table XXXI. Cruise Emissions Performance for the YJ-2030

Flight Condition	EI (g/kg)
Supersonic Cruise @ Mach 2.1, Altitude 40k ft	4.83
Boomless Cruise @ Mach 1.15, Altitude 40k ft	5.08
High subsonic @ Mach 0.98, Altitude 50k ft	5.58

Table XXXI suggests that the 5 g/kg NOx EI goal, defined in the requirements section, is met at the supersonic cruise point. Although the other two cruise points do not meet the goal, the fuel flow at these points is much lower; thus the over weight of the NOx emissions will be lower.

Just as important as cruise emissions, are the emissions that occur within the vicinity of airports. ICAO defines these emissions as part of a Landing-Takeoff (LTO) cycle. This parameter is defined as the total weight of NOx per KN of thrust for a LTO cycle. The allowable NOx per kN per LTO cycle is a function of the SLS engine pressure ratio. The equation is shown in Equation 12.

$$\frac{D_p}{F_{oo}^*} = 36 + 2.42 * OPR_{oo} \quad (12)$$

For the YJ-2030, with a takeoff OPR of 21.84, the allowable NOx per kN per LTO cycle is 88.85 (g/kN). To calculate the NOx per kN, the engine cycle was run at the different LTO operating modes. Using the cycle outputs, the NOx EI was calculated using the equations above. Finally, using the TSFC at each operating mode and converting, the NOx per kN for each operating mode could be found. Results are shown below in Table XXXII.

Table XXXII. YJ-2030 LTO Emissions Performance.

LTO operating mode	Time (min)	% of SLS Thrust	Thrust (lbf)	Emissions Index (g/kg)	TSFC (lbm/(hr*lbf))	Oxides of nitrogen (g/kN)
Takeoff	1.2	100	21700	5.51	0.504	5.67
Climb	2	65	14105	5.80	0.484	9.53
Descent	1.2	15	3255	4.45	0.470	4.26
Approach	2.3	34	7378	5.76	0.419	9.43
Taxi	26	5.8	1258.6	3.73	0.754	124.22
					Total:	153.11

As the figure shows, the YJ-2030 would not achieve the YJ-2030 ICAO certification for NOx. This is a result of the extremely poor taxi performance. The YJ-2030 produces over 80% of its NOx emissions just at the taxi condition. This can be attributed to many things. First, the TSFC at taxi is extremely poor, if the taxi TSFC can be improved 5%, the LTO emissions decrease by ~4%. Also, the NOx EI equations used are extremely sensitive to changes in T₃ at low throttle settings; a 5% decrease in T₃ yields a 10% decrease in the LTO emissions. This further reiterates the need to test the YJ-2030 in order to determine the proper EI NOx relationships.

6.5 Materials And Manufacturing

When selecting the materials for the combustor, it is important to understand that even though the combustor is stationary, the combustor is a major structural component of the engine and undergoes a lot of stress. It is in fact a pressure vessel and experiences the highest gauge pressure in the engine.

The combustor casing will experience temperatures that similar to exit compressor discharge temperature. Thus, the combustor casing for the YJ-2030 shall be manufactured out of the same Ti-Al alloy used in the last 3 stages of the compressor. It will also be manufactured with a thermal coating barrier (TBC) such as yttria-stabilized zirconia (YSZ). Ceramic TBCs have a thermal conductivity almost 20 times lower than that of nickel alloys [36]. This allows a TBC part to experience a lower metal temperature compared to one with no coating.

The combustor liner shall be made out of CMCs. The CMC components may be manufactured using a process called Polymer infiltration and pyrolysis (PIP). This method infuses a liquid preceramic polymer into the fiber

perform. This process is simpler and relatively low cost compared to other CMC manufacturing methods such as CVD or melt infiltration [39].

7. Turbines

The YJ-2030 features two stage cooled HPT and a two stage LPT. The purpose of a gas turbine is to extract work from the incoming flow. These systems experience some of the highest temperature gases in the engine and are thus the most stressed components. Major turbine design considerations include weight, efficiency and lifetime.

7.1 Design Approach

Just as in the compressor, the general design approach begins by determining the turbine requirements and selecting the inlet conditions. In modern gas turbines, the first stage nozzle of every spool is choked. This means that, for the most part, turbines operate with a constant corrected mass flow throughout the flight envelope. Thus, the design requirements for a turbine are typically the corrected mass flow as well as a power extraction requirement. The max T4 cycle point is usually chosen as the component design point for the turbines so that cooling flows may be sized.

Once conditions and requirements are set, design may begin. As in the compressor, the team utilized Turbomachinery prEliminary Design (TED) to carry out the design. TED performed a mean-line, constant tip design by assuming a constant axial velocity across the turbine. Blade angles across the blade height are found by assuming free vortex flow. Besides inlet conditions, additional inputs include: exit nozzle MN, initial mean line radius, inlet flow angle, exit rotor MN and loss coefficients. While loss coefficients are typically a fall out based on MNs and flow angles, since efficiency was chosen during cycle design, the loss coefficients are varied until the desired efficiency is matched. Finally, the design point rpm for each spool was iterated with the compressor design. The iteration ensures that the turbine material limits are respected.

Stage inputs include: Zweifel loading coefficient, taper ratio and chordwise Reynolds number on the rotor and stator. The following labeling and sign convection was used for the turbine design:

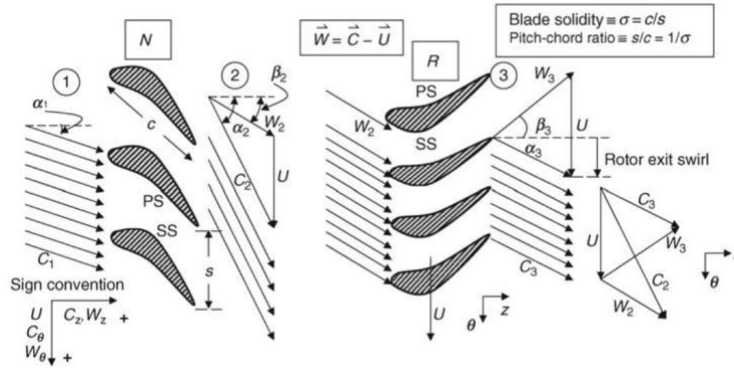


Figure 39. Turbine Labeling Convention [15].

Inputs are varied and stages are added one by one until a design that meets both the turbine design requirements and the general turbine parameter guidelines is found. A table showing general guidelines on turbine parameters is shown in **figure**. This information was compiled from sources such as Farohki, Mattingly, Denney and Sagerser [15] [22] [40] [41].

Table XXXIII. General Turbine Parameter Guidelines

	First stage	Following Stages
Exit Nozzle Mach Number	$M_2 \approx 1.1$	$M_2 < 0.9$
Exit Nozzle Flow angle	$\alpha_2 < 70^\circ$	$\alpha_2 > \sim 40^\circ$
Exit Rotor Mach Number	$M_{r3} < 0.9$	
Flow Coefficient	$0.5 < \phi < 1.1$	
Loading Coefficient	$0.8 < \psi < 2.3$	
Degree of Reaction	$0.2 < R < 0.7$ *at hub Reaction must be positive	
Zweifel Loading Coefficient	$0.8 < \xi < 1.0$	
AN ₂ (rpm*in ₂)	HPT: $AN_2 < 6.5 * 10^{10}$ LPT: $AN_2 < 7 * 10^{10}$	
Nozzle Axial Aspect Ratio	HPT: $1 < AR_x < 2$ LPT: $1 < AR_x < 3$	
Rotor Axial Aspect Ratio	HPT: $1.5 < AR_x < 3$ LPT: $3.5 < AR_x < 4.5$	

7.2 High Pressure Turbine

The YJ-2030 features a two stage high pressure turbine (HPT) design, with the first stage cooled using HPC bleed air. The design point required power for the turbine is 116108.3 horsepower at a corrected mass flow of 21.49 lbm/s. The cycle design point is chosen as the component design point for the HPT. Table XXXIV shows the inlet conditions and design requirements for the HPT.

Table XXXIV. HPT Inlet Conditions and Design Requirements.

Parameter	Value
Total Inlet Temperature (°R)	3366.00
Total Pressure (psi)	620.366
Average Heat Capacity Ratio	1.288
Mass Flow Requirement (lbm/s)	363.51
Efficiency Requirement (%)	95.6
Power Requirement (HP)	116108.3

7.2.1 HPT Design Results

The HPT features design with a first stage nozzle exit Mach number of 1.1, as recommended, at an angle of 65 degrees. The HPT turbine design choices and results are shown below in Table XXXV , Table XXXVI and Table XXXVII. The Velocity triangles are shown in Appendix G for the HPT at the hub, mean and tip.

Table XXXV. HPT Design Results Summary

Parameter	Value
Shaft speed (rpm)	14485
M ₂	1.05
α_2	65.00°
M _{r3}	0.88
α_4	42.00°
M _{r5}	0.78
α_6	0.11°

Table XXXVI. HPT Design Parameter Results

	Stage 1		Stage 2	
	Nozzle	Rotor	Nozzle	Rotor
Power Extracted (HP)	85535		30735	
Zweifel Coefficient	0.8	0.8	0.9	0.9
AN₂	4.07E+10		5.39E+10	
Stage PR	2.29		1.43	
Loading Coefficient	1.93		0.73	
Flow Coefficient	0.79		0.82	
Stage Reaction	0.26		0.63	
Hub-Tip ratio	0.90	0.83	0.79	0.76
Mean Radius (in)	12.00		11.37	
Number Blades	95	186	70	143
Solidity	1.40	2.37	1.53	2.53
Aspect Ratio	1.16	2.33	1.73	2.38
Taper Ratio	1	0.8	1	0.8
Tip Speed (ft/s)	1599.23		1608.41	
Stagger Angle	47.00	-18.41	16.97	-37.80
Blade Chord	1.12	0.93	1.57	1.26
Turbine Rotor Inlet Temp (°R)	3001.08		2733.61	

Table XXXVII. HPT Design Blade Angles and Mach Numbers

	Stage 1		Stage 2	
	Nozzle	Rotor	Nozzle	Rotor
Blade angle in (°)	-17.56	40.93	-35.86	-29.11
Blade angle out (°)	65.00	-62.37	46.76	-52.39
MN abs in	0.43		0.50	
MN abs out	1.10		0.65	
MN relative in		0.62		0.51
MN relative out		0.88		0.78

During initial design, the HPT was estimated to be 1.2 stages. Physically, this means that the HPT must be 2 stages. This resulted in an HPT design where the first stage produced approximately 70% of the work required which in turn designed a highly loaded, low reaction, first stage. The second stage HPT produced the remaining 30% of the work, but more importantly, it produced an exit flow with almost 0 swirl. This results in a low loading, high reaction stage. Having a highly loaded first stage provides additional benefits. The large temperature drop associated with a high loading coefficient allows the second stage HPT to be uncooled, since it will experience a lower rotor inlet temperature.

The free vortex flow assumption allows analysis across the entire blade height. In Figure 40, it is seen that the first stage maintains a positive reaction at the hub, as suggested, and varies to 0.4 at the tip. The loading coefficient remains below 2.5 at the hub.

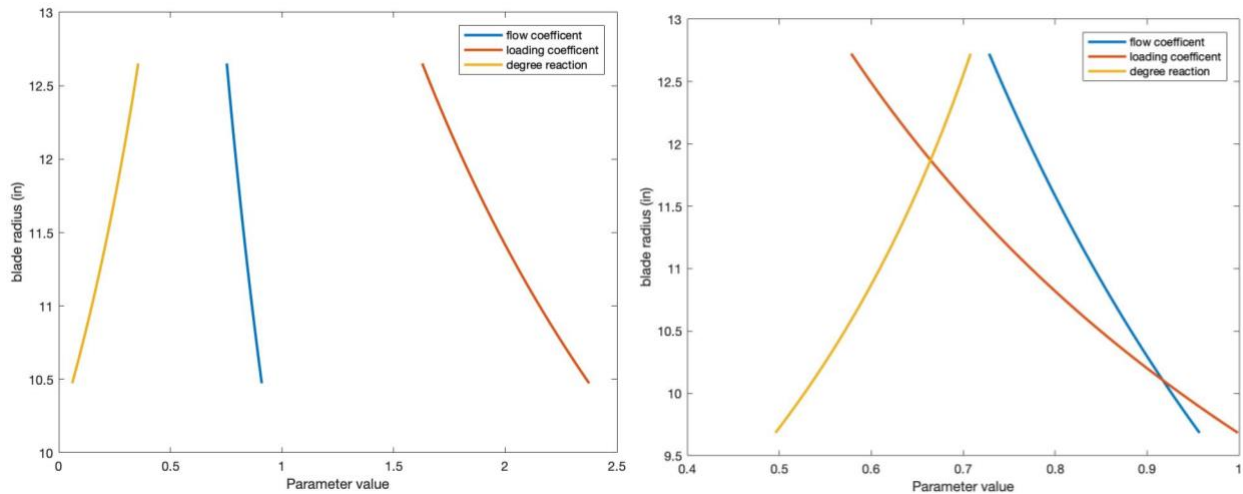


Figure 40. Aerodynamic parameters as a function of blade radius for the 1st (left) and 2nd HPT stage (right).

The aerodynamic coefficients are plotted on a general smith chart, shown in Figure 41. The first stage of the HPT is less efficient than the second stage, as expected, since the first stage does the majority of the work extraction. The second stage has a fairly low stage loading coefficient and could be improved by slightly lowering the first stage

exit nozzle MN. This would also improve the first stage reaction, however, the first stage nozzle would become more likely to unchoke during off design operation as first stage exit nozzle MN is lowered from MN 1.1.

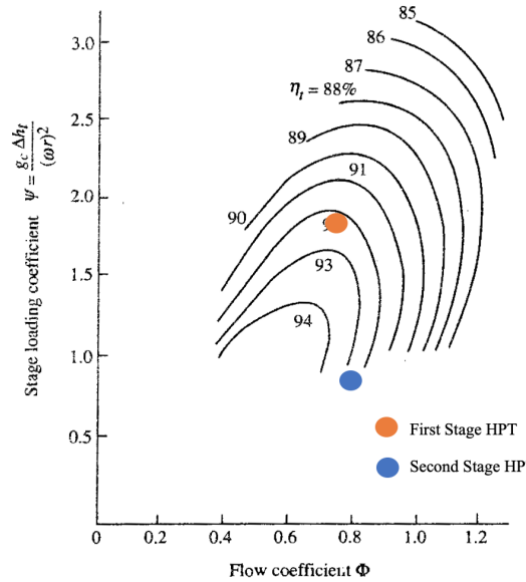


Figure 41. HPT Smith Chart [22].

The final flow path of the HPT turbine is shown in Figure 42. It is noteworthy to mention that the HPT turbine has an inlet mean radius 2 inches smaller than the HPC exit mean radius. Combustor geometry must adjust for this decrease in radius.

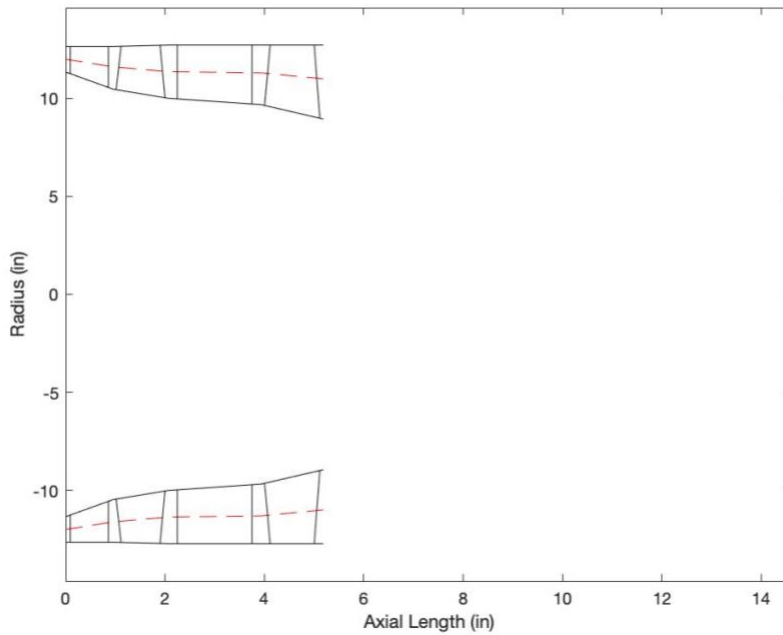


Figure 42. HPT Flow Path Drawing.

7.2.2 HPT Blade design

Turbine blade design is not as simple as compressor blade design where a certain family of blades may be chosen. The high turning in turbine blades and the supersonic first stage nozzle requires custom blades to be designed. The blade angles, seen in Table XXXVII are calculated by assuming the incidence is equal to the induced turning caused by the flow curvature at the leading edge and using Carters rule for deviation. Induced turning is calculated using Equation 13. Deviation in the supersonic nozzle is assumed to be 0°.

$$\Delta\theta_{ind} = 14 \left(1 - \frac{\beta_1}{70^\circ} \right) + 9(1.8 - \sigma) \quad (12)$$

Table XXXVII also shows that all blades following the first stage nozzle have subsonic blade relative Mach numbers. This is consistent with design recommendations and suggests that losses will be low.

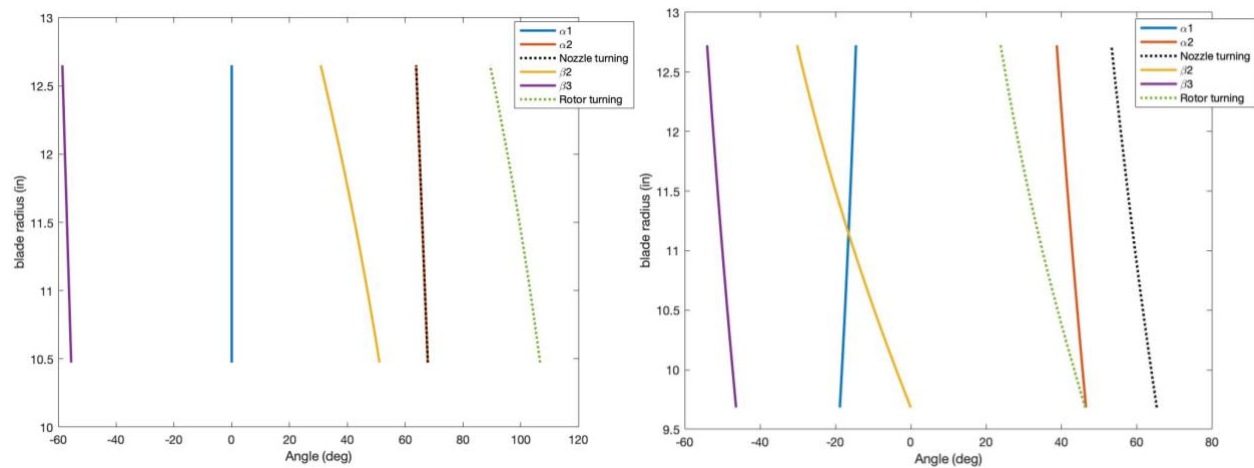


Figure 43. Twist of the 1st and last stage HPT nozzle and rotor blades as a function of blade radius.

As seen in Figure 43, the HPT blades have much high turning compared to the compressor blades; The first stage rotor turns the flow over 100° at the hub. The blades do have a small amount of twist as the blade height increases, however the twist from hub to tip is limited to no more than 25°. In the second stage, the turning for both the nozzle and the rotor is much less compared to the first stage, although the twist in the blades remains. This makes sense since a higher turning, suggests higher loading. Interestingly, the nozzle has higher turning than the rotor in the second stage. This is likely why the second stage reaction is greater than 0.5.

The first stage of the HPT is cooled using HPC bleed air. The amount of cooling flow was calculated by using the NPSS function CoolIt and setting a blade operating temperature of 3100 °R. Figure 44 shows the configuration of how the cooling flow will be distributed.

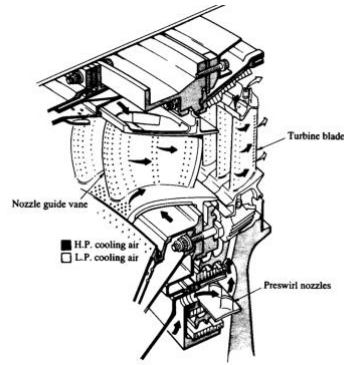


Figure 44. Cooling Scheme for a HPT Stage [42]

With advanced manufacturing techniques, such as metal 3D printing, the nozzle and rotor blades may be designed to have multiple hollow passages within them to cool convection the blade from the inside. Figure 45 shows an example of this.

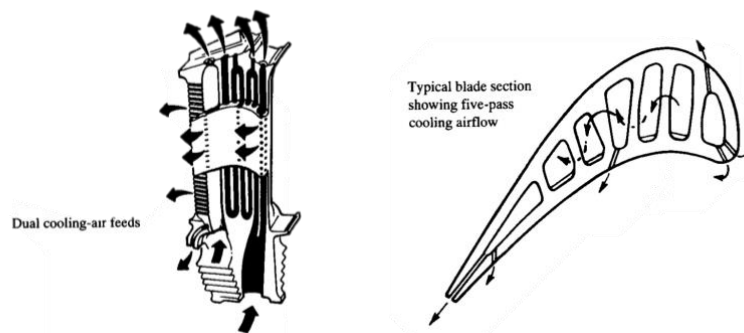


Figure 45. Five Pass Inner Blade Cooling [22]

7.2.3 HPT Off Design Performance

It is important to analyze the off design performance of the HPT. The EEE HPT turbine map used in the cycle design is scaled using the scaling values calculated in NPSS. Since the turbine operates choked, the speed lines will all collapse into a single line. Thus, to distinguish the speed lines easier, the corrected mass flow was multiplied by the corrected speed. As can be seen from Figure 46, the HPT operates for most of the mission points at 100% corrected speed. Unlike the HPC, at $MN=3.0$ and at taxi, the HPT actually operates at a higher corrected speed compared to the other mission points. To note, a higher corrected speed does not necessarily correlate to a higher uncorrected speed; The uncorrected HP taxi spool speed is 65%!

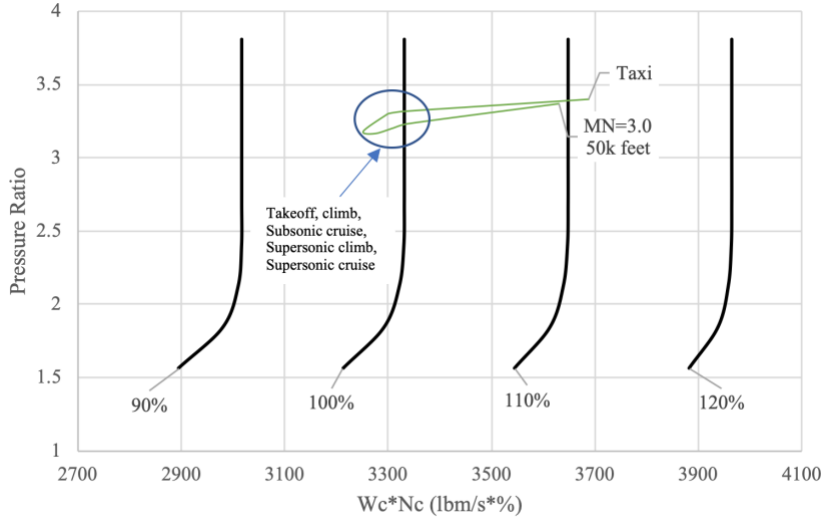


Figure 46. Scaled HPT Map for the YJ-2030 with the Mission Operating line overlaid.

7.3 Low Pressure Turbine

The YJ-2030 features a 2 stage uncooled Low Pressure Turbine (LPT). The design point required power for the turbine is 72844.5 horsepower at a corrected mass flow of 63.74 lbm/s. The LPT is limited by a max diameter of 21 inches so that it does not interfere with the bypass duct. The cycle design point is chosen as the component design point for the LPT. Table XXXVIII shows the inlet conditions and design requirements for the LPT.

Table XXXVIII. LPT Inlet Conditions and Design Requirements.

Parameter	Value
Total Inlet Temperature (°R)	2597.93
Total Pressure (psi)	188.928
Average Heat Capacity Ratio	1.300
Mass Flow Requirement (lbm/s)	366.20
Efficiency Requirement (%)	96.4
Power Requirement (HP)	72844.5

7.3.1 LPT Design Results

The low pressure turbine features design with a first stage nozzle exit Mach number of 1.05 at an angle of 60.5 degrees. A relatively low exit MN and angle for the first stage nozzle is required to ensure that the reaction is positive at the hub and so that first stage loading is not too high. This results in a high flow coefficient for the LPT. The second stage of the LPT required the balancing between the exit nozzle angle and the exit rotor relative MN to ensure that the work required was matched and the exit swirl was close to 0°. The second stage exit nozzle angle deviated by 2° from the recommended minimum recommended angle, 40°.

The LPT turbine design choices and results are shown below in Table XXXIX , Table XL and Table XLI.

The Velocity triangles are shown in Appendix H for the LPT at the hub, mean and tip.

Table XXXIX. LPT Design Results Summary

Parameter	Value
Shaft speed (rpm)	6913
M_2	1.05
α_2	60.50°
M_{r3}	0.83
α_4	38.00°
M_{r5}	0.74
α_6	1.2°

Table XL. LPT Design Parameter Results

	Stage1		Stage 2	
	Nozzle	rotor	Nozzle	Rotor
Power Extracted (HP)	53436		19897	
Zweifel Coefficient	0.8	0.8	0.8	0.8
AN₂	2.11E+10		2.62E+10	
Stage PR	1.90		1.31	
Loading Coefficient	2.08		0.80	
Flow Coefficient	1.03		1.05	
Stage Reaction	0.21		0.58	
Hub-Tip ratio	0.89	0.83	0.81	0.79
Mean Radius (in)	19.00		18.26	
Number Blades	85	248	114	204
Solidity	1.43	2.30	1.64	2.57
Aspect Ratio	1.09	3.13	2.33	2.92
Taper Ratio	1	0.7	1	0.7
Tip Speed (ft/s)	1212.33		1217.88	
Stagger Angle	41.47	-11.56	15.10	-28.85
Blade Chord	2.02	1.08	1.66	1.44
Turbine Rotor Inlet Temp (°R)	2375.89		2198.45	

Table XLI. LPT Design Blade Angles and Mach Numbers

	Stage 1		Stage 2	
	Nozzle	Rotor	Nozzle	Rotor
Blade angle in (°)	-17.33	36.86	-31.70	-18.71
Blade angle out (°)	60.50	-55.26	41.92	-44.57
MN abs in	0.49		0.54	
MN abs out	1.05		0.67	
MN relative in		0.66		0.54
MN relative out		0.83		0.74

We may analyze aerodynamic coefficients across the entire blade by assuming free vortex flow. In the first stage, Figure 47 shows that the reaction and loading coefficient at the hub are ~0 and 2.5, respectively. This is not

ideal, thus, the free vortex assumption must be revisited for the first stage of the LPT. Alternatively, during detailed design, further iterations between the cycle, the fan design and the LPT design, may solve this issue. The second stage aerodynamic coefficients remain within their recommended ranges.

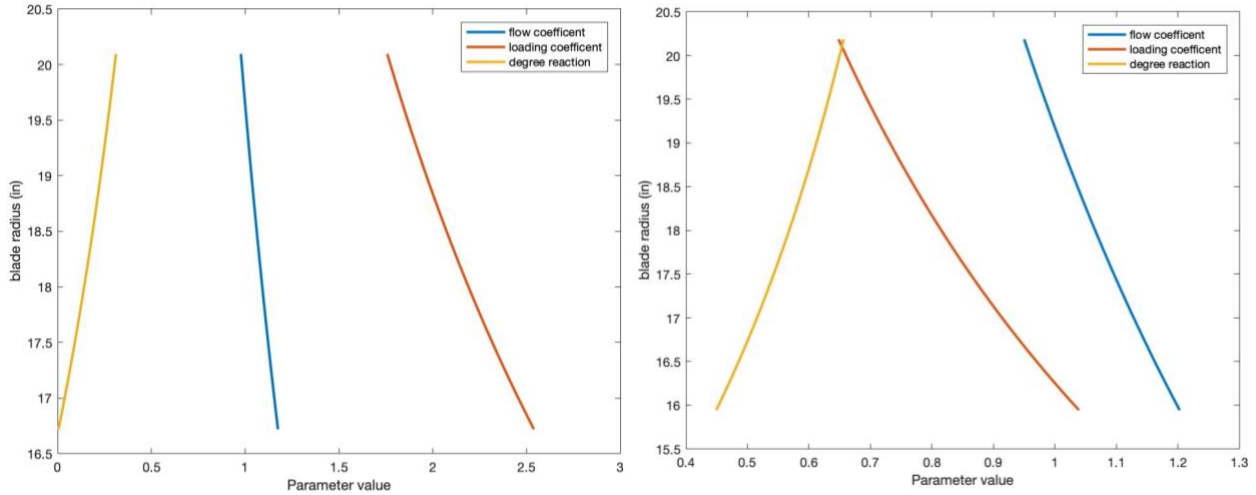


Figure 47. Aerodynamic parameters as a function of blade radius for the 1st (left) and 2nd LPT stage (right).

The aerodynamic coefficients are also plotted on a smith chart, shown in Figure 48, to estimate the efficiency of the LPT. Again, the first stage is less efficient compared to the second stage, just as in the HPT. From this figure, it is evident that the flow coefficient for the LPT is much too high and must be lowered to achieve the predicted cycle efficiency of 96%.

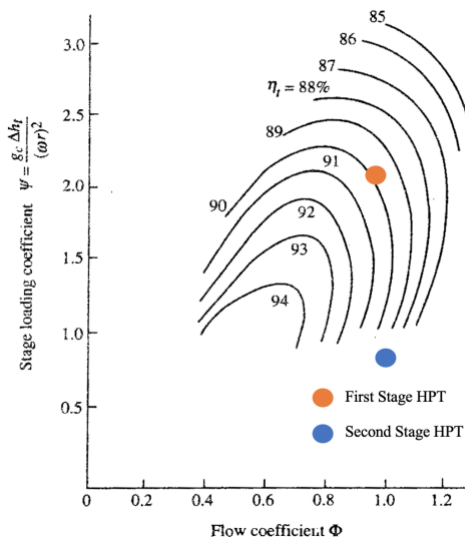


Figure 48.LPT Smith Chart [22].

Finally, the LPT flow path is shown in Figure 50. The maximum radius of the LPT remains below 21 inches, the inner radius of the bypass duct.

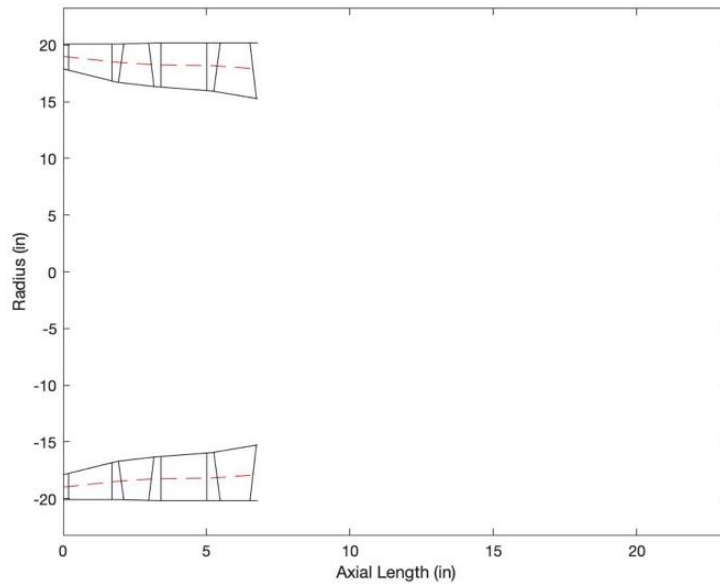


Figure 49. LPT Flow path Drawing.

7.3.2 LPT Blade Design

The blade angles in the LPT are calculated using the incidence and deviation assumptions listed in the HPT blade design section. Per Table XLI, the LPT chokes the first stage nozzle and all remaining blade relative Mach Numbers are subsonic. This ensures that the LPT will not experience high pressure losses and overall increases efficiency.

By assuming free vortex flow, the flow angles across the blade height may be found, seen in Figure 50.

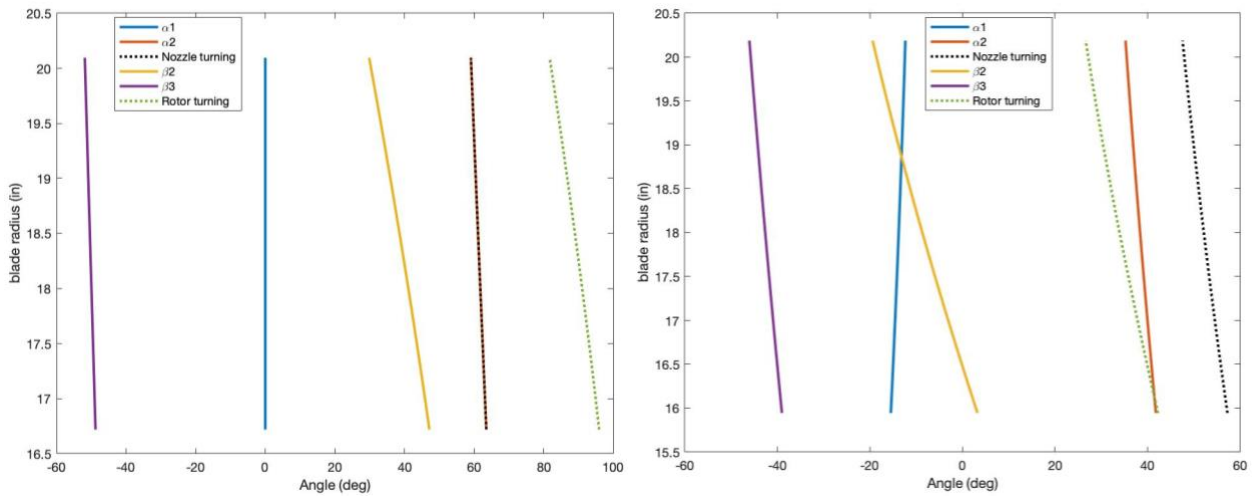


Figure 50. Twist of the 1st and last stage LPT nozzle and rotor blades as a function of blade radius.

Just as in the HPT, the LPT blades have very high turning; Though, the first stage rotor turning in the LPT is lower than in the HPT. The twist from hub to tip is limited to no more than 20° in the LPT, compared to 25° in the HPT. Just as in the HPT, turning is lower in the second stage and the nozzle turns the flow more than the rotor in the second stage. The LPT is uncooled, therefore, there is no need to analyze cooling techniques for the blades.

7.3.3 LPT Off Design Performance

LPT off design performance is analyzed by looking at the scaled LPT map, shown in Figure 51. Like all the other turbomachinery components, this map is from the EEE program. It is scaled using the factors from the NPSS cycle model and the mission operating like is plotted over it. Interestingly, most of the mission points hovered around 95%-110% corrected speed. However, unlike the HPT, the LPT operates at a lower corrected speed during the Taxi and Mach 3.0 mission conditions. Also, at these conditions, the LPT first stage nozzle appears to be unchoked or close to unchoking. This could have significant effects on the engine performance and must be investigated further during testing.

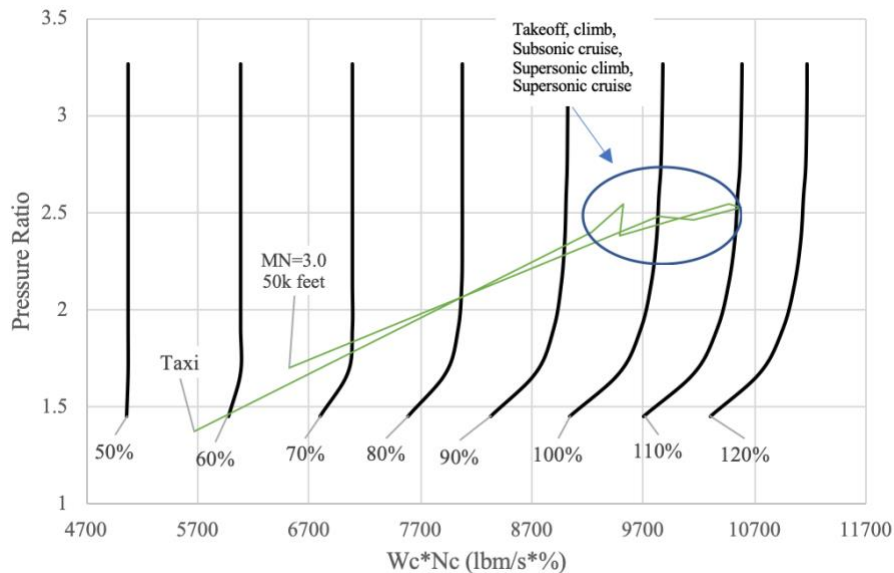


Figure 51. Scaled HPT Map for the YJ-2030 with the Mission Operating line overlaid.

7.4 Materials and Manufacturing

Using the methods described in the compressor “Materials and Manufacturing” section, the required strength for the turbine blades is found. Additionally, the design point AN2 rule and turbine rotor entry temperature is listed. Results are shown in Table XLII.

Table XLII. Turbine Stress Analysis.

	HPT Stage 1 Rotor	HPT Stage 2 Rotor	LPT Stage 1 Rotor	LPT Stage 2 Rotor
Required strength-density ratio (ksi/(slug/ft ³))	3.08	4.08	1.51	1.87
AN2 (in ² *rpm x10 ¹⁰)	4.07E10	5.39E+10	2.11E+10	2.62+10
Maximum Rotor Inlet Temperature (°R)	3001	2734	2376	2198

Analyzing this information allows the team to make a decision on blade materials for the turbine. In the YJ-2030, the turbine rotors and nozzles will be made entirely out of CMCs. CMC turbine blades and nozzles are not new. GE has tested rotating CMC parts in the LPT of their ADVENT engine. They provide longer lifetime and lower weight compared to their traditional nickel superalloy counterparts. The material properties of CMCs are shown in Appendix D.

While the LPT blade could be manufactured out of state of the art nickel superalloys, to lower costs, the reduced weight and longer lifetime of the CMCs overshadow this lower material and manufacturing cost. Furthermore, because the CMCs will have a longer life, they will be replaced less often. This can save owners on maintenance costs which, long-term, add up and dwarf the increased initial cost of the engine.

To produce the first stage HPT blades, the SiC fibers must be 3D printed into a fiber preform. Then, using the PIP process outlined in the combustor materials and manufacturing section, the preceramic polymer may be infiltrated into the preform before the part is sent to autoclave. Post processing includes using electron beam drilling (EBD) to manufacture the small outer cooling holes. 3D printing the HPT blades is required because the inner cooling passages would be extremely difficult to manufacture in post process. This process is has not been implemented on cooled HPT blades and thus poses some risk to the YJ-2030 program. After testing, if the risk is deemed too high, the blade material may be switched to a nickel superalloy. This material is proven to be able to be 3D printed into a single complex part. However, the YJ-2030 cycle would have to be modified to include more cooling for the HPT first stage since nickel superalloys have a lower operating temperature than CMCs.

Second stage HPT blades and all LPT blades are uncooled; Thus, their preform can be manufactured into the general shape of the blade, infiltrated with the preceramic polymer, autoclaved and then cut using a laser microjet as post processing. This manufacturing process is mature and poses no risk to the YJ-2030 project.

Finally, all HPT blades will be coated with a thermal barrier coating (TBC). Per Farhoki, a TBC, such as yttria-stabilized zirconia (YSZ), can increase blade operating temperatures by about 180° R. This can further increase lifetime of the HPT turbine blades. A TBC may be applied to turbine blades using a plasma spray process.

A chart describing the materials and manufacturing methods for the turbine is shown in Table XLIII.

Table XLIII. Turbine Material and Manufacturing summary.

	HPT		LPT	
	Stage 1	Stage 2	Stage 1	Stage 2
Material	CMC blades coated with YSZ as a TBC		CMC blades	
Manufacturing technique	3D printing preform, EBD postprocess Plasma spray for TBC		Traditional Preform, Laser microjet postprocess	
Alternative Manufacturing technique	3D print Nickle Superalloy		N/A-Technology is already mature	

8. Mixer, Afterburner and Mixer Ejector

The YJ-2030 engine architecture features a core-bypass mixer, afterburner and Mixer-Ejector. These components share a common duct to reduce the length and weight in the engine. The following sections outline the purpose of each component and the design.

8.1 Core-Bypass Mixer

In any MFTF, following the LPT, the bypass and core stream must be mixed. State of the art MFTFs utilize a forced-lobed mixer, shown in Figure 52, to mix the two streams. Mixing the two flows slightly improves the performance of the engine of the while lowering the engine jet velocity.



Figure 52. GE Passport Mixer and Center cone [43].

8.1.1 Core-Bypass Mixer Design

To begin the design of the mixer, inlet conditions to the mixer are determined using the cycle design results. Assuming continuity and energy conservation, the outlet conditions to the mixer may be found. At the design point, the static pressures at the entrance to the mixer are made equal by varying the bypass duct entrance MN. Per Frost, the ideal extraction ratio (ER), P_{t16}/P_{t56} , for minimal losses, is approximately 1.0. BPR or FPR may be varied to hit the correct ER. Using the NPSS solver, both the bypass duct MN for a static pressure balance and the FPR needed for an ER=1.0 may be found. Results for the inlet and outlet conditions to the mixer are shown in Table XLIV.

Table XLIV. Mixer Inlet and Outlet Conditions

Parameter	Core Steam Exit	Bypass Stream Exit	Mixer Exit
\dot{W} (lbm/s)	366.12	303.948	670.067
T_t (°R)	2124.06	1048.91	1661.97
P_t (psi)	75.648	75.639	75.446
P_s (psi)	71.355	71.355	70.929
MN	0.3	0.2922	0.3054
Area (in ²)	881.4	513.6	1395.1

The thrust losses due to mixing are accounted for in a mixing correction coefficient. This coefficient lowers the gross thrust coefficient of the nozzle. Using the results above and Equation 13 and Equation 14, the Mixing correction coefficient is found. E is the mixing efficiency and it is assumed to be 80% since the bypass ratio of the engine is close to 1.

$$f_1 = \frac{\dot{W}_{core}\sqrt{T_{t,core}} + \dot{W}_{bypass}\sqrt{T_{t,bypass}}}{(\dot{W}_{core} + \dot{W}_{bypass})\sqrt{T_{t,mixer}}} \quad (13)$$

$$C_{mixing,correction} = E(1 - f_1) + f_1 \quad (14)$$

These calculations yield a $C_{mixing,correction}$ equal to 0.9971.

It is difficult to design a proper mixer for the YJ-2030 without generating a CFD model and rigorously testing the proposed design. Instead, the results found in a NASA study are extrapolated to the YJ-2030 mixer design [44]. The labeling scheme shown in Figure 53 are used for mixer design.

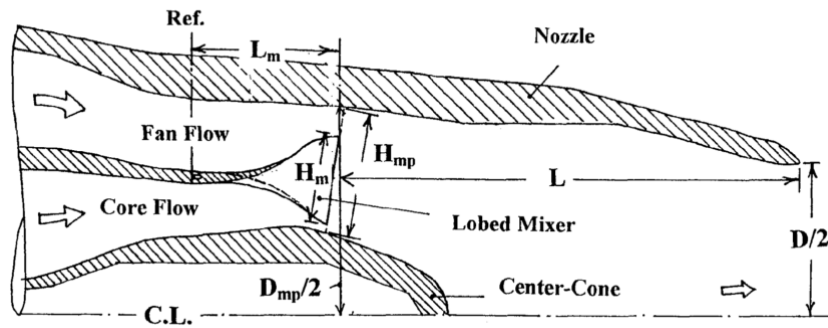


Figure 53. Typical Mixer labeling scheme [44].

Analyzing publicly released information, the GE Affinity features a deeply scalloped, highly lobed mixer with an alternating lobe design. The computer generated image of the GE Affinity mixer is shown in Figure 54.

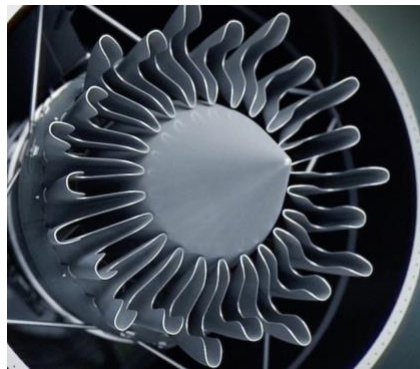


Figure 54. GE Affinity Mixer [23]

The proposed mixer design for the YJ-2030 is a deeply scalloped, highly lobed mixer design. This designed offered good noise suppression across all thrust levels tested with middle of the road losses in the NASA study. Alternating lobe designs should be considered.

Using WATE++ results and the mixer parameters in the NASA study, the proposed mixer dimensions are shown in Table XLV Dimensions for the lobe crest, lobe keel and lobe scallop are not included since they are defined by nonlinear curves.

Table XLV. Mixer Design Results

Parameter	Value
outer radius	24.1265
mixer radius	20.46
plug radius	11.75
Plug Length	13.88
Plug Half angle	40.249309
# of lobes	20

Lobe penetration height	8.292255
Lobe length	16.40602
Lobe angular Spacing	18

8.2 Afterburner

As discussed earlier in the cycle design section, an afterburner is included on the YJ-2030 so that Mach 3.0 may be achieved. Afterburner design is closely intertwined with mixer design; Often, the fuel injector rings lie right before the mixer. A diagram of a EJ200 afterburner design is shown in Figure 55.

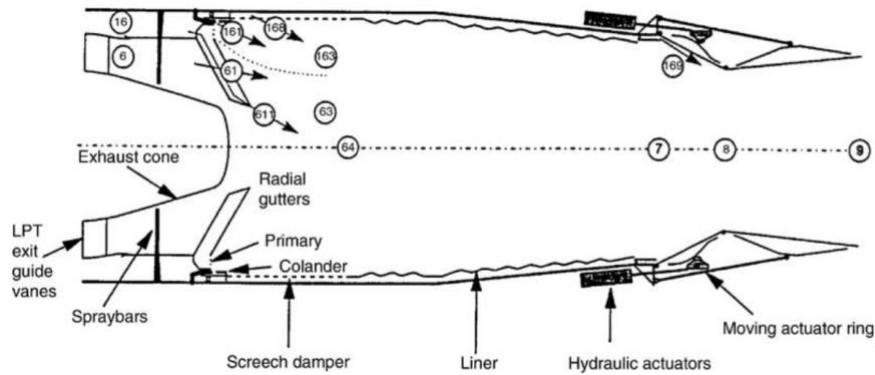


Figure 55. EJ200 Afterburner architecture [15]

8.2.1 Afterburner Design

Design considerations for an afterburner are the weight, length, pressure loss and efficiency of the system. The design point for the afterburner is considered to be Mach 3.0, the point where maximum afterburner operation is required. The afterburner inlet conditions and fuel flow are shown in Table XLVI for the Mach 3.0 condition.

Table XLVI. Afterburner Inlet Conditions

Parameter	Value
\dot{W}_{fuel} (lbm/s)	627.262
P_{t6} (psi)	72.21
T_{t6} (°R)	1519.54
T_{t65} (°R)	2791.11
MN_6	0.3252
W_{fuel} (lbm/s)	15.05814

An afterburner with staged fuel injection is installed on the YJ-2030. Staged fuel injection is preferred so that heat addition rate can be gradually increased. The YJ-2030 afterburner injection system consists of multiple circular tubes with small holes with each injection ring having the ability to control the fuel flow. The YJ-2030 utilizes two arc igniters sitting inside the wake of a flame stabilizers with its own dedicated fuel supply

In terms of flame stabilization, bluff-body vee-gutter flame holders are installed. The technology is quite mature while also offering a low total pressure loss.

The maximum temperature in the afterburner reaches 2800 °R. Even though this temperature is cooler than the main combustor, the afterburner duct liner will still need to be cooled. This is done by bypassing some of the exhaust gas around the liner.

Finally using the figures presented by Mattingly, the afterburner length, efficiency and total pressure loss are estimated based on the YJ-2030 SLS BPR [22]. Results are shown in Table XLVII.

Table XLVII. Afterburner Design Conditions

Parameter	Value
Afterburner Efficiency	94%
Pressure Loss	0.018
Diameter (in)	24.1
Length(in)	34.974

8.3 Mixer Ejector

The Stage 5 noise constraints placed on the aircraft and its engine drive the need for a noise suppressing exhaust system. Besides changing the cycle or engine architecture, which would cause issues of its own, one of the only noise suppression options on aircraft engines is a mixer ejector nozzle system. This system uses the velocity of the exhaust gases to draw in ambient air. This phenom is depicted in Figure 56 and lowers the exit jet velocity with a small gross thrust loss at takeoff.

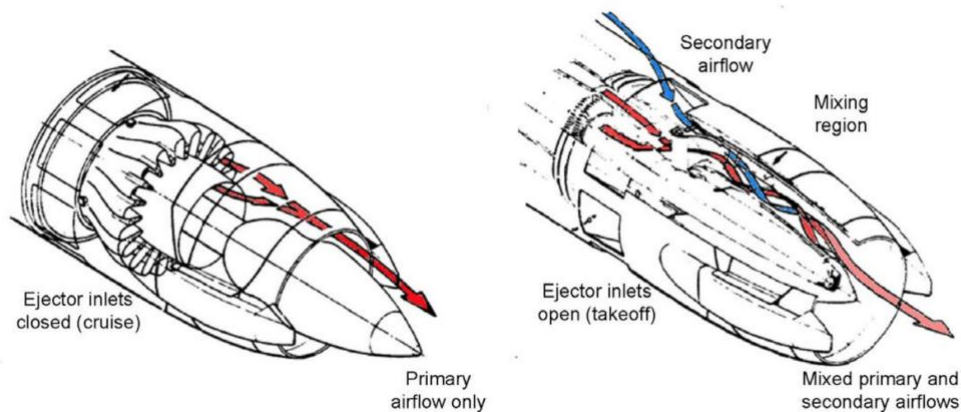


Figure 56. JT8D ejector nozzle showing cruise (left) and takeoff (right) operation. [45]

Since the 8th power of jet velocity is proportional to noise, a decrease in jet velocity will have dramatic noise damping.

8.3.1 Mixer Ejector Design

To design the mixer ejector, the mass flow augmentation (MFA) required to reduce the jet velocity down to acceptable levels must be found. The mass flow augmentation is the amount of ambient air drawn in, normalized by the unaugmented exhaust mass flow.

In order to determine the amount of MFA required a 1993, 1994 mixer-ejector nozzle MFA severity model was modified [7]. The model showed a relationship between nozzle jet velocity and the MFA needed to reduce the jet velocity down to 1450 ft/s. The model is shown in Figure 57.

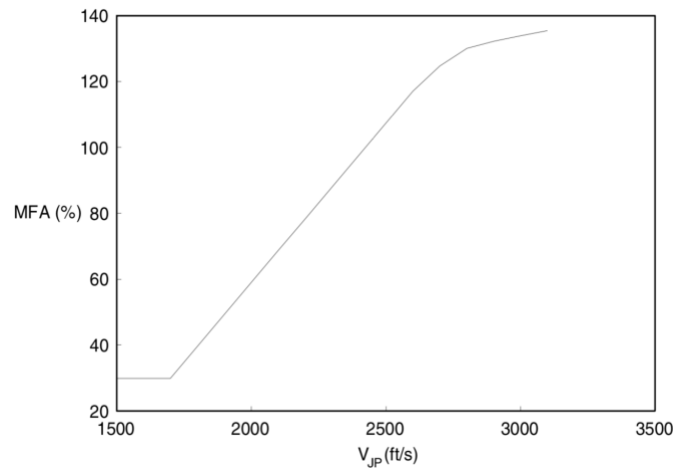


Figure 57. NASA Mixer Ejector Model [7].

Since the estimated jet velocity requirement is different today than in 1993, the x-axis of the model was modified to be a percent decrease in jet velocity; Simply, the x-axis was divided by 1450 ft/s. The new model is shown in Figure 58.

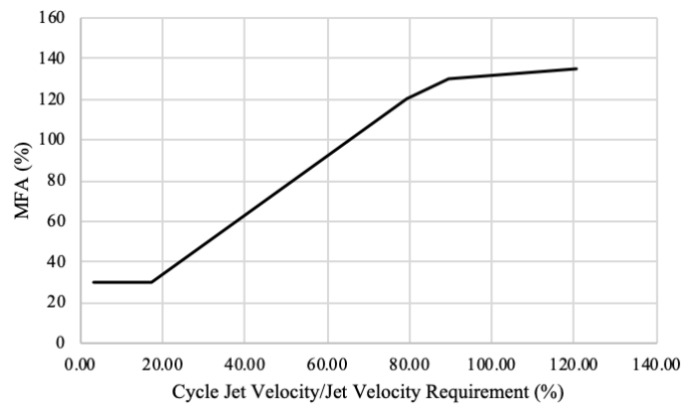


Figure 58. Modified Mixer Ejector Model.

As determined in the requirements section, to meet Stage-5 noise requirements, the YJ-2030 would need an effective jet velocity of 1100 ft/s. Thus, using Figure 58, the YJ-2030 would need a MFA of 65% at takeoff and 30% during descent.

The cycle is mostly unaffected by the addition of a mixer ejector. Per Berton a constant nozzle thrust coefficient of 0.95 is assumed during the portions of flight when the ejector is active. Outside of these conditions, the cycle and nozzle performance is unaffected by the mixer ejector [7].

The ejector inlets will be installed right after the core-bypass mixer. This allows the ambient air to utilize the mixer and afterburner duct as mixing region. Combining all three of these components into a single mixing duct drastically reduces the engine length.

8.4 Materials and Manufacturing

The GE Passport mixer and center cone, seen above in Figure 52, was manufactured purely out of ceramic matrix composites. Typically, the mixer and center body would have been manufactured out steel or titanium. Using CMCs instead, leads to drastic weight savings and does not compromise the structure of the engine. Also, the entire afterburner system, besides the fuel ejector rings, will be manufactured out of CMCs to save weight. The fuel rings will be manufactured out of nickel alloy . To further increase afterburner lifetime, a thermal barrier coating may be applied to the flameholder, liner and fuel injection rings.

9. Nozzle

The YJ-2030 features a fully variable, axisymmetric, converging diverging nozzle. The propelling nozzle in a gas turbine engine converts the thermal energy of the flow into kinetic energy with a minimum pressure loss to generate gross thrust. Design considerations of the nozzle include performance across the flight envelope, simplicity, footprint, weight and noise suppression.

9.1 Nozzle Architecture

The nozzle design for the YJ-2030 nozzle began by selecting its architecture. Due to the high operating Mach Number, high nozzle pressure ratio (NPR), and afterburning capability, a fully variable, axisymmetric, convergent-divergent (C-D) nozzle is considered. C-D nozzles allow for 5% or greater increase in ideal gross thrust at NPRs of 6 or higher. Additionally, a fully variable C-D nozzle allows for control of the fan operating line in MFTFs, which is required during afterburner operation to prevent fan surge. Control of the fan operating line also allows for TSFC

optimization throughout the envelope. These factors combined outweigh the complexity and weight concerns that plaque variable C-D nozzles. The addition of the mixer ejector does not significantly affect the nozzle architecture.

9.2 Nozzle Design

Now that the architecture has been decided, design may begin. A MATLAB code is written that performs the nozzle analysis and design for a given set of cycle inputs. The code is based off of a C-D nozzle design procedure outlined by Mattingly [22]. A drawing of a C-D nozzle showing the dimensions and parameters is shown in Figure 59.

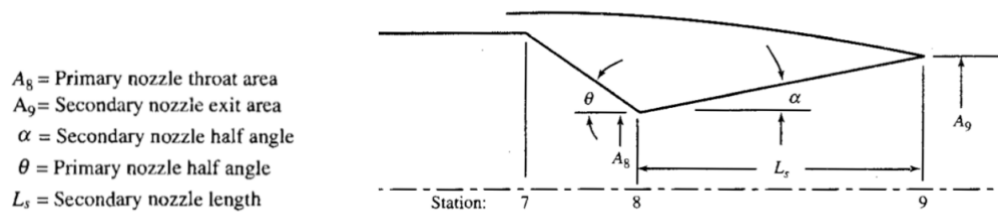


Figure 59. Typical Nozzle Dimensions and Parameters [22].

Choosing the top of climb, $MN=2.1$ at 40,000 feet, as the nozzle design point allows the team to set the nozzle dimensions. The MATLAB code is rerun at off design points such as takeoff and Mach 3.0, afterburner operation, to understand the performance of the nozzle. It should be mentioned that C_v and C_{fg} coefficients calculated below were not used in the cycle analysis because they do not account for mixing corrections and the effect of the mixer-ejector system. At takeoff, the input mass flow accounts for the engine cycle mass flow plus the MFA from the mixer ejector. Results of the nozzle design study are shown in Table XLVIII.

Table XLVIII. Nozzle Design Results

	MN = 2.1	MN = 3.0	MN = 0
\dot{W} (lbm/s)	670.07	645.85	717.69
T_{t7} (°R)	1662.78	2833.15	1036.95
P_{t7} (psi)	73.94	70.75	36.57
P_{amb} (psi)	2.72	1.68	14.70
Tailpipe Area (in²)	1260.60	1260.60	1260.60
Tailpipe Radius (in)	20.03	20.03	20.03
Throat Area (in²)	721.34	960.40	1220.63
Throat Radius (in)	15.15	17.48	19.71
Exit Area (in²)	2498.73	4719.42	1220.63
Exit Radius (in)	15.15	17.48	19.71
Exit Velocity (ft/s)	3535.96	4907.60	1448.90
Discharge Coefficient	0.98	0.98	0.98
Velocity Coefficient	1.00	1.00	0.89
Gross Thrust Coefficient	0.978	0.978	0.969
Theta (°)	10.19	5.36	0.68

Alpha (°)	11.93	19.00	0.00
Axial Convergent Length (in)	27.13	27.45	27.57
Axial Divergent Length (in)	61.78	59.45	63.14
Total Axial Length (in)	88.91	86.90	90.70

Using the information generated from the MATLAB code, a 2-D flowpath sketch of the nozzle may be generated, shown in Figure 60. In the figure, just the angle of the convergent and divergent flaps change, their lengths are fixed.

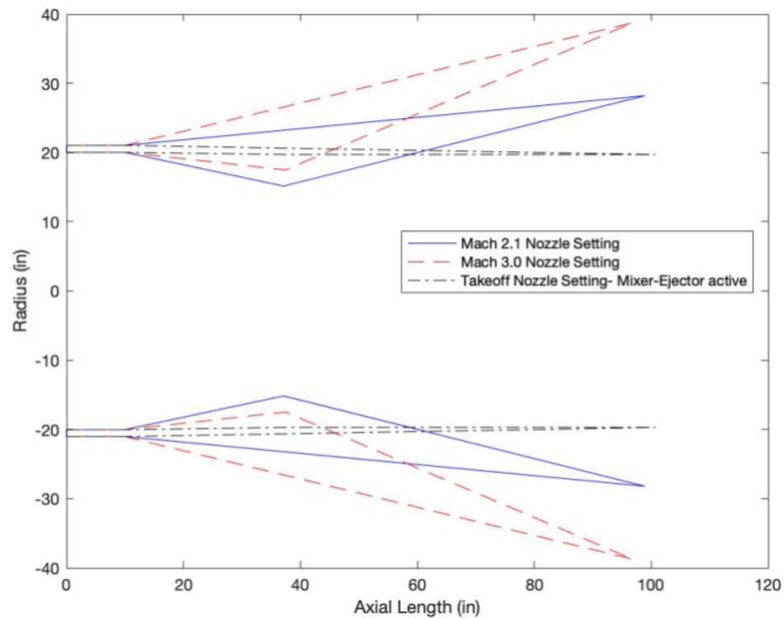


Figure 60. Drawing of the nozzle flow path at different operating conditions

Actuators adjust the angle of convergent and divergent flaps to meet the A8/A9 schedule determined by the cycle. A schematic showing the general method of actuation of the variable convergent divergent nozzle is shown below in Figure 61

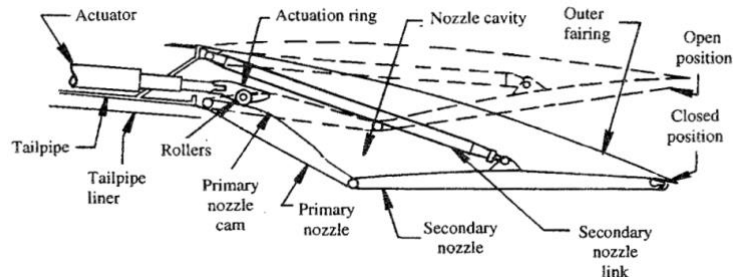


Figure 61. CD Nozzle Actuation Schematic [22].

During FAS certification, if the mixer ejector does not provide enough noise suppression to meet Stage-5 noise requirements, the exit of the nozzle divergent flap may be easily modified to include a chevron tab design. This

sawtooth pattern, as seen in Figure 62, provides up to ~3 EPN dB of noise suppression at the expense of a small gross thrust coefficient loss.

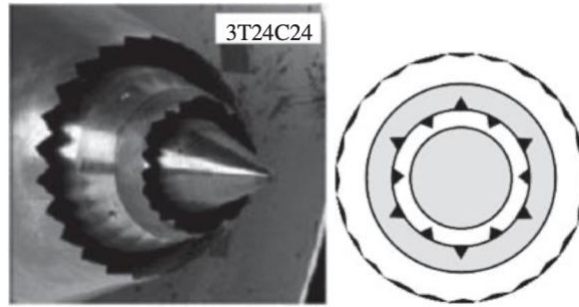


Figure 62. Chevron Nozzle Pattern [15].

9.3 Nozzle Off Design Performance

As with all major components, the off design performance should be analyzed. For the nozzle, this includes how the nozzle coefficients, the nozzle afterbody drag, and the nozzle area ratio changes across the flight envelope.

Using the relationships discussed in Mattingly, the discharge coefficient is assumed to be constant at 0.98. In the cycle model, the nozzle velocity coefficient is assumed constant at 0.98 throughout the flight envelope when the mixer-ejector doors are closed. When the doors are open, the velocity coefficient decreases to 0.95. The gross thrust coefficient may be calculated by multiplying the velocity coefficient by the mixing correction coefficient. The NASA PIPSI curve relationships were not applicable to the nozzle coefficients because the curves did not approximate the coefficients for the area ratios and NPRs that occurred in the YJ-2030 nozzle. When flight tests occur for the YJ-2030, the constant velocity/discharge coefficient assumption should be replaced in the cycle analysis with a velocity/discharge coefficient as a function of NPR and area ratio.

In terms of afterbody drag calculations, the NASA PIPSI curve are able to be applied. The “208NTY” afterbody drag curve is used. This nozzle is a single, axisymmetric C-D nozzle configuration, exactly like the YJ-2030. The afterbody drag coefficient graph is shown below in Figure 63.

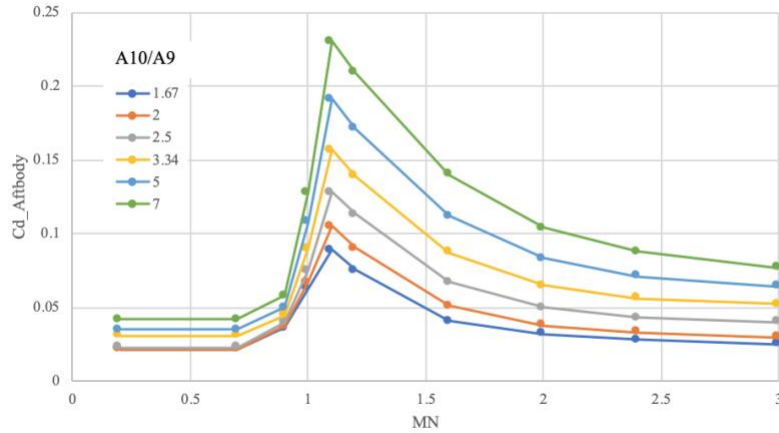


Figure 63. YJ-2030 Afterbody Drag Relationship [20].

The nozzle coefficients and afterbody drag at the different flight conditions is shown in Figure 64.

Figure 64. YJ-2030 Nozzle Performance at different flight conditions

Mission stage	Drag due to inlet (lbf)	Cd	Cv (lb _m /s)	Cfg
Overland Cruise (40k, 1.15 MN)	150	0.980	0.980	0.977
Oversea Cruise (40k, 2.1 MN)	494	0.980	0.980	0.977
Overland Cruise (50k, .98 MN)	33	0.980	0.980	0.977
Takeoff (SLS)	0	0.980	0.950	0.948

As mentioned earlier, the variable operation of the C-D nozzle allows for control of the fan operating line. More specifically, this allows the YJ-2030 to prevent fall surge during augmentor operation and also allows for TSFC optimization in other off design situations. Figure 65 illustrates how a change in A8 will affect the operating line

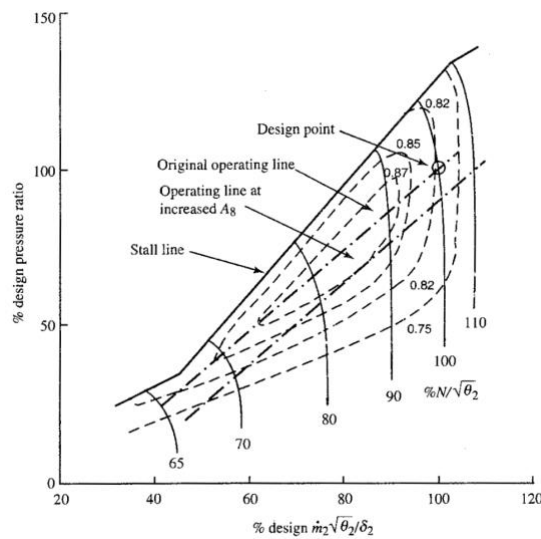


Figure 65. Effect of variable A8 on fan operating line [22].

Using the cycle model, an Area schedule for the nozzle as a function of Mach Number may be created, shown in Figure 66. This area schedule was created by optimizing TSFC while maintaining at least a 10% stall margin on the Fan compressor map.

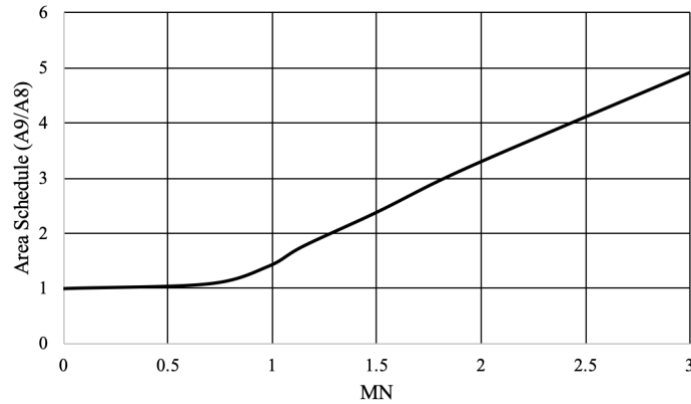


Figure 66. YJ-2030 Nozzle Area Schedule.

9.4 Materials and Manufacturing

The YJ-2030 nozzle will be manufactured with its diverging and converging nozzle flaps made out of ceramic matrix composites. This reduces the weight of the engine compared to flaps that are made of nickel alloy. CMC nozzle divergent flaps, seen in Figure 67 have been tested on the F-16 nozzle as early as 2005 [46].

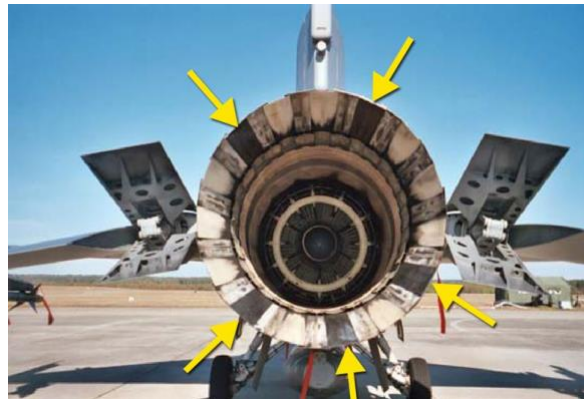


Figure 67. CMC Divergent Nozzle Flaps on a F-16 Nozzle [46]

The technology is quite mature and poses no significant risk to the YJ-2030 program.

10. Engine Control System

The YJ-2030 features a modern full authority digital engine control (FADEC) to control the engine. The purpose of an engine control system is to ensure that the engine properly responds to a pilot input without exceeding engine limits and damaging components.

The general engine state space can be represented as a collection of flow properties at different stations in the engine. A few system state variables include: the exhaust gas temperature (EGT), P_3 , N_1 and N_2 . The pilot control can be represented as a scalar throttle input. In response to a throttle input, the FADEC has the ability to control the fuel to air ratio, nozzle area ratio, guide vane angles and the oil supply. The system block diagram is shown in Figure 68.

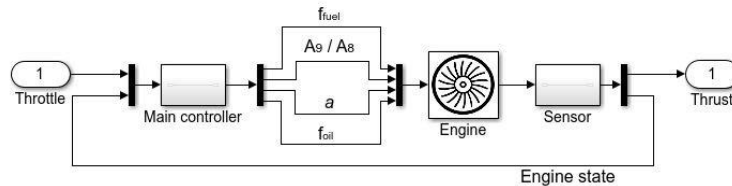


Figure 68. YJ-2030 FADEC Block Diagram.

Using modern control theory, the FADEC's main controller simultaneously changes the 4 engine inputs described above subject to constraints for each of the state variables. These constraints arise as a non-linear combination of various inherent engine system limitations, such as blade clearance constraints, material temperature limits, compressor stall limits and vibrational frequency restrictions. Each input governs an actuator that regulates the engine state. Finally, the FADEC forms a closed loop control configuration by inferring the engine state variables via a number of sensors installed to measure each of them directly forwarding them to the main controller.

11. Final Engine Flow path and Engine Weight Analysis

The engine flow path and weight were determined using NASA Weight Analysis of Turbine Engine (WATE++) [47]. This software integrates itself with NPSS in order to use the cycle thermodynamic information to size the engine flow path and determine engine weight. WATE++ can include structural frame components and has the ability to determine the turbomachinery disk shape.

Using the information determined in each component design section, the YJ-2030 WATE++ model could be created. Some of the many WATE inputs include: number of turbomachinery stages, blade ARs, blade solidities, density of component material and duct lengths. While WATE++ is a strong tool for weight estimation, it has its limitations. WATE++ does not have the ability to properly estimate the weight of blisked compressors nor the weight of an afterburner. A 0.90 factor was applied to the weight of the HPC to account for the implementation of blisks [48].

To account for the afterburner weight, the weight of the GE F110, a similarly sized (49.2'' vs. 46.5'') afterburning MFTF, was subtracted from the weight of the GE F118, its non-afterburning derivative . Then a factor of 0.8 was applied to this weight to account for the implementation of CMC components. This method should give a reasonable estimation of the added weight of an afterburner.

The WATE++ weight results are shown in Table XLIX. The proposed YJ-2030 is about 200 lbm lighter than the baseline engine, even with an afterburner included. The decrease in weight can be attributed to utilizing low density, high strength, materials across the engine and also decreasing the number of turbomachinery stages compared to the baseline engine.

Table XLIX. WATE++ Results for the YJ-2030

Component	Weight (lbm)
Fan	1674.2
Swan Neck Duct	137.4
HPC	350.8
Burner	256.0
HPT	291.9
ITT duct	10.2
LPT	287.1
Bypass duct	476.5
Mixer	25.9
Afterburner	576.0
HP Shaft	64.6
LP Shaft	187.3
Dry Wright Less Nozzle	4337.9

The flow path for the YJ-2030 is shown in Figure 69. The yellow blades represent structural frames and red represents the fan containment system.

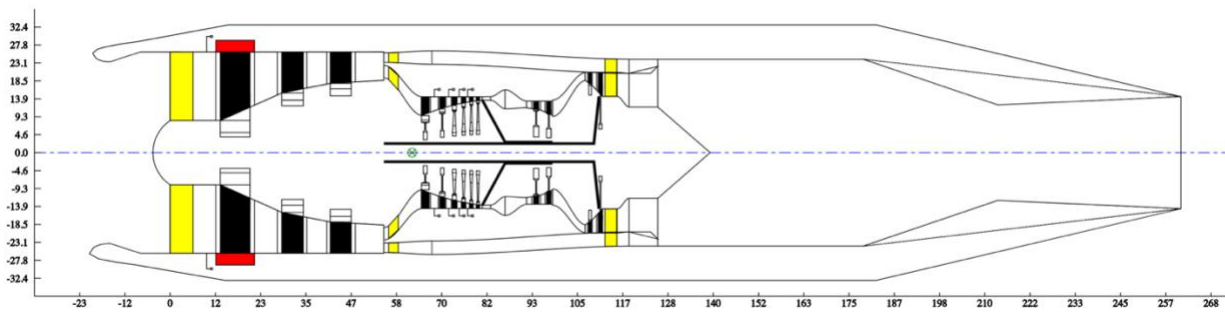


Figure 69. YJ-2030 WATE++ Flow path.

The YJ-2030 has a fan diameter of 49.2'', a total engine length of 260'' and an inlet length of 219''. If the diverging part of the YJ-2030 nozzle is not included in the overall length of the engine, the total length of the nacelle is 416'' or 34.7 inches. Just a 0.7 feet longer than the estimated nacelle length in the RFP.

12. Conclusion

In summary, the YJ-2030 is a candidate engine to be installed on the next supersonic business jet. The engine allows the aircraft to cruise at Mach 2.1, with a maximum speed of Mach 3.0. The design of the YJ-2030 began by setting the engine requirements and optimizing the cycle for maximum range. Each major flow path component was designed with low weight, high efficiency and high reliability in mind. A final component and performance summary is shown in Table L.

Table L. YJ-2030 Component and Performance Summary

Component	Description
Engine Architecture	Afterburning Mixed Flow Turbofan
Inlet	4 shock, 2-D Mixed Compression Supersonic inlet
Fan	3-Stage High Efficiency Fan with Polyimide Fan Blades
HPC	6 Stage All Blisk HPC
Burner	Next generation annular, lean-premixed combustor
HPT	2 Stage cooled HPT manufactured from CMC
HPC	2 Stage uncooled LPT manufactured from CMC
Mixer	Full composite deeply scalloped, highly lobed mixer design
Afterburner	Shares duct with mixer-ejector and core-bypass mixer to reduce length
Nozzle	Fully Variable Axisymmetric Converging Diverging Nozzle
Performance Metric	Value
Fan Diameter	49.2''
Weight (lbm)	4338
Engine + Inlet Length (feet)	34.66 feet
NYC to London Fuel burn (lbm)	92769
Time for NYC to London	4:57
Range at Mach 0.98, 40000 feet (nm)	5300
Takeoff Exit Jet Velocity	1100 ft/s with Mixer-Ejector Active
Supercruise NOx emissions	4.83 g/kg
LTO cycle NOx	Does Not Meet Requirement*

*NOx relationships must be revisited after combustor testing

In conclusion, the YJ-2030 meets all the engine requirements besides LTO cycle NOx emissions while maximizing the aircraft range. Assumptions during design and the technologies implemented in the engine are not overly risky and should not pose a risk to the success of the engine.

References

- [1] A. J. Yatsko, "Candidate Engines for a Supersonic Business Jet," American Institute of Aeronautics and Astronautics, Reston, 2019.
- [2] Pratt & Whitney, General Electric Aircraft Engines, Critical Propulsion Components Volume 1: Summary, Introduction, and Propulsion Systems Studies, Glenn Research Center: NASA, 2005.
- [3] Southwest Research Institute, "What Is Numerical Propulsion System Simulation (NPSS®)?," San Antonio, 2019.
- [4] Federal Aviation Administration, "Stage 5 Airplane Noise Standards," 2017.
- [5] European Aviation Safety Agency, "Improvement in aircraft noise performance has occurred over time," 2020.
- [6] H. R. Welge, "N+2 Supersonic Concept Development and Systems Integration," NASA, Hampton, 2010.
- [7] J. J. Berton, W. J. Haller, P. F. Senick, S. M. Jones and J. A. Seidel, "A Comparative Propulsion System Analysis for the High-Speed Civil Transport," NASA Glenn Research Center, Cleveland, Ohio, 2005.
- [8] T. Kellner, "This News Travels Fast: Boeing's Partnership With Aerion Could Supercharge Supersonic Travel," GE Aviation, 8 February 2019. [Online]. Available: <https://www.ge.com/reports/news-travels-fast-boeings-partnership-aerion-supercharge-supersonic-travel/>. [Accessed 22 February 2020].
- [9] T. Kellner, "The Superjet: Building the Ultimate Flying Machine," GE Aviation, 4 March 2014. [Online]. Available: <https://www.ge.com/reports/post/78469596586/the-superjet/>. [Accessed 2 February 2020].
- [10] V. Kuz'michev, I. Krupenich, E. Filinov and Y. Ostapyuk, "Comparative Analysis of Mathematical Models for Turbofan Engine Weight Estimation," MATEC Web of Conferences, Samara, 2018.
- [11] I. A. E., O. Ikechukwu, P. O. Egunilo and E. Ikpe, "Material Selection for High Pressure (HP) Compressor Blade of an Aircraft Engine".
- [12] J. W. Gatmtner, "Algorithm for Calculating Turbine Cooling Flow and the Resulting Decrease in Turbine Efficiency," NASA Technical Memorandum, 1980.
- [13] GE Aviation Blog, "In aviation's material world, GE's CMCs unlock opportunity," 2018.
- [14] B. L. Koff, "GAS TURBINE TECHNOLOGY EVOLUTION - A DESIGNER'S PERSPECTIVE," AIAA, Palm Beach Gardens, 2003.
- [15] S. Farokhi, Aircraft Propulsion Second Edition, Wiley, 2014.
- [16] R. Avellán, On the Design of Energy Efficient Aero Engines Some Recent Innovations, Göteborg, 2011.
- [17] E. A. Timby, "Airflow Rate Requirements in Passenger Aircraft," MINISTRY OF AVIATION SUPPLY, Farnborough, 1970.
- [18] D. Scholz, R. Seresinhe, I. Staack and C. Lawson, "FUEL CONSUMPTION DUE TO SHAFT POWER OFF-TAKES FROM THE ENGINE," AST, Hamburg, 2013.
- [19] T. H. Frost, "Practical Bypass Mixing Systems for Fan Jet Aero Engines," 1965.
- [20] E. J. Kowalski and R. A. Atkins Jr., A Computer Code for Estimating Installed Performance of Aircraft Gas Turbine Engines, Seattle: Boeing Military Airplane Company, 1979.
- [21] H. Ran and D. Mavris, "Preliminary Design of a 2D Supersonic Inlet to Maximize Total Pressure Recovery," *American Institute of Aeronautics and Astronautics*, 2005.
- [22] J. D. Mattingly, Elements of Gas Turbine Propulsion, McGraw-Hill, 2005.
- [23] GE Aviation, "The Affinity™ Supersonic turbofan," [Online]. Available: <https://www.geaviation.com/bga/engines/ge-affinity/>. [Accessed 12 February 2020].
- [24] J. Kurzke and I. Halliwell, Propulsion and Power An Exploration of Gas Turbine Performance Modeling, Cham: Springer, 2018.
- [25] GE Aviation, "The GE90 Engine," [Online]. Available: <https://www.geaviation.com/commercial/engines/ge90-engine/>. [Accessed 15 February 2020].
- [26] P. J. Cavano and W. E. Winters, "PMR Polyimide/Graphite Fiber Composite Fan Blades," NASA, Cleveland, 1976.

- [27] GE Aviation, "Proven Experience, Program Upgrades Spark GE F110 and F404/414 Popularity," [Online]. Available: <https://www.geaviation.com/press-release/military-engines/proven-experience-program-upgrades-spark-ge-f110-and-f404414>. [Accessed 4 May 2020].
- [28] J. Bayliff, A. Billberg, R. Blom, N. Gallegor, O. Holke and S. Sandford, "Research and Development of Additive Manufactured Bladed Disks," Gothenburg, 2017.
- [29] U.S. National Archives, "DAMAGED STATOR SECTORS OF J-85-21 ENGINE," U.S. National Archives, 1978.
- [30] Technicut, "BLISK," 5 May 2020. [Online]. Available: <https://www.technicut.co.uk/blisk>.
- [31] Y. Liu, X. Sun, V. Sethi, D. Nalianda, Y.-G. Li and L. Wang, "Review of modern low emissions combustion technologies for aero gas turbine engines," Aerospace Sciences, Bedfordshire, 2017.
- [32] M. J. Foust, D. Thomsen, R. Stickles, C. Cooper and W. Dodds, "Development of the GE Aviation Low Emissions TAPS Combustor for Next Generation Aircraft Engines," AIAA, Nashville, 2012.
- [33] J. Seay and G. Samuelson, "Atomization and Dispersion of a Liquid Jet Injected Into a Crossflow of Air," NASA, Irvine, 1996.
- [34] David L. Heiserman, "IGNITERS," SweetHaven , 2015.
- [35] J. Li, X. Sun, Y. Liu and V. Sethi, "Preliminary Aerodynamic Design Methodology for Aero Engine Lean Direct Injection Combustors," Aeronautical Journal, Shenyang, 2017.
- [36] J. M. Seitzman, *Common Engine Atomizers*, Atlanta, 2017.
- [37] General Electric, "TAPS II Combustor Final Report," FAA, Washington, DC, 2014.
- [38] Paradigm, "Paradigm Capabilities," Paradigm, [Online]. Available: <http://www.palmermfgco.com/capabilities/>. [Accessed 10 5 2020].
- [39] D. García, *Ceramic Matrix Composites Manufacturing and Applications in the Automotive Industry*, Bristol.
- [40] R. Denney, Interviewee, *Turbine Design Guidelines*. [Interview]. 4 May 2020.
- [41] D. A. Sagerser, S. Lieblein and R. P. Krebs, "Empirical Expressions for Estimating Length and Weight of Axial-Flow components of VTOL Powerplants," NASA, Cleveland, 1971.
- [42] P. G. Hill and C. R. Peterson, *Mechanics and Thermodynamics of Propulsion*, Addison-Wesley, 1992.
- [43] CompositesWorld, "Ceramic matrix composites: Hot engine solution," 17 April 2017. [Online]. Available: <https://www.compositesworld.com/articles/ceramic-matrix-composites-hot-engine-solution>. [Accessed 12 May 2020].
- [44] V. G. Mengle and W. N. Dalton, "Lobed Mixer Design for Noise Suppression," NASA, Indianapolis, 2002.
- [45] E. S. Hendricks and J. A. Seidel, *A Multidisciplinary Approach to Mixer-Ejector Analysis and Design*, Cleveland: Glenn Research Center, 2012.
- [46] P. Meltzer, "Ceramic Matrix Composite seals proving reliable for jet engine nozzles," 8 July 2008. [Online]. Available: <https://www.wpafb.af.mil/News/Article-Display/Article/400832/ceramic-matrix-composite-seals-proving-reliable-for-jet-engine-nozzles/>. [Accessed 13 May 2020].
- [47] NASA, "Weight Analysis of Turbine Engine - an Object-Oriented Version (WATE)," [Online]. Available: <https://software.nasa.gov/software/LEW-19687-1>. [Accessed 20 1 2020].
- [48] Rolls Royce, "Trent XWB," [Online]. Available: https://www.rolls-royce.com/products-and-services/civil-aerospace/airlines/trent-xwb.aspx#/. [Accessed 20 April 2020].
- [49] Cytec, "AVIMID N POLYIMIDE COMPOSITE," [Online]. Available: <https://www.e-aircraftsupply.com/MSDS/15754cytec%20AVIMID%20N%20tds.pdf>. [Accessed 5 May 2020].
- [50] TIMET, "TIMETAL 834," [Online]. Available: <https://www.timet.com/assets/local/documents/datasheets/alphaalloys/834.pdf>. [Accessed 5 May 2020].
- [51] J. Chesnutt, "Titanium Aluminides for Aerospace Applications," The Minerals, Metals & Materials Society, Cincinnati, 1992.
- [52] M.-K. Seo and P. Soo-jin, *Interface Science and Composites*, Incheon: Academic Press, 2011.

Appendix A- Baseline Engine NPSS Output

Summary Output Data														
MN	alt	dTamb	W	Fg	Fn	TSFC	BPR	VTAS	OPR	T4	T41	humRel		
0.00	0.0	0.00	477.2	21698.9	21698.9	0.4719	1.70	0.00	11.66	2492.0	2433.9	0.000		
FLOW STATION DATA														
	W	Pt	Tt	FAR	ht	Wc	Ps	Ts	Aphy	MN	Rt	gamt		
FS0 InEngStart_FL_0	477.229	14.696	518.67	0.0000	123.95	477.23	14.696	518.67	-----	0.0000	0.0686	1.40052		
FS1 Inlet_FL_0	477.229	14.696	518.67	0.0000	123.95	477.23	12.388	493.92	1863.0	0.5000	0.0686	1.40052		
FS2 Fan_FL_0	477.229	27.922	634.58	0.0000	151.79	277.83	25.077	615.44	1301.4	0.3950	0.0686	1.39830		
FS14 Split_FL_02	300.478	27.922	634.58	0.0000	151.79	174.93	25.001	614.91	810.0	0.4006	0.0686	1.39830		
FS23 Split_FL_01	176.752	27.922	634.58	0.0000	151.79	102.90	24.566	611.84	448.8	0.4318	0.0686	1.39830		
FS25 SwanNeckDuct_FL_0	176.752	27.922	634.58	0.0000	151.79	102.90	25.212	616.39	492.5	0.3848	0.0686	1.39830		
FS26 IPC_FL_0	176.752	78.182	867.72	0.0000	208.35	42.97	65.974	827.40	168.3	0.5000	0.0686	1.38868		
FS27 ICd_FL_0	176.752	76.619	867.72	0.0000	208.35	43.85	64.654	827.40	171.7	0.5000	0.0686	1.38868		
FS3 HPC_FL_0	171.449	325.629	1333.93	0.0000	325.72	12.41	266.400	1264.58	45.9	0.5500	0.0686	1.35983		
FS31 CDPBld_FL_0	152.007	325.629	1333.93	0.0000	325.72	11.00	301.113	1306.51	59.1	0.3410	0.0686	1.35983		
FS32 OGVdct_FL_0	152.007	325.629	1333.93	0.0000	325.72	11.00	323.427	1331.53	189.4	0.1000	0.0686	1.35983		
FS4 BrnPri_FL_0	154.851	309.348	2492.00	0.0187	658.94	16.12	301.437	2477.07	144.3	0.2000	0.0685	1.30118		
FS45 HPT_FL_0	174.294	126.991	1956.28	0.0166	501.90	39.17	108.010	1881.08	156.8	0.5000	0.0685	1.31799		
FS48 ITTduct_FL_0	174.294	124.452	1956.28	0.0166	501.90	39.97	112.438	1908.85	192.4	0.3946	0.0685	1.31799		
FS5 LPT_FL_0	179.596	36.063	1458.67	0.0161	363.85	122.73	32.478	1420.27	582.8	0.3972	0.0685	1.34135		
FS56 TEGVduct_FL_0	179.596	35.783	1458.67	0.0161	363.85	123.97	24.682	1326.88	387.9	0.7575	0.0685	1.34135		
FS15 FanBld_FL_0	300.478	27.922	634.58	0.0000	151.79	174.93	26.544	625.50	1141.8	0.2700	0.0686	1.39830		
FS16 BPduct_FL_0	300.478	27.224	634.58	0.0000	151.79	179.41	24.682	617.10	873.4	0.3770	0.0686	1.39830		
FS6 Mix_FL_0	480.074	29.895	956.17	0.0060	231.12	320.43	25.281	912.97	1261.3	0.4983	0.0686	1.37939		
FS7 Tailpipe_FL_0	480.074	29.895	956.17	0.0060	231.12	320.43	26.059	920.67	1360.8	0.4500	0.0686	1.37939		
FS9 NozPri_FL_0	480.074	29.895	956.17	0.0060	231.12	320.43	15.842	801.77	937.8	1.0000	0.0686	1.37939		
TURBOMACHINERY PERFORMANCE DATA														
	Wc Wp	PR	eff	TR	effPoly	Nc Np	pwr	SMN	SMW					
Fan	477.23	1.900	0.9000	1.2235	0.9086	100.0	-18796.7	20.00	13.17					
IPC	102.90	2.800	0.9197	1.3674	0.9302	90.4	-14144.7	19.10	9.94					
HPC	43.85	4.250	0.9010	1.5373	0.9181	77.3	-28867.3	13.28	13.39					
HPT	24.99	2.436	0.9219	1.2104	0.9138	2.0	29558.6							
LPT	61.94	3.451	0.9268	1.3238	0.9152	2.3	33274.1							
TURBOMACHINERY MAP DATA														
	WcMap	PRmap	effMap	NcMap	s_WcDes	s_PRdes	s_effDes	s_NcDes	RlineMap					
Fan	3200.00	1.500	0.9150	1.000	0.1491	1.8000	0.9836	100.0	2.0000					
IPC	187.67	1.710	0.8969	1.000	0.5483	2.5338	1.0254	90.4	2.0000					
HPC	123.57	24.136	0.8216	1.000	0.3549	0.1405	1.0966	77.3	2.0000					
HPT	15.77	4.975	0.9220	100.000	1.5851	0.3613	0.9999	0.0200						
LPT	78.56	4.271	0.9171	100.000	0.7885	0.7493	1.0106	0.0226						
DUCTS														
	dPqP	MNin	Aphy	BLEEDS - interstg										
SwanNeckD>	0.00000	0.4318	448.75	C_FS49 HPC.ChargeLPT	Wb Win	dhb/dh	dPb/dP	W	Tt	ht	Pt			
ICD	0.02000	0.5000	168.30	C_FS50 HPC.notChargeLPT	0.0033	0.4500	0.4286	0.5892	1080.79	261.17	183.34			
OGVduct	0.00000	0.3410	59.05	BLEEDS - output										
ITTduct	0.02000	0.5000	156.82	C_FS41 CDPBld.CDPBldA	Wb Win	hscale	Pscale	W	Tt	ht	Pt			
TEGVduct	0.01000	0.3972	582.84	C_FS42 CDPBld.CDPBldB	0.0600	1.0000	1.0000	10.6127	1333.93	325.72	325.63			
BPduct	0.02500	0.2700	1141.76	C_FS14 FanBld.FanBld	0.0000	1.0000	1.0000	0.0000	634.58	151.79	27.92			
Tailpipe	0.00000	0.4983	1261.33											
SPLITTERS														
Split	BPR	dP/P1	dP/P2											
Split	1.70000	0.0000	0.0000											
SHAFTS														
SH	Nmech	trqIn	pwrIn	HPX										
SH	100.000	1552449.8	29558.6	100.00										
SHL	100.000	1747595.3	33274.1	0.00										
BURNERS														
BrnPri	TtOut	eff	dPqP	Wfuel	FAR									
BrnPri	2492.00	0.9950	0.0500	2.84459	0.01871									
MIXERS														
Mix	PtRatio	MN1	MN2	partialMix										
Mix	0.7625	0.757	0.377	0.6000										
NOZZLES														
NozPri	type	PR	Cfg	CdTh	Cv	Cang	CmixCorr	Cqua	Ath	MNth	Vactual	Fg	FgIdeal	Vid,full
NozPri	conic	2.034	1.0000	0.9600	1.0000	1.0000	1.0000	1.0000	976.90	1.000	1382.1	21698.9	21698.9	1454.2

Figure 70. Baseline Engine NPSS Model Output

Appendix B- YJ-2030 NPSS Outputs

Summary Output Data															
MN	alt	dTamb	W	Fg	Fn	TSFC	BPR	VTAS	OPR	T4	T41	Wfuel/hr			
2.10	40000.0	0.00	704.3	72000.0	30380.1	1.0486	0.85	2033.81	27.89	3366.0	3338.8	31856.6			
INSTALLED PERFORMANCE															
Wengine	Wbypass	Wbleed	Fram	FgIn	FnIn	TSFCin	eRam	Dinlet	Dnozz	Acppt	A0AC	Fan Diam			
658.41	0.00	45.87	41620.2	71115.9	29001.6	1.0984	0.9313	884.39	494	2887	0.8575	49			
FLOW STATION DATA															
	W	Pt	Tt	FAR	ht	Wc	Ps	Ts	Aphy	MN	Rt	gamt			
FS0 InEngStart.Fl_0	704.287	24.890	733.79	0.0000	175.74	494.61	2.720	389.97	2648.8	2.1000	0.0686	1.39488			
FS1 Inlet.Fl_0	658.414	23.179	733.79	0.0000	175.74	496.53	18.183	684.97	1721.1	0.6000	0.0686	1.39488			
FS2 Fan.Fl_0	658.414	77.201	1048.98	0.0000	253.20	178.24	69.442	1018.87	840.0	0.3950	0.0686	1.37765			
FS13 Split.Fl_02	302.514	77.201	1048.98	0.0000	253.20	81.90	69.235	1018.03	381.5	0.4006	0.0686	1.37765			
FS23 Split.Fl_01	355.899	77.201	1048.98	0.0000	253.20	96.35	68.044	1013.17	422.7	0.4318	0.0686	1.37765			
FS25 SwanNeckDuct.Fl_0	355.899	76.043	1048.98	0.0000	253.20	97.81	68.766	1020.36	471.0	0.3848	0.0686	1.37765			
FS3 HPC.Fl_0	355.899	646.366	1915.37	0.0000	481.33	15.55	584.803	1868.12	75.2	0.3900	0.0686	1.33138			
FS31 CDPBld.Fl_0	345.610	646.366	1915.37	0.0000	481.33	15.10	598.629	1879.07	81.9	0.3410	0.0686	1.33138			
FS32 OGVduct.Fl_0	345.610	646.366	1915.37	0.0000	481.33	15.10	630.242	1903.35	136.8	0.1951	0.0686	1.33138			
FS4 BrnPri.Fl_0	354.459	620.511	3366.01	0.0256	932.15	21.39	604.838	3347.14	192.8	0.2000	0.0685	1.28182			
FS45 HPT.Fl_0	364.393	191.881	2598.03	0.0249	695.74	62.46	173.677	2539.61	303.1	0.3946	0.0685	1.29464			
FS48 ITTduct.Fl_0	364.393	189.003	2598.03	0.0249	695.74	63.41	171.072	2539.61	307.7	0.3946	0.0685	1.29464			
FS5 LPT.Fl_0	364.393	76.236	2124.05	0.0249	555.08	142.15	68.845	2073.71	683.1	0.3972	0.0685	1.30674			
FS56 TEGVduct.Fl_0	364.393	75.664	2124.05	0.0249	555.08	143.22	71.371	2095.08	877.1	0.3000	0.0685	1.30674			
FS15 FanBld.Fl_0	302.514	77.201	1048.98	0.0000	253.20	81.90	73.448	1034.71	538.2	0.2700	0.0686	1.37765			
FS16 BPduct.Fl_0	302.514	75.657	1048.98	0.0000	253.20	83.57	71.370	1032.30	511.0	0.2923	0.0686	1.37765			
FS6 Mix.Fl_0	666.907	75.463	1662.00	0.0134	418.15	232.49	70.944	1636.54	1388.1	0.3054	0.0686	1.33270			
FS63 Mix_duct.Fl_0	666.907	75.463	1662.00	0.0134	418.15	232.49	69.567	1628.54	1229.0	0.3509	0.0686	1.33267			
FS65 Afterburner.Fl_0	666.907	73.954	1662.00	0.0134	418.37	237.29	68.204	1629.50	1257.1	0.3500	0.0686	1.33267			
FS7 Tailpipe.Fl_0	666.907	73.954	1662.00	0.0134	418.37	237.29	68.176	1629.33	1254.4	0.3509	0.0686	1.33267			
FS9 NozPri.Fl_0	666.907	73.954	1662.00	0.0134	418.37	237.29	2.720	688.54	2533.5	2.7748	0.0686	1.33267			
TURBOMACHINERY PERFORMANCE DATA															
	Wc Wp	PR	eff	TR	effPoly	Nc Np	pwr	SMN	SMW						
Fan	496.53	3.331	0.9293	1.4295	0.9400	84.1	-72155.8	30.48	16.98						
HPC	97.81	8.500	0.9091	1.8259	0.9300	70.3	-114874.5	13.28	13.39						
HPT	33.14	3.234	0.9560	1.2825	0.9500	1.724	115546.8								
LPT	98.27	2.479	0.9639	1.2231	0.9600	1.962	72516.8								
TURBOMACHINERY MAP DATA															
	WcMap	PRmap	effMap	NcMap	s_WcDes	s_PRdes	s_effDes	s_NcDes	RlineMap						
Fan	3000.81	1.396	0.9365	0.910	0.1655	5.8845	0.9923	92.4	2.0000						
HPC	123.57	24.136	0.8216	1.000	0.7916	0.3242	1.1065	70.3	2.0000						
HPT	15.77	4.975	0.9220	100.000	2.1022	0.5620	1.0369	0.0172							
LPT	78.56	4.271	0.9171	100.000	1.2508	0.4522	1.0511	0.0196							
DUCTS															
	dPqP	MNin	Aphy												
SwanNeckDuct	0.01500	0.4318	422.66												
OGVduct	0.00000	0.3410	81.86												
ITTduct	0.01500	0.3946	303.06												
TEGVduct	0.00750	0.3972	683.07												
BPduct	0.02000	0.2700	538.17												
Mix_duct	0.00000	0.3054	1388.12												
Tailpipe	0.00000	0.3500	1257.14												
BLEEDS - output															
	Wb/Win	hscale	Pscale	W	Tt	ht	Pt								
C_FS11 CDPBld.CustBleed	0.0010	1.0000	1.0000	0.3559	1915.37	481.33	646.37								
TrbH_CH CDPBld.TCLA_CH	0.0073	1.0000	1.0000	2.5976	1915.37	481.33	646.37								
TrbH_NC CDPBld.TCLA_NC	0.0206	1.0000	1.0000	7.3356	1915.37	481.33	646.37								
C_FS14 FanBld.FanBld	0.0000	1.0000	1.0000	0.0000	1048.98	253.20	77.20								
SPLITTERS															
	BPR	dP/P1	dP/P2												
Split	0.85000	0.0000	0.0000												
SHAFTS															
	Nmech	trqIn	pwrIn	HPX											
SH	100.000	6068650.9	115546.8	110.00											
SHL	100.000	3808664.8	72516.8	0.00											
BURNERS															
	TtOut	eff	dPqP	Wfuel	FAR										
BrnPri	3366.01	0.9990	0.0400	8.84905	0.02560										
Afterburner	1662.80	0.9000	0.0200	0.00000	0.01345										
MIXERS															
	PtRatio	MN1	MN2	partialMix	T_Mix	Mixingcorr									
Mix	0.9999	0.300	0.292	0.8000	1612	0.9971									
NOZZLES															
	type	PR	Cfg	CdTh	Cv	Cang	CmixCorr	Cqua	Ath	MNth	Vactual	Fg	FgIdeal	Vid,full	Area_schedule
NozPri	CON_DIV	27.189	0.9772	0.9600	0.9800	1.0000	0.9971	1.0000	731.32	1.000	3473.6	72000.3	73682.0	3554.7	3.464

Figure 71. YJ-2030 NPSS Output at Design point

Summary Output Data															
MN	alt	dTamb	W	Fg	Fn	TSFC	BPR	VTAS	OPR	T4	T41	Wfuel/hr			
0.00	0.0	0.00	431.0	21700.4	21700.4	0.5035	1.00	0.00	21.84	2225.9	2208.1	10927.2			
INSTALLED PERFORMANCE															
Wengine	Wbypass	Wbleed	Fram	FgIn	FnIn	TSFCin	eRam	Dinlet	Dnoz	Acapt	A0AC	Fan Diam			
430.98	0.00	0.00	0.0	21700.4	21700.4	0.5035	0.9700	0.00	0	2887	0.3407	49			
FLOW STATION DATA															
		W	Pt	Tt	FAR	ht	Wc	Ps	Ts	Aphy	MN	Rt	gamt		
FS0	InEngStart.Fl_0	430.984	14.696	518.67	0.0000	123.95	430.98	14.696	518.67	----	0.0000	0.0686	1.40052		
FS1	Inlet.Fl_0	430.984	14.439	518.67	0.0000	123.95	438.66	12.199	494.25	1721.1	0.4965	0.0686	1.40052		
FS2	Fan.Fl_0	430.984	38.888	699.61	0.0000	167.47	189.16	34.407	675.71	840.0	0.4223	0.0686	1.39602		
FS13	Split.Fl_02	215.130	38.888	699.61	0.0000	167.47	94.42	33.276	669.32	381.5	0.4776	0.0686	1.39602		
FS23	Split.Fl_01	215.854	38.888	699.61	0.0000	167.47	94.74	34.454	675.98	422.7	0.4199	0.0686	1.39602		
FS25	SwanNeckDuct.Fl_0	215.854	38.305	699.61	0.0000	167.47	96.18	34.775	680.67	471.0	0.3746	0.0686	1.39602		
FS3	HPC.Fl_0	215.854	315.280	1303.33	0.0000	317.81	15.95	283.540	1267.03	75.2	0.3972	0.0686	1.36169		
FS31	CDPBld.Fl_0	209.614	315.280	1303.33	0.0000	317.81	15.49	290.698	1275.48	81.9	0.3469	0.0686	1.36169		
FS32	OGVduct.Fl_0	209.614	315.280	1303.33	0.0000	317.81	15.49	306.995	1294.14	136.8	0.1981	0.0686	1.36169		
FS4	BrnPri.Fl_0	212.649	302.668	2225.87	0.0145	577.90	21.39	295.029	2212.41	192.8	0.1978	0.0686	1.31082		
FS45	HPT.Fl_0	218.673	91.244	1672.26	0.0141	421.24	63.24	82.363	1630.05	303.1	0.3943	0.0686	1.33179		
FS48	ITTDuct.Fl_0	218.673	89.876	1672.26	0.0141	421.24	64.20	81.128	1630.05	307.7	0.3943	0.0686	1.33179		
FS5	LPT.Fl_0	218.673	37.455	1353.29	0.0141	335.05	138.59	34.040	1320.17	683.1	0.3786	0.0686	1.34884		
FS56	TEGVduct.Fl_0	218.673	37.174	1353.29	0.0141	335.05	139.64	35.179	1334.10	877.1	0.2869	0.0686	1.34884		
FS15	FanBld.Fl_0	215.130	38.888	699.61	0.0000	167.47	94.42	36.322	686.19	538.2	0.3141	0.0686	1.39602		
FS16	BPduct.Fl_0	215.130	38.110	699.61	0.0000	167.47	96.35	35.169	683.84	511.0	0.3411	0.0686	1.39602		
FS6	Mix.Fl_0	433.803	37.450	1038.46	0.0070	251.94	240.87	35.035	1019.78	1388.1	0.3128	0.0686	1.37346		
FS63	Mix_duct.Fl_0	433.803	37.450	1038.46	0.0070	251.94	240.87	34.296	1013.87	1229.0	0.3599	0.0686	1.37346		
FS65	Afterburner.Fl_0	433.803	36.701	1038.92	0.0070	252.06	245.84	33.625	1014.45	1257.1	0.3589	0.0686	1.37343		
FS7	Tailpipe.Fl_0	433.803	36.701	1038.92	0.0070	252.06	245.84	33.610	1014.33	1254.4	0.3599	0.0686	1.37343		
FS9	NozPri.Fl_0	433.803	36.701	1038.92	0.0070	252.06	245.84	14.696	807.18	748.3	1.2254	0.0686	1.37343		
TURBOMACHINERY PERFORMANCE DATA															
Fan	Wc	PR	eff	TR	effPoly	Nc Np	pwr	SMN	SMW						
438.66	2.693	0.9357	1.3489	0.9440	74.4	-26537.8	39.83	18.00							
HPC	96.18	8.231	0.9157	1.8629	0.9358	69.8	-45913.5	15.05	15.30						
HPT	33.15	3.317	0.9560	1.3179	0.9492	1.719	46254.5								
LPT	99.50	2.400	0.9573	1.2357	0.9524	1.820	26666.4								
TURBOMACHINERY MAP DATA															
Fan	WcMap	PRmap	effMap	NcMap	s_WcDes	s_PRdes	s_effDes	s_NcDes	RlineMap						
2650.56	1.288	0.9430	0.886	0.1655	5.8845	0.9923	92.4	1.9329							
HPC	121.50	23.305	0.8276	0.993	0.7916	0.3242	1.1065	70.3	2.0462						
HPT	15.77	5.123	0.9220	99.746	2.1022	0.5620	1.0369	0.0172							
LPT	79.54	4.095	0.9108	92.786	1.2508	0.4522	1.0511	0.0196							
DUCTS															
SwanNeckD>	dPqP	MNin	Aphy	BLEEDS - output											
0.01500	0.4199	422.66		C_FS11	CDPBld.CustBleed	0.0010	1.0000	1.0000	0.2159	1303.33	317.81	315.28			
OGVduct	0.00000	0.3469	81.86	TrbH_CH	CDPBld.TCLA_CH	0.0073	1.0000	1.0000	1.5755	1303.33	317.81	315.28			
ITTDuct	0.01500	0.3943	303.06	TrbH_NC	CDPBld.TCLA_NC	0.0206	1.0000	1.0000	4.4491	1303.33	317.81	315.28			
TEGVduct	0.00750	0.3786	683.07	C_FS14	FanBld.FanBld	0.0000	1.0000	1.0000	0.0000	699.61	167.47	38.89			
BPduct	0.02000	0.3141	538.17												
Mix_duct	0.00000	0.3128	1388.12												
Tailpipe	0.00000	0.3589	1257.14												
SPLITTERS															
Split	BPR	dP/P1	dP/P2												
0.99664	0.0000	0.0000													
SHAFTS															
SHH	Nmech	trqIn	pwrIn	HPX											
81.112	2995031.1	46254.5	110.00												
SHL	74.441	1881419.3	26666.4	0.00											
BURNERS															
BrnPri	TtOut	eff	dPqP	Wfuel	FAR										
2225.87	0.9990	0.0400	3.03533	0.01448											
Afterburner	1038.92	0.9000	0.0200	0.00000	0.00705										
MIXERS															
Mix	PtRatio	MN1	MN2	partialMix	T_Mix	Mixingcorr									
1.0252	0.287	0.341	0.8000	I011	0.9973										
NOZZLES															
NozPri	type	PR	Cfg	CdTh	Cv	Cang	CmixCorr	Cqua	Ath	MNth	Vactual	Fg	FgIdeal	Vid,full	Area_schedule
CON_DIV	2.497	0.9475	0.9600	0.9500	1.0000	0.9973	1.0000	750.00	1.000	1609.5	21700.4	22903.8	1698.7	0.998	

Figure 72. YJ-2030 NPSS Output at Takeoff

Appendix C- YJ-2030 Inlet Maps

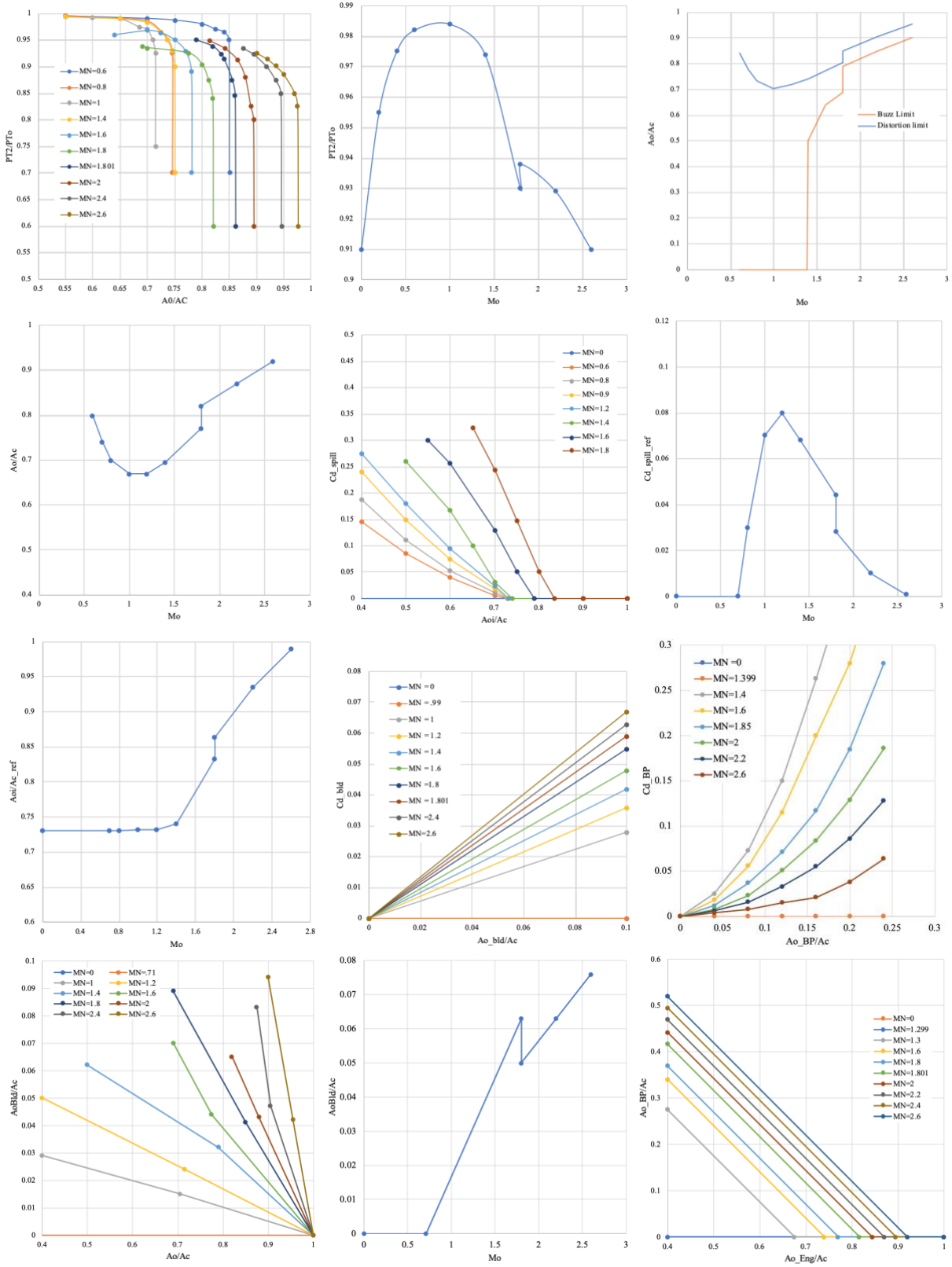


Figure 73. YJ-2030 Inlet Maps.

Appendix D: Material Properties

Table LI. AVIMID® N Material Properties [49].

Material Properties	Value
Density (lbm/in ³)	0.0524
0.2% Yield Strength (ksi)	66.72
Specific Strength at Temperature (ksi/(slug/ft ³))	23.71
Max Operating Temperature (°R)	1200

Table LII. TI-834 Material Properties [50].

Material Properties	Value
Density (lbm/in ³)	0.1643
0.2% Yield Strength (ksi)	65.26
Specific Strength at Temperature (ksi/(slug/ft ³))	7.39
Max Operating Temperature (°R)	1570

Table LIII. Ti48Al2Cr2Nb Material Properties [51].

Material Properties	Value
Density (lbm/in ³)	0.1409
0.2% Yield Strength (ksi)	43.51
Specific Strength at Temperature (ksi/(slug/ft ³))	5.75
Max Operating Temperature (°R)	2000

Table LIV. CMC Material Properties [52]

Material Properties	Value
Density (lbm/in ³)	0.0759
0.2% Yield Strength (ksi)	38.00
Specific Strength at Temperature (ksi/(slug/ft ³))	9.32
Max Operating Temperature (°R)	3000

Appendix E: Fan Velocity Triangles

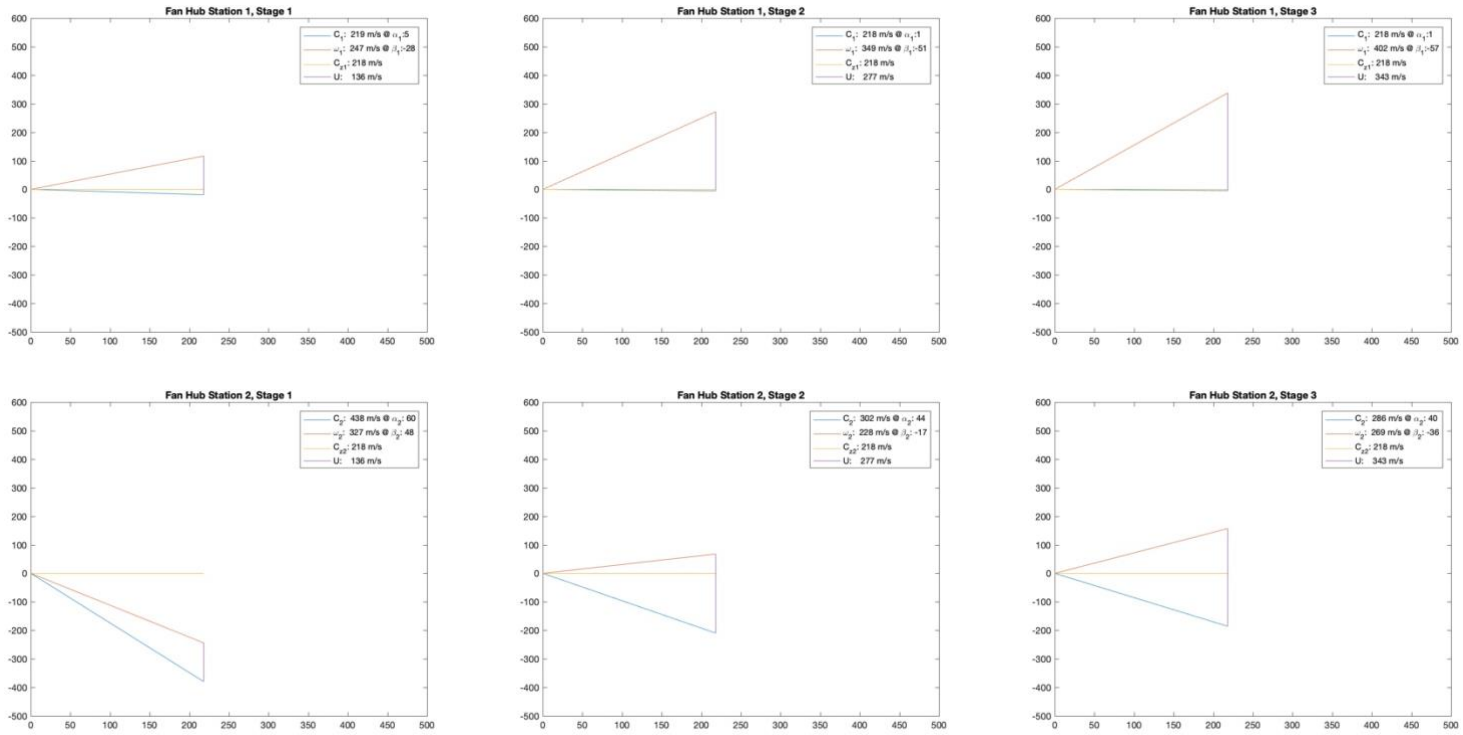


Figure 74. Fan Hub Velocity Triangles

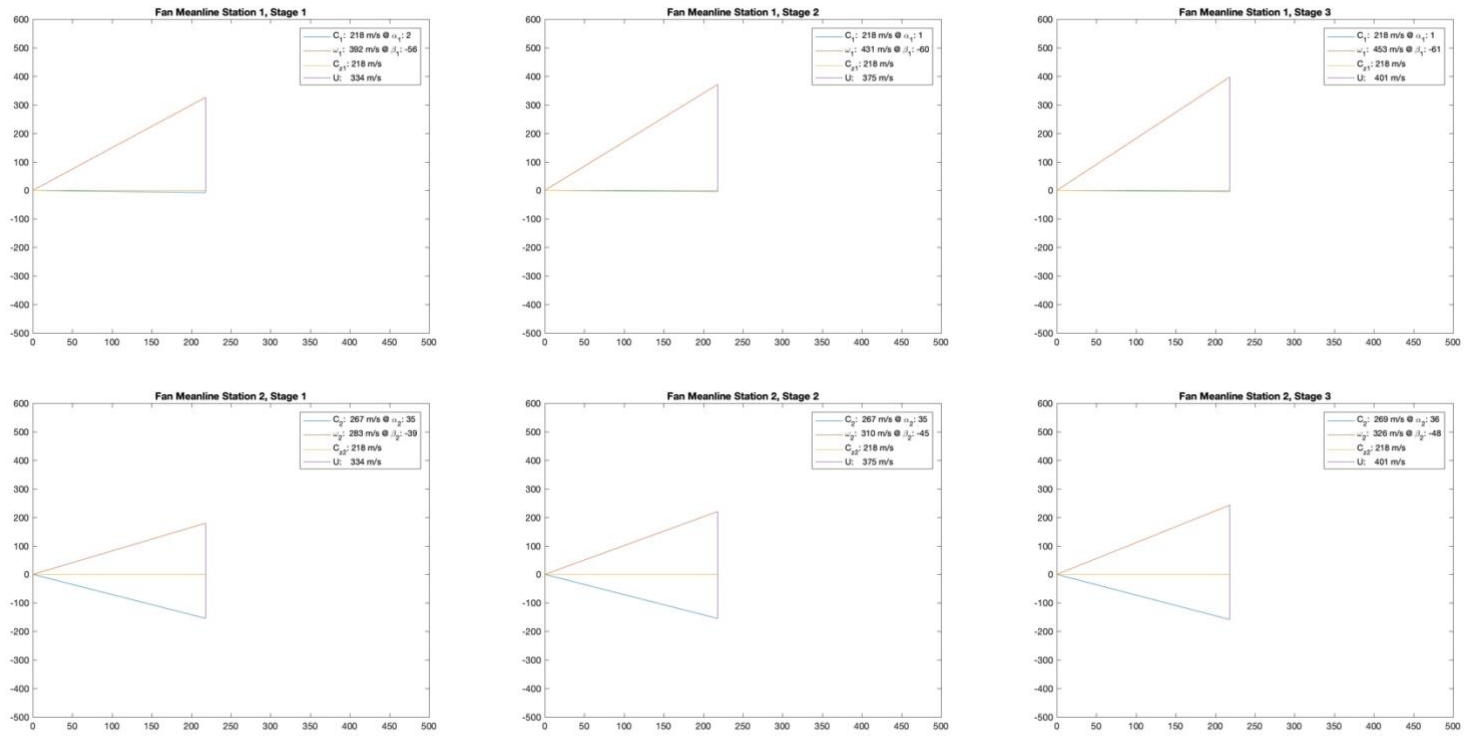


Figure 75. Fan Mean-line Velocity Triangles

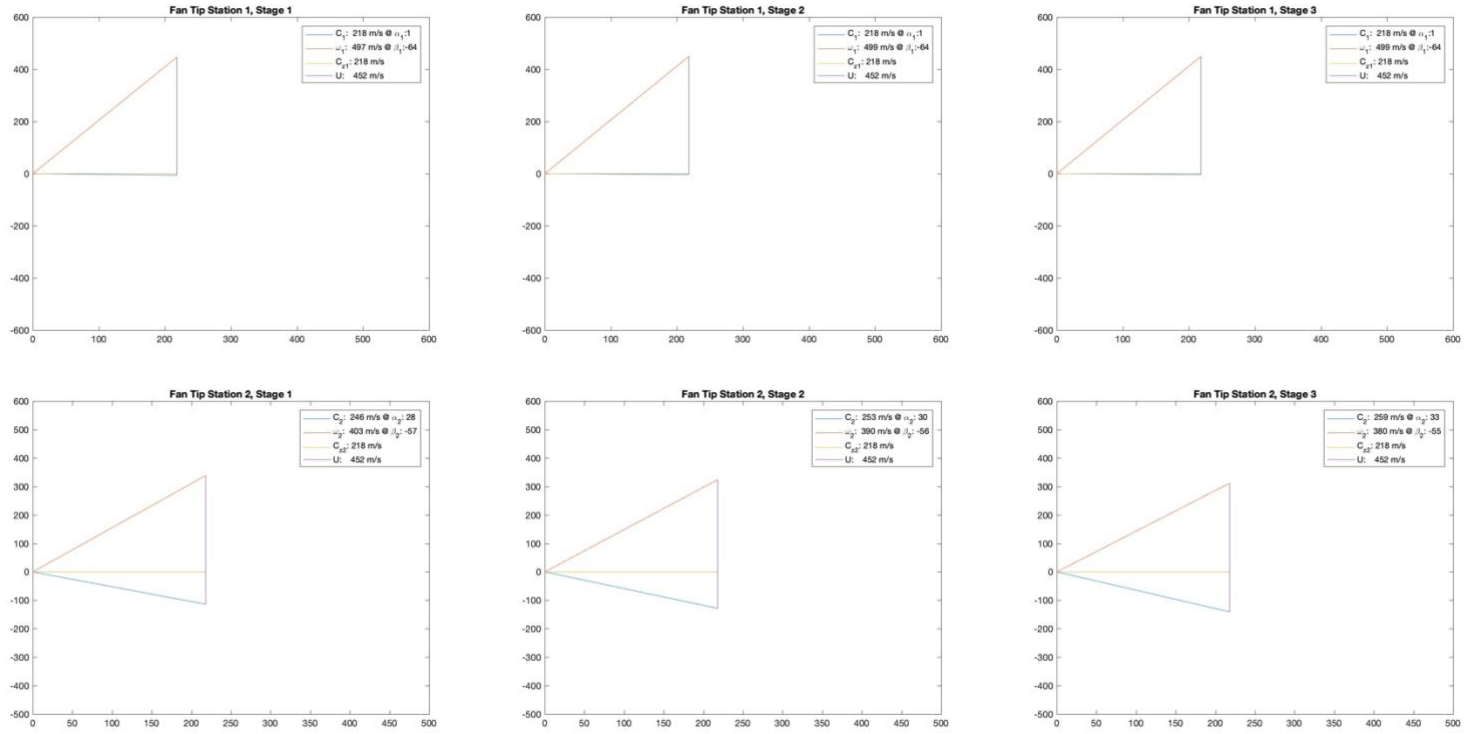


Figure 76. Fan Tip Velocity Triangles

Appendix F: HPC Velocity Triangles

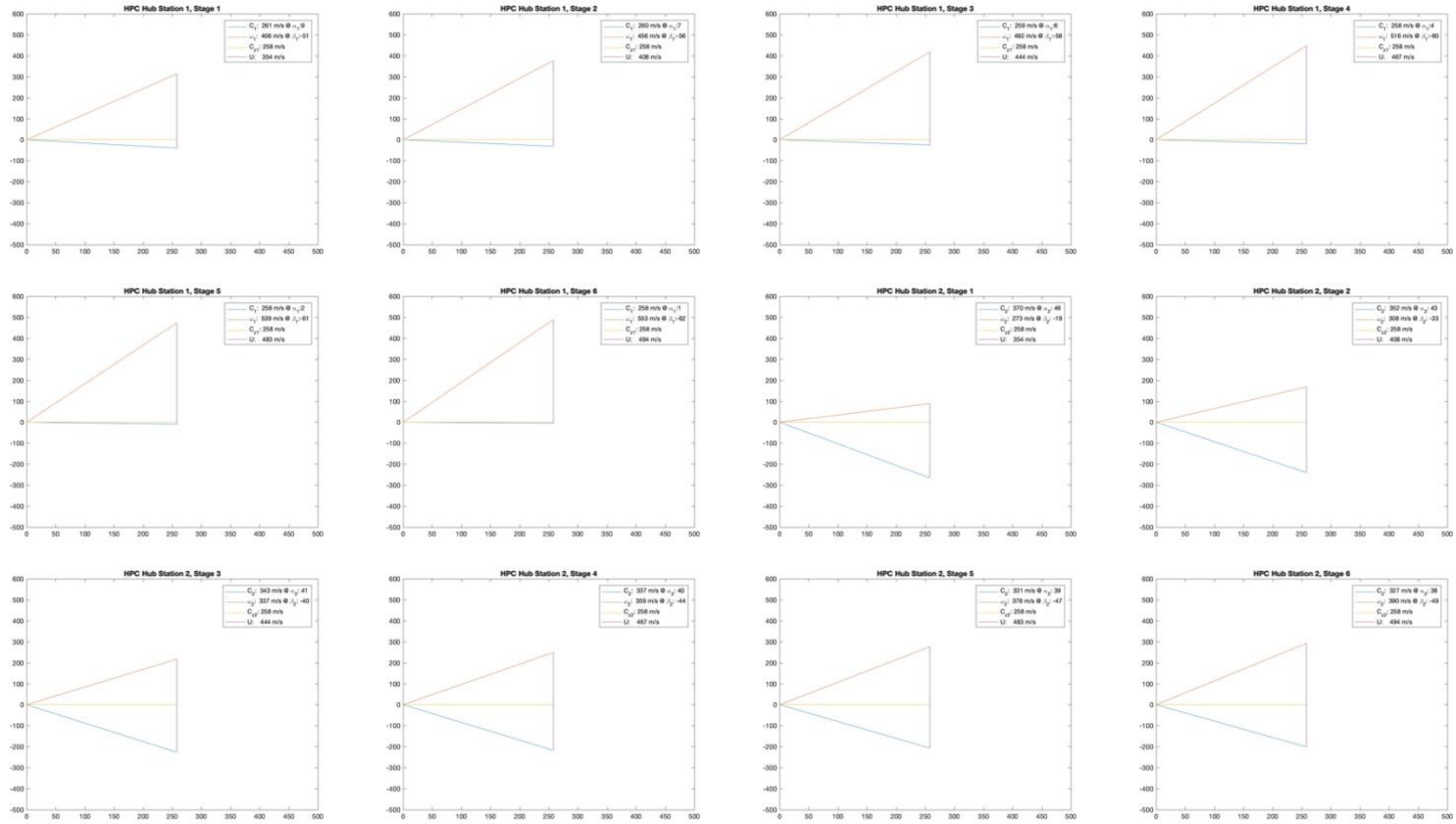


Figure 77. HPC Hub Velocity Triangles

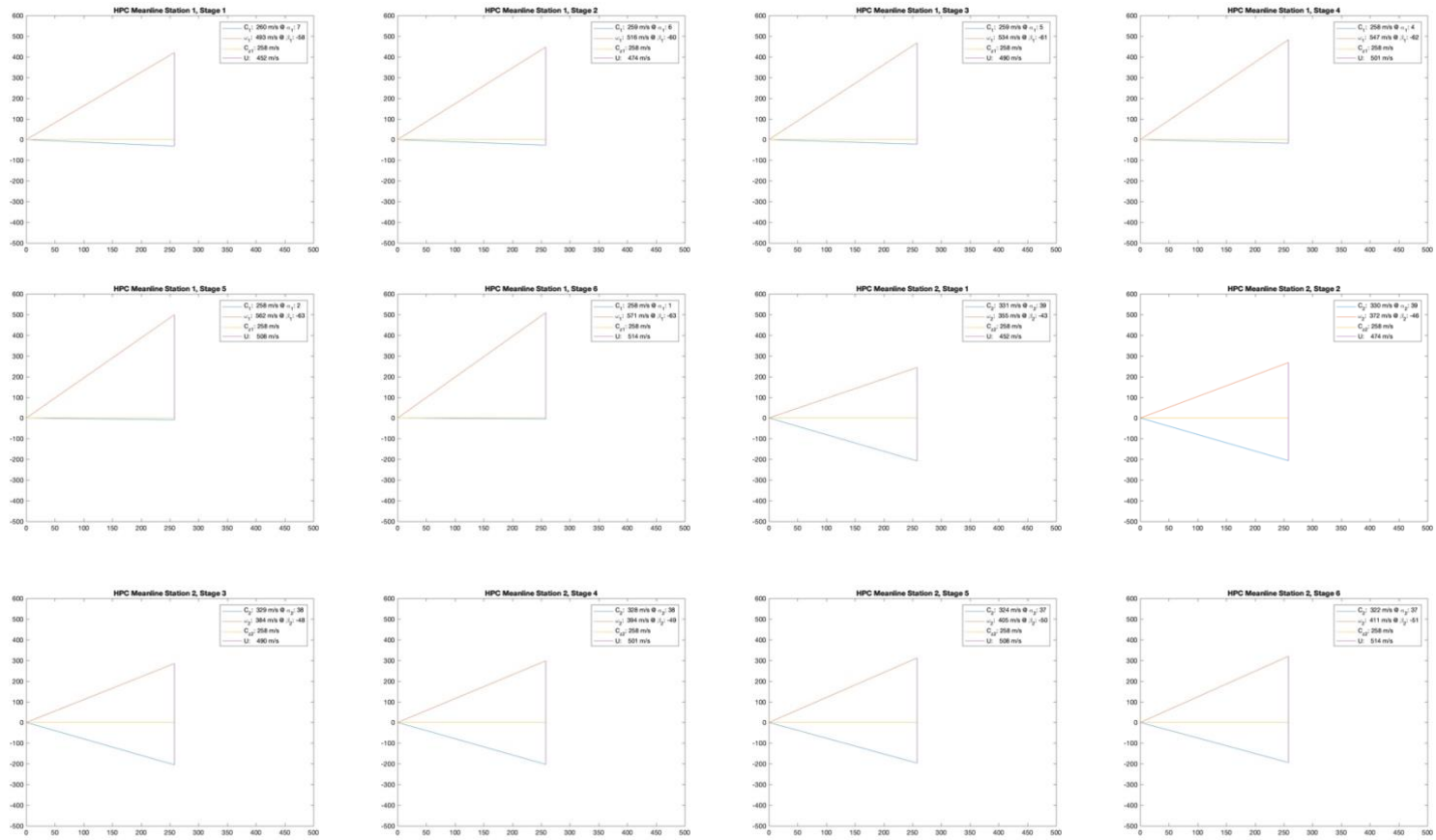


Figure 78. HPC Mean line Velocity Triangles

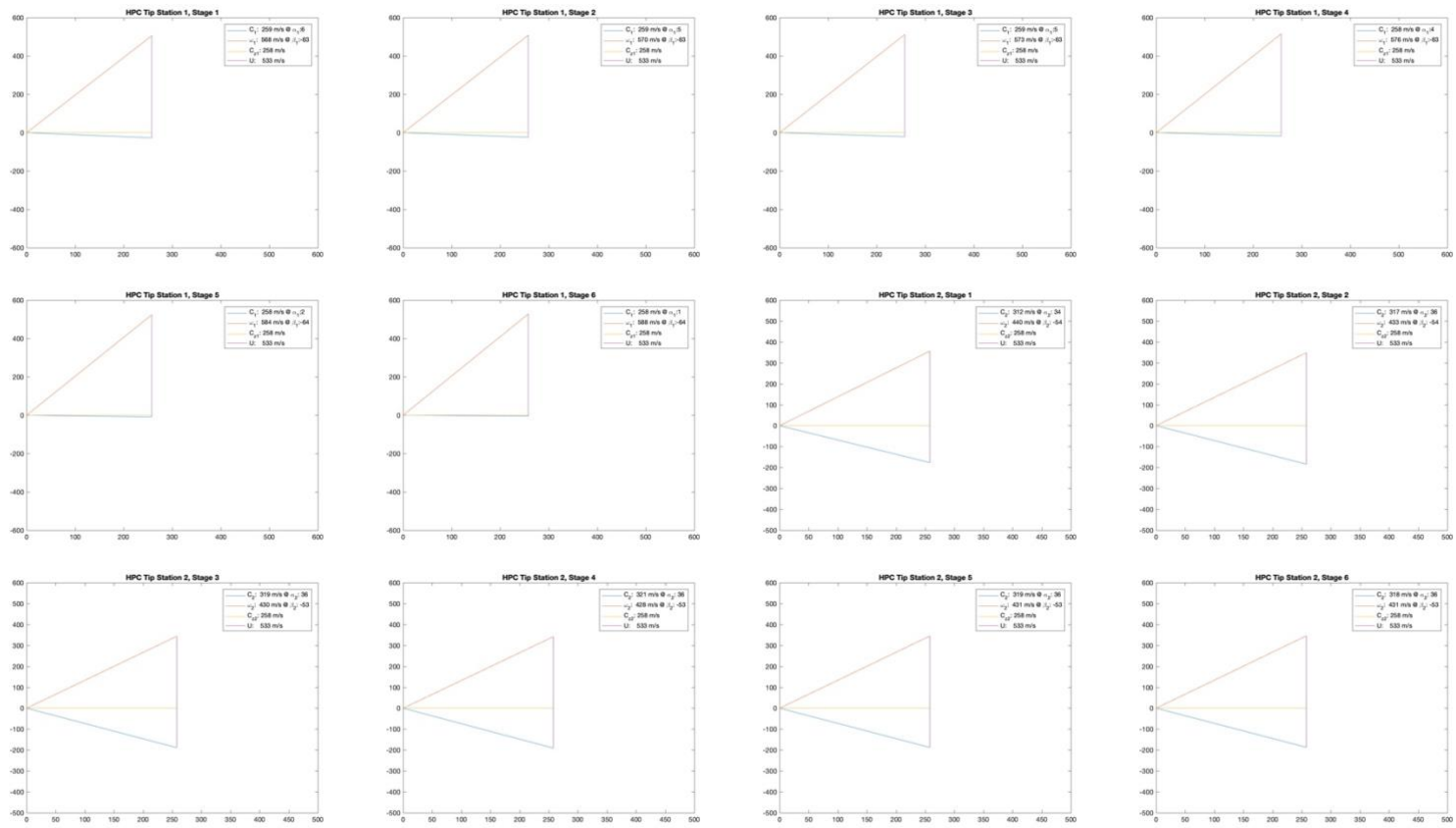


Figure 79. HPC Tip Velocity Triangles

Appendix G: HPT Velocity Triangles

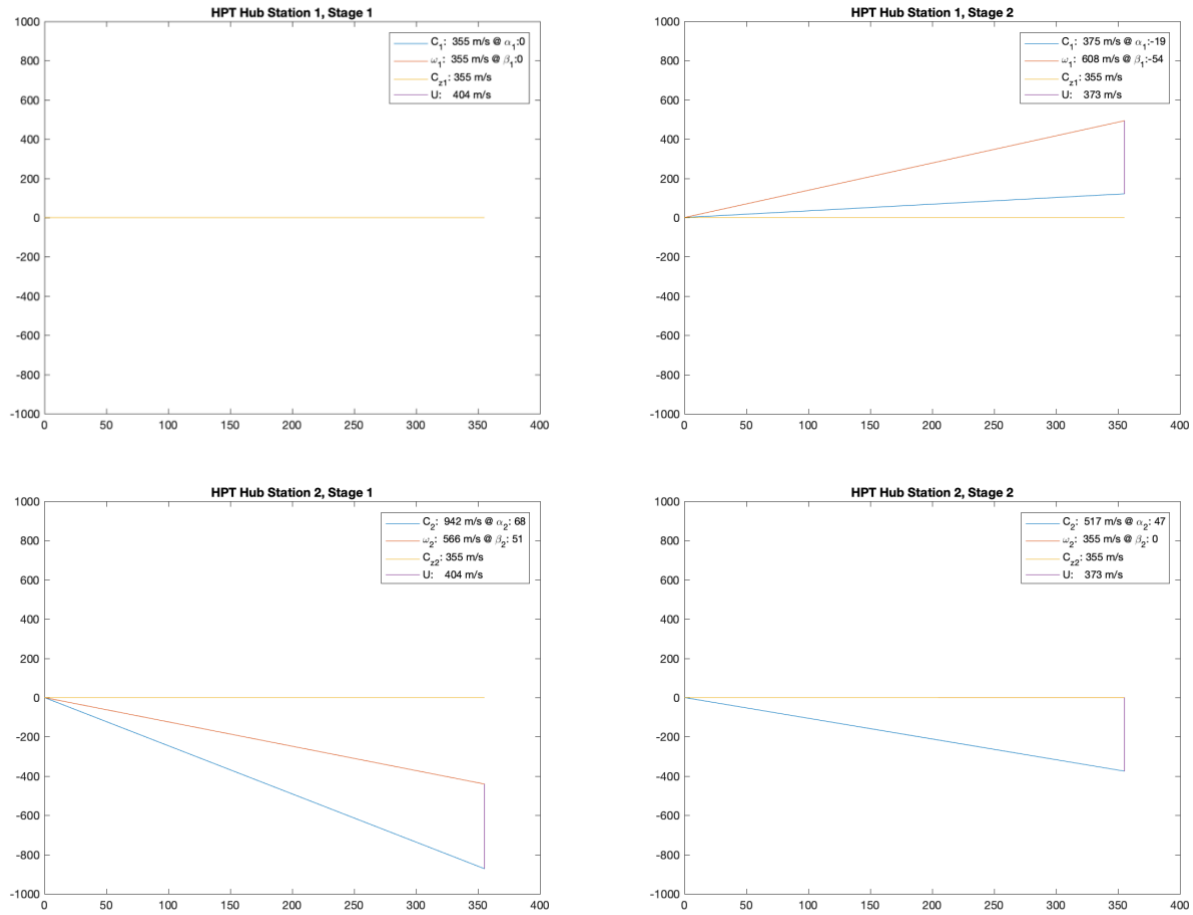


Figure 80. HPT Hub Velocity Triangles

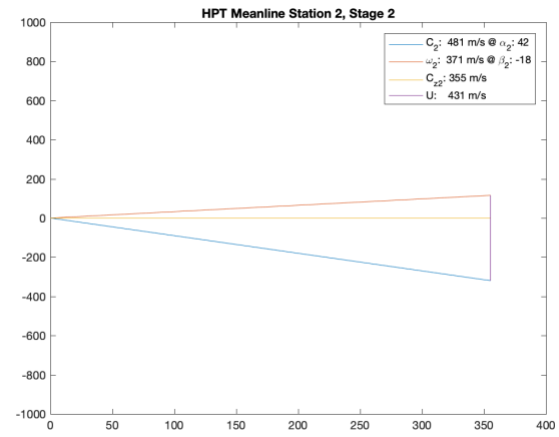
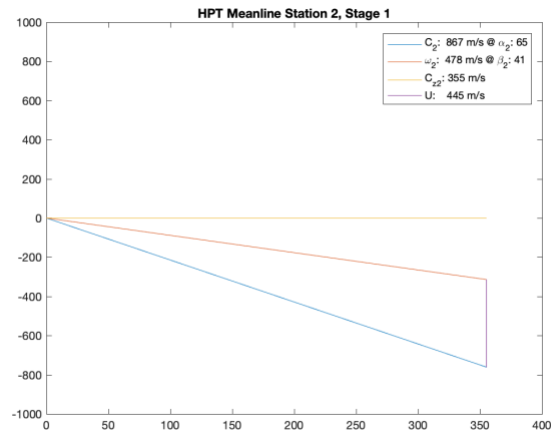
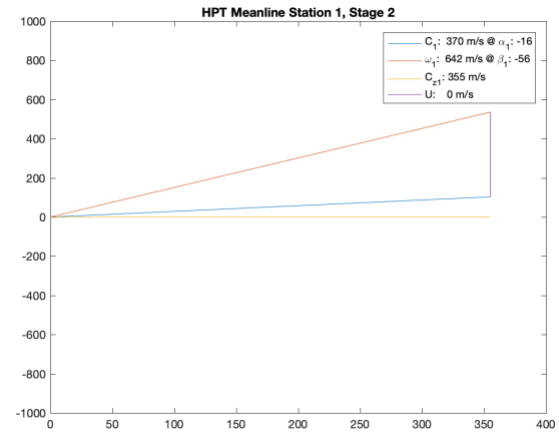
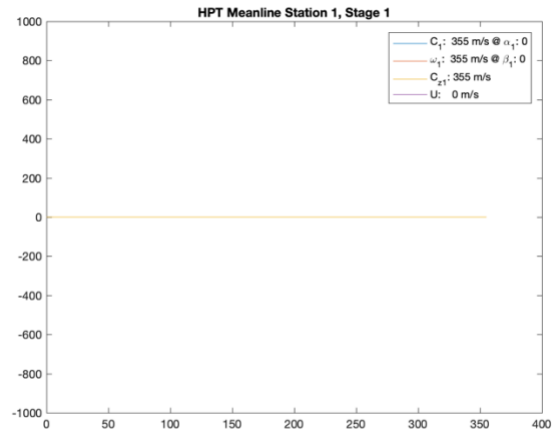


Figure 81. HPT Mean line Velocity Triangles

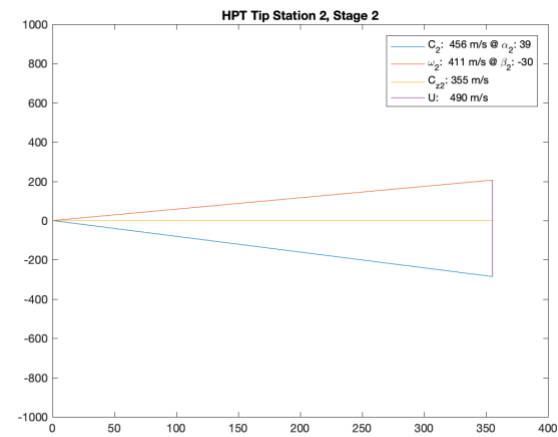
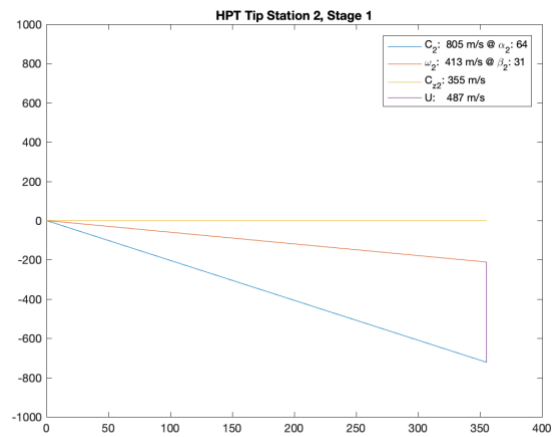
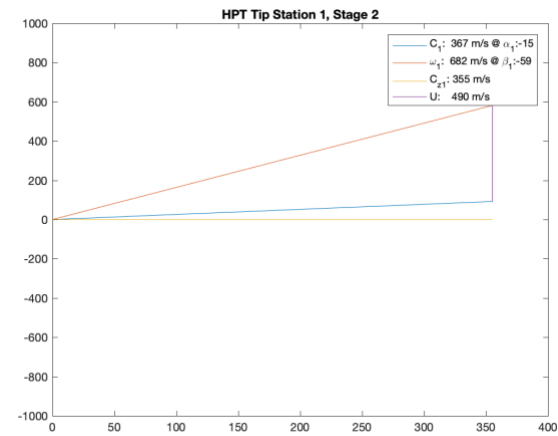
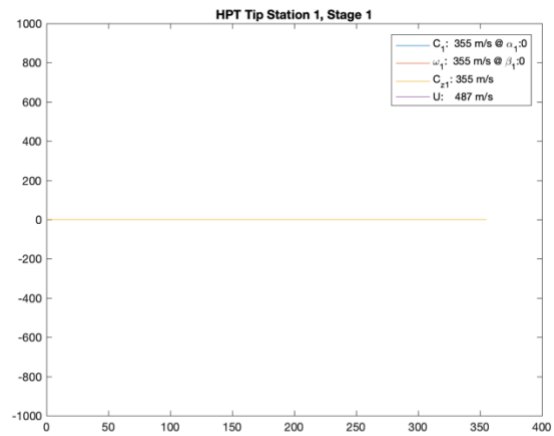


Figure 82. HPT Tip Velocity Triangles

Appendix H: LPT Velocity Triangles

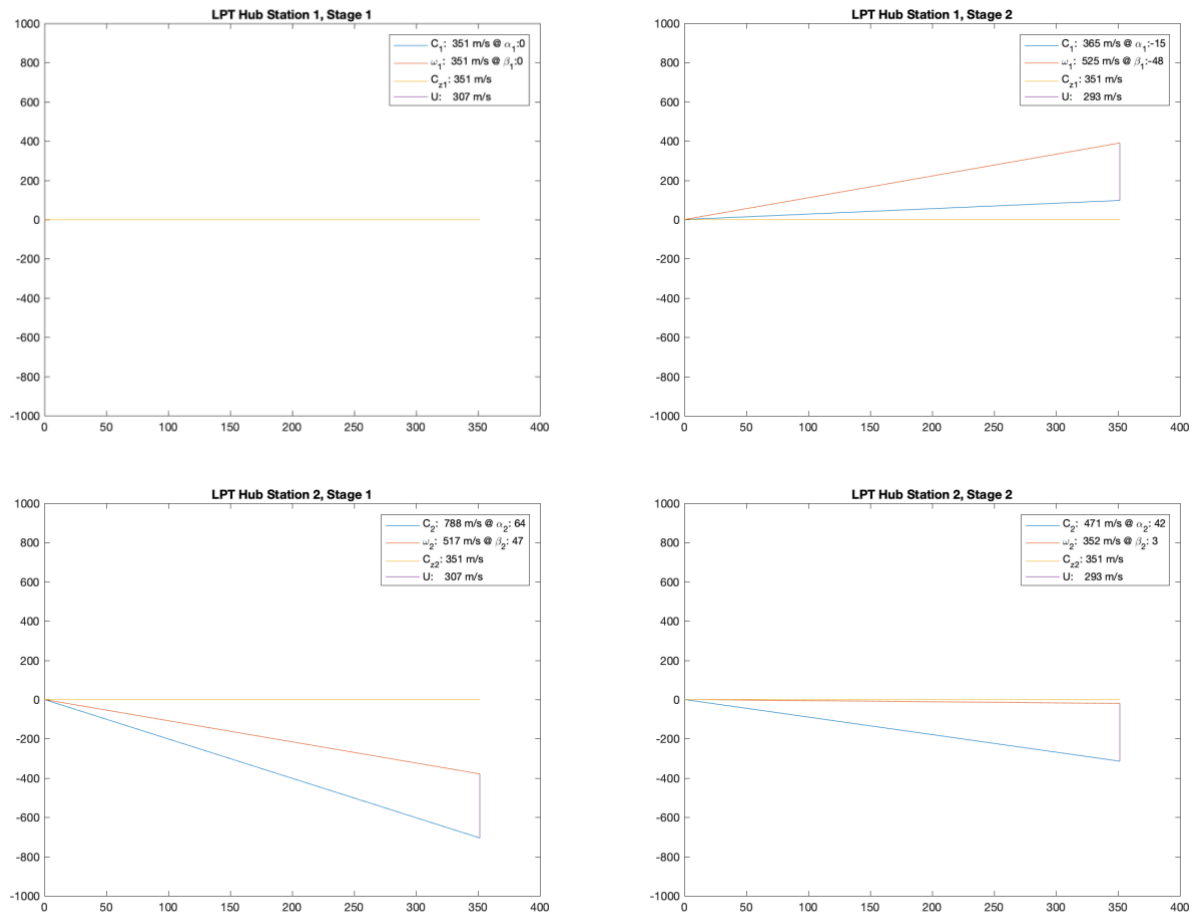


Figure 83. LPT Hub Velocity Triangles

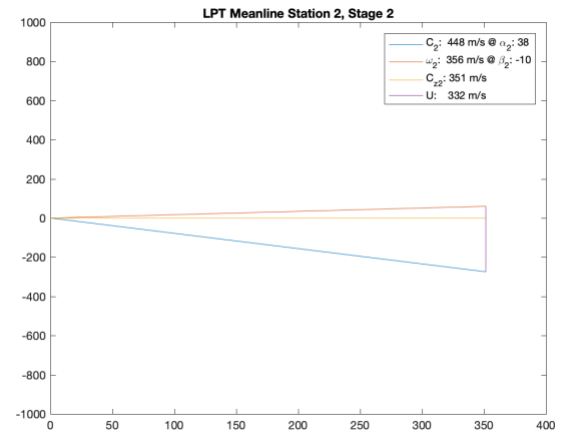
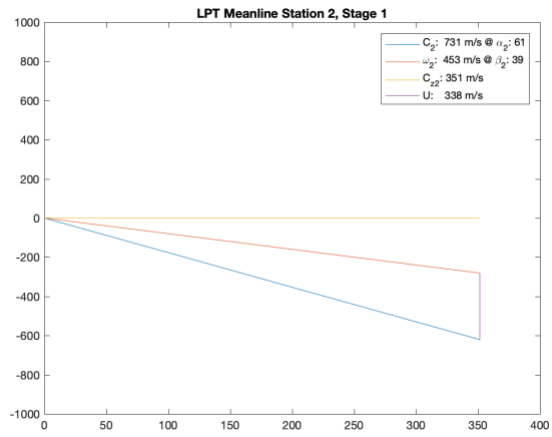
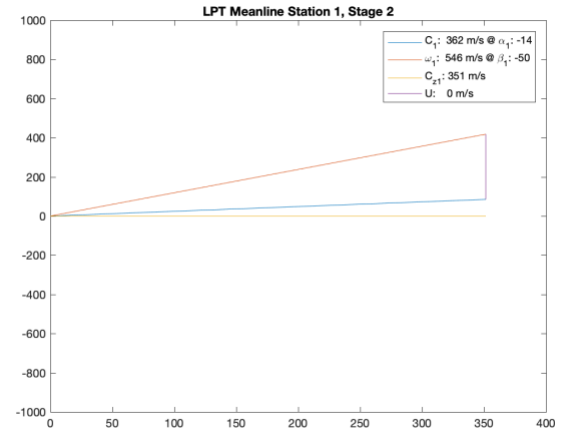
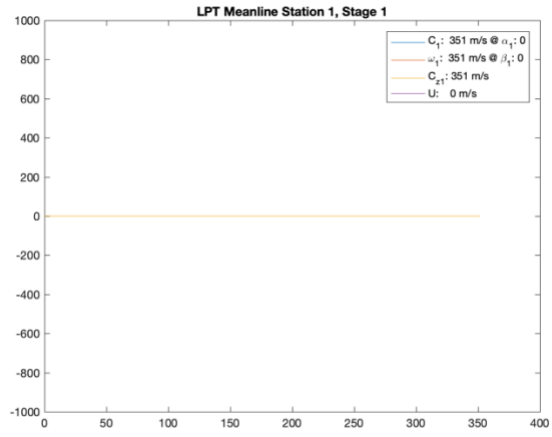


Figure 84. LPT Mean Line Velocity Triangles

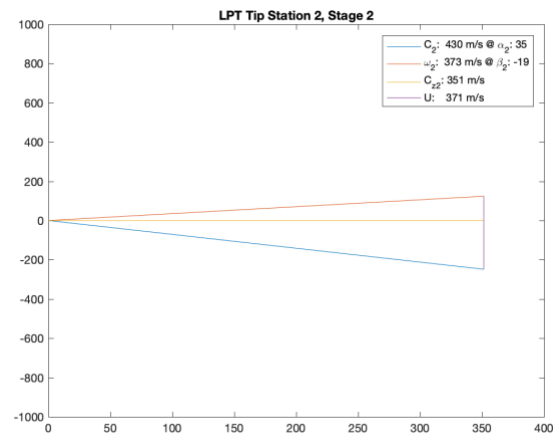
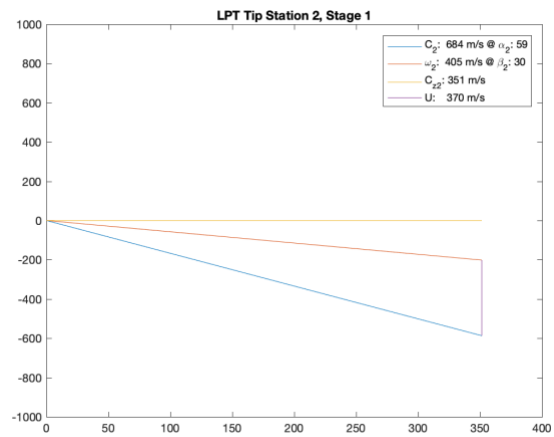
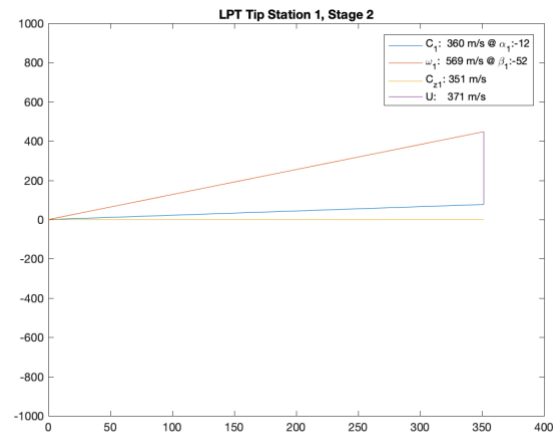
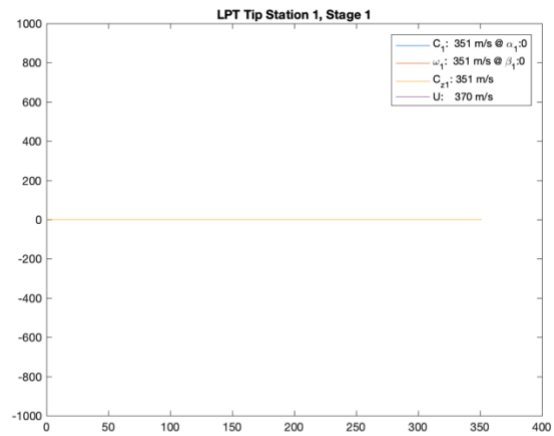


Figure 85. LPT Tip Velocity Triangles